

REPORT DOCUMENTATION PAGE

0523

Public reporting burden for this collection of information is estimated to average 1 hour per response, including the gathering and reviewing the data needed, and completing and reviewing the collection of information. Send comments collection of information, including suggestions for reducing this burden, to Washington Headquarters Service, Dept. Dev't Highway, Suite 1204, Arlington, VA 22202-4302, and to the Office of Management and Budget, Paperwork Redu...

1. AGENCY USE ONLY (Leave blank)		2. REPORT DATE February 1997	3. REPORT TYPE AND DATES COVERED Final Report Feb. 15, 1994-Feb. 14, 1997	
4. TITLE AND SUBTITLE TRANSPORT AND INTERFACIAL KINETICS IN MULTIPHASE COMBUSTION SYSTEMS			5. FUNDING NUMBERS PE - 61102F PR - 2308 SA - BS G - F49620-94-1-0143	
6. AUTHOR(S) Principal Investigator: Daniel E. Rosner				
7. PERFORMING ORGANIZATION NAME(S) AND ADDRESS(ES) Yale University High Temperature Chemical Reaction Engineering Laboratory Department of Chemical Engineering PO Box 208286 YS, New Haven, CT 06520-8286 USA			8. PERFORMING ORGANIZATION REPORT NUMBER	
9. SPONSORING/MONITORING AGENCY NAME(S) AND ADDRESS(ES) AFOSR/NA 110 Duncan Avenue, Suite B115 Bolling AFB DC 20332-0001			10. SPONSORING/MONITORING AGENCY REPORT NUMBER	
11. SUPPLEMENTARY NOTES				
12a. DISTRIBUTION/AVAILABILITY STATEMENT Approved for public release; distribution is unlimited			12b. DISTRIBUTION CODE	
13. ABSTRACT (Maximum 200 words) A 3-year program of research oriented toward the formation/transport of combustion-generated particles is summarized. Using thermophoretic sampling/TEM image analysis techniques, both inorganic (alumina) and carbonaceous soot aggregates have been shown to exhibit quantitatively similar morphologies. A thermophoresis-based method for measuring absolute local soot volume fractions, f_v , in flames has been successfully implemented (in both co-flow and counterflow laminar diffusion flames). Called <i>Thermocouple Particle Densitometry</i> (TPD), it exploits the laws governing thermocouple response to <i>thermophoretic soot deposition</i> , as first suggested by Eisner and Rosner in 1985. This method is independent of (often unknown) soot optical properties, unbiased with respect to soot morphology and size distribution, and yields spatially resolved f_v -values directly even at low soot concentrations (below 0.1 ppm). Accordingly, while neither "instantaneous" or "non-intrusive", it is especially applicable to spatially non-uniform and/or lightly sooting laminar steady flames. Ancillary studies of the transport properties of soot aggregates, and particle impaction on cylinders in high-speed crossflow are also described/documentated among the 30 cited references emerging from this program(Section 5). DTIC QUALITY INSPECTED 4				
14. SUBJECT TERMS Soot morphology, aggregated particles, particle mass transport, thermophoresis, sintering, Brownian diffusion, chemical vapor deposition, particle sampling, nano-particle formation/restructuring in flames, deposition rate theory			15. NUMBER OF PAGES 38	
			16. PRICE CODE	
17. SECURITY CLASSIFICATION OF REPORT Unclassified	18. SECURITY CLASSIFICATION OF THIS PAGE Unclassified	19. SECURITY CLASSIFICATION OF ABSTRACT Unclassified	20. LIMITATION OF ABSTRACT UL	

19971021 178

TRANSPORT AND INTERFACIAL KINETICS IN MULTIPHASE COMBUSTION SYSTEMS

Principal Investigator: Prof. Daniel E. Rosner

1. INTRODUCTION

The performance of aircraft gas turbine engines under sooting conditions and/or ramjets burning slurry fuels (leading to oxide aerosols and deposits), depends upon the formation and transport of small particles of complex morphology, often in non-isothermal combustion gas boundary layers (BLs). Aggregate formation / transport are also important in chemical reactors used to synthesize/process aerospace materials, including turbine blade coatings, optical waveguides, ceramic precursor powders,...). Accordingly, this 3 year research program was directed toward providing chemical propulsion system engineers with rational new predictive techniques to deal with particle formation-transport-deposition phenomena, accounting for significant non-spherical particle morphology effects. An interactive experimental/theoretical approach has been used to gain an understanding of performance-limiting mass/energy transfer-phenomena at or near interfaces. This included the development and exploitation of laboratory diffusion flame burners and new (thermophoresis-based) soot diagnostic/characterization techniques (Sections 2,5). Resulting experimental data, together with the predictions of asymptotic theories, were used to propose and verify *rational engineering correlations* for future design/optimization.

2. RESEARCH ACCOMPLISHMENTS

The most important results obtained under Grant AFOSR F49620-94-1-0143 during the period: **Feb. 15, 1994-Feb. 14, 1997** can be broadly divided into the subsections below. Since our techniques and results are so thoroughly documented in our archival publications (Section 5) and previous Annual Reports, this Final Report provides only a brief overview.

2.1. SEEDED LAMINAR COUNTERFLOW DIFFUSION FLAME EXPERIMENTS: FORMATION, COAGULATION, TRANSPORT AND STABILITY OF COMBUSTION-GENERATED PARTICLES

Particles produced during combustion processes frequently become aggregates of much smaller "primary" spherules, partially 'fused' due to high temperatures. Consequently, the resulting aggregates can differ in morphology and size according to the flame conditions under which they are generated and 'processed'. Since particle morphology and aggregate transport properties are interrelated (Tandon and Rosner, 1996), it is important to understand not only aggregate formation but also their *morphological evolution* in flames. We have carried out experimental investigations of the morphological evolution of flame-generated aggregates at low particle volume fractions ($O(10^{-1}$ ppm)) in a well-defined/characterized laminar non-premixed combustion environment. Al_2O_3 particles synthesized in a $Al(CH_3)_3$ (TMA)-seeded atmospheric pressure laminar counterflow diffusion flame fueled with $CH_4/O_2/N_2$ are used as the model material/combustion system (Xing, *et.al.*, 1996). Experiments include laser light scattering (LLS) and thermophoretic sampling/Transmission Electron Microscope (TEM) techniques (Koylu, *et.al.*, 1995). Aggregate morphology was characterized in terms of spherule ("grain") size, aggregate size, aggregate shape and fractal structure. Additionally, the effects of temperature and TMA concentration on particle sizes and morphology were also investigated systematically and interpreted based on parallel theoretical studies. LLS signals and typical TEM images clearly illustrated particle/aggregate size and morphology evolution as a result of two competing processes, with *coagulation* increasing aggregate sizes, and *sintering* reducing aggregate surface areas. Mean spherule diameters were found to be in the range of only 13 to 40 nm, increasing with increasing temperature and with TMA concentration. Mean aggregate sizes reached a maximum near a local temperature of only 1250 K and increased with TMA seed level. Perhaps most interesting, the final products were compact spherical particles resulting from complete 'collapse' of the aggregates, apparently as a result of surface diffusion rather than surface energy-driven "viscous flow". These results were shown to be compatible with the characteristic times governing each of the participating "unit" rate processes (Xing, *et.al.*, 1996). More comprehensive quantitative predictions are

underway for multi-phase laminar CDFs and will be part of our follow-on AFOSR research program. The experimental and theoretical methods developed and illustrated here will find applications in controlling the synthesis of valuable nano-powders, and facilitate rational extensions into the domain of *turbulent* non-premixed combustors generating desired or inadvertent ultrafine particles.

2.2 IMPLEMENTATION OF THERMOCOUPLE PARTICLE DENSITOMETRY (TPD)

Thermocouple Particle Densitometry (TPD) is a convenient, inexpensive and robust method for measuring absolute and local soot volume fractions, f_v , in flames first suggested by Eisner and Rosner in 1985. Based on the laws governing thermocouple response to *thermophoretic soot deposition*, this method has now been successfully implemented in both axisymmetric co-flowing laminar diffusion flames as well as CDFs (McEnally *et al.*, 1997). Since it yields spatially resolved f_v -values directly and can easily measure low soot concentrations, TPD is especially applicable to spatially non-uniform and/or lightly sooting flames. To further evaluate the method, TPD soot volume fractions (ppm) were recently measured in several laminar non-pre-mixed flames. In methane and ethylene counterflow flames the TPD results agreed to within experimental error with laser extinction measurements we performed in the same flames. In axisymmetric methane and ethylene co-flowing flames the shape of TPD f_v profiles also agreed well with published de-convoluted laser extinction measurements in similar flames. However, soot volume fractions inferred from mass deposition were systematically somewhat larger than laser *extinction* results in the lower portion of an ethylene co-flowing diffusion flame, and throughout a methane co-flowing flame, probably due to deposition of visible-light-transparent particles with masses of several thousand *amu*, known to be present in such flames. This implies that TPD could prove useful in future studies of the significance of these "invisible" soot precursors.

2.3 MORPHOLOGY OF FLAME-GENERATED 'SOOT' AGGREGATES

We have developed/tested/exploited practical image-analysis methods for inferring the fractal characteristics of thermophoretically sampled aggregates based on their projected (2-D) images (Koylu *et al.*, 1995).

Based on our investigation of over 3000 electron microscope images of soot aggregates from a variety of laminar and turbulent *hydrocarbon*-fueled flames we have found (Neimark *et al.* (1996)) that their scaling properties *cannot* be characterized solely using the now-familiar *mass fractal dimension*, D_f . Rather, the *asymmetric* properties of flame-generated soot evidently require the introduction of *longitudinal* ($[(1+H)/2] \cdot D_f$) and *transverse* ($[(1+H)/2H] \cdot D_f$) exponents, where $D_f=1.75$ and $H=0.91$. In this sense combustion-generated soot aggregates should apparently be regarded as *self-affine* rather than self-similar. Moreover, widely employed diffusion-limited cluster-cluster aggregation (DLCCA-) models, while undeniably providing a useful first approximation, are unable to accurately describe these aggregate populations not only with respect to $H \neq 1$ but also with respect to lacunarity (pre-exponential factor; see Koylu *et al.* (1995)). This statistically significant asymmetry may prove to be important for predicting essential *transport and radiative properties* of suspended aggregates.

2.4 THEORY OF TRANSPORT, RESTRUCTURING, AND RADIATIVE TRANSPORT PROPERTIES OF FLAME-GENERATED AGGREGATES

The ability to reliably predict transport properties and morphological stability of *aggregated* flame-generated *particles* (carbonaceous soot, Al_2O_3 , SiO_2 ,...) is important in chemical propulsion and refractory materials fabrication applications. We have developed efficient methods to anticipate coagulation, restructuring, and ultimate deposition rates of suspended populations of such particles in combustion systems, as well as laws needed to interpret laser-based soot diagnostics. In one asymptotic limit large 'fractal' aggregates are treated using a spatially variable, effective porosity pseudo-continuum model (see, *eg.*, Rosner and Tandon (1994) and Tandon and Rosner (1996)). Indeed, the competition between restructuring kinetics and coagulation kinetics determines the observed size of the apparent "primary" particles comprising soot particles (Xing and Rosner, 1996), as well as the "collapse" of surface area observed in some high temperature systems. These studies, together with our methods to predict interactions between aggregates and their surrounding *vapor* environment (interactions which can lead to

primary particle growth, or (for carbonaceous soot in the presence of oxidizing species burn-out) are now available to be incorporated into our laminar CDF structure modelling (Xing et.al.,1997). This work will also facilitate rational extensions into the uncharted domain of turbulent non-premixed combustors generating ultrafine particles, via extended flamelet models.

2.5 PARTICLE FORMATION AND TRANSPORT IN LAMINAR BOUNDARY LAYERS AND MIXING LAYERS

Because of the implications for depositing thin solid films (Rosner, Collins,1994) and soot layers we also investigated particle formation in laminar boundary layers and deposition near hot solid surfaces, leading to 'mixed' particle plus vapor deposition ("co-deposition", see Tandon and Rosner, 1996; Castillo and Rosner, 1996). These phenomena also occur when fuel-rich vapors 'impinge' on hot solid surfaces, as in gas turbine combustors. We have developed a promising rational approach to predict the self-consistent *deposit roughness* as well as deposition rate in such circumstances (Tandon and Rosner (1996).

2.6 PARTICLE IMPACTION ON CYLINDRICAL TARGETS; EROSION BEHAVIOR OF CERAMIC OR METAL TARGETS IN HIGH-SPEED ABRASIVE STREAMS

We have exploited our earlier correlations for *inertial impaction* using an *effective* Stokes number to calculate: a) particle deposition rates on cylindrical targets, including *rebound* behavior (Rosner and Tandon, 1995a) and b) the relation between the particle size distribution of *deposited* particles and the particle size distribution of the *mainstream* suspension (Rosner and Tandon, 1995b)

By capturing with simple formulae the essential features of available *erosion yield* experiments, we have developed an efficient method to predict local and total surface *erosion rates* for metal or ceramic targets of simple geometry exposed to a 'polydispersed' population of abrasive particles suspended in a high-speed mainstream (Rosner *et.al.* (1995), Kho *et.al.* (1995), Khalil and Rosner(1996)). Our earliest methods/results (*loc. cit.*) were deliberately limited to small relative changes in body shape to allow for arbitrary Stokes numbers. We then relaxed this assumption for the limiting (worst-) case of rectilinear erodent particle trajectories. The interface was assumed to recede normal to itself at the rate determined by the local particle impaction frequency, angle-of-incidence and velocity (Rosner and Khalil (1996)). The normalized "body" radius $R(\theta, \tau)$ at polar angle θ , and dimensionless exposure time τ was found to satisfy an interesting first-order nonlinear PDE. Illustrative results were obtained comparing the erosion rate behavior of initially circular targets of a *ceramic* and a *metal* by numerically solving this PDE using the "method of lines". Calculated interface positions revealed "nose blunting" for the erosion of *ceramic* targets in a uniform erodent-carrying stream. In contrast, "nose-sharpening" occurred for *metal* targets, with the development of an ogive-shaped feature facing upstream. Our methods can be used to calculate/correlate the erosion behavior of targets of other important aerodynamic *shapes*, including spheres, cones,..... These methods/results will allow aerospace design engineers to anticipate erosion behavior in a variety of particle-laden flow environments, and provide guidance on tolerable particle loadings, required maintenance frequencies, and materials selection.

3. ADMINISTRATIVE INFORMATION: PERSONNEL, PRESENTATIONS, APPLICATIONS, TECHNOLOGY TRANSFER

The following sections summarize some pertinent facets of the abovementioned Yale HTCRC Lab/AFOSR three year research program of management interest:

3.1 Research Personnel

Our present results (Sections 2 and 5) are due to the contributions of the individuals listed in Table 3.1-1, which also indicates the role of each researcher. It will be noted that, in addition to the results themselves, this program has simultaneously contributed to the research training of my PhD students J. Collins, P. Tandon, and Y. Xing, who are now be in an excellent position to make future contributions to technologies oriented toward air-breathing chemical propulsion, and/or high-tech aerospace materials processing.

Table 3.1-1 Summary of *Research Participants*^a on AFOSR Grant: F49620-94-1-0143:

**TRANSPORT PHENOMENA AND INTERFACIAL KINETICS
IN MULTIPHASE COMBUSTION SYSTEMS**

Name	Status ^a	Principal Research Activity ^b
Castillo, J.L.	Res. Vis.	x-port props. of aggregates
Collins, J.	PDRA	chemical vapor deposition
Farias, T.	Res. Vis.	radiative props. of aggregated soot
Garcia-Ybarra, P.	Res. Vis.	x-port props. of aggregates
Khalil, Y.F.	Res. Assoc.	erosion of ceramics
Kho, T.	GRA(MS)	CV-Deposit density correlation
Konstandopoulos, A.G.	Res. Vis.	deposition rate theory
Koylu, U.O.	PDRA	thermophoretic sampling/image analysis
McEnally, C.	PDRA	thermophoresis-based soot diagnostics
Neimark, A. V.	Vis. Fac.	fractal morphology of aggregates
Rosner, D.E.	PI	program direction-dep. theory/exp
Tandon, P.	GRA,PDRA	x-port props. of aggregates
Xing, Y.	GRA	particle prod/char. in CDFs
Vaidya, D.	PDRA	simultaneous coag. + restructuring

^a PDRA=Post-doctoral Research Asst
PI = Principal Investigator

GRA= Graduate Research Assistant (PhD unless designated MS)
^b See Section 5for specific references cited in text (Section 2)

3.2 Cooperation with US Industry

While the research summarized here was supported by AFOSR under Grant AFOSR 94-1-0143, the Yale HTCRC Laboratory has also been the beneficiary of continuing smaller grants from U.S. industrial corporations, including groups within ALCOA, GE, DuPont, Union Carbide (now Advanced Ceramics Corp.) and Shell, as well as the feedback and occasional advice of principal scientists/engineers from each of these corporations and Combustion Engineering-ABB and Textron. We appreciate this level of collaboration, and expect that it will accelerate inevitable applications of our results in areas relevant to their technological objectives (see, also, Section 3.4, below).

Periodically our results are picked up and used by aerospace industrial contractors. As mentioned below and included in my September 1996 report as a formal "Technology Transition", a variant of our recent method to correlate/predict the density of vapor deposited graphite, BN,...(Kho,*et.al.*,1995, Section 5.1) is being used by Advanced Ceramics Corp. (M. B. Dowell, *et.al.*) to guide the selection of production conditions in their CVD reactors. Another such transition based on the PhD research of J. Collins, 1995 is also taking shape and will be reported in due course.

3.3 External Presentations, Research Training

Apart from the *ca.* 24 publications itemized in Section 5.1, and the 5 submitted papers now in print (Section 5.2) verbal accounts of our research on soot diagnostic techniques, soot morphology and transport, particle and vapor deposition dynamics, and erosion were presented on some 32 occasions over this reporting period, including invited presentations at the US Corporations: DuPont, ALCOA, and PPG, and at each of the annual AIChE, AAAR and MRS meetings. As noted below, the present 3 year AFOSR program has also led to some 120 citations under the PI's name: Rosner, D.E. in *Science Citation Index*.

This research program also involved completion of the PhD dissertation research of Joshua Collins and Pushkar Tandon, and will be the basis of the PhD dissertation of Yangchuan Xing, expected to defend his work in September of this year.

3.4 Applications of Yale-HTCRE Lab Research Results, Including Technology Transfer

It has been gratifying to see direct applications of some of this generic AFOSR-supported particle and vapor mass transfer research in more applications-oriented investigations reported in recent years. Indeed, *the writer would appreciate it if further examples known to the reader can be brought to his attention.* As a result of the present 3 year AFOSR program, over one hundred citations under the PI's name: Rosner, D.E. have appeared in *Science Citation Index*.

We communicated a Sept. 1996 *Technology Transition* which was a variant of our recent method to correlate/predict the density of vapor deposited graphite, BN,...(Kho,*et.al.*,1995). This correlation is being used by Advanced Ceramics Corp. (M. B. Dowell, *et.al.*) to guide their selection of CVD reactor operating conditions. It should also be applicable in the field of diamond film deposition.

While the work described in McEnally *et.al.*, 1997, has the potential of leading to a thermocouple-based instrument/software package for determining local soot volume fractions and temperatures in laminar flames (based on the laws of soot particle thermophoresis, completely independent of particle optical properties, and applicable to very low soot volume fractions), we have no immediate plans to pursue the patent/licencing implications. Our most recent demonstration that thermophoretic theory combined with TEM-grid information can provide local soot volume fractions as well as all required morphological information (Koylu *et. al.*, 1997; Section 5.2), is expected to have a significant influence on soot research worldwide, especially since the optical properties of "young" soot are poorly known.

Of course, in combustion fundamentals research, many groups (*eg.*, Dobbins *et.al.* (Brown U.), Faeth *et.al.* (U. Mich.), Katz *et al.* (J. Hopkins U.)) are now utilizing "thermophoretic sampling" techniques to exploit the size- and morphology-insensitive capture efficiency characteristics proven in our AFOSR research (Sections 2.1, 2.3). Our earlier thermophoretic studies (*eg.*, Gomez and Rosner, 1993) have also led to an appreciation of the associated systematic corrections needed in particle velocimetry, as well as the important role that particle stagnation plane location plays in powder synthesis flames.

Our AFOSR-supported research on *soot deposition rates* from flowing laminar or turbulent combustion gases is now also the basis of a collaborative AGARD-NATO supported program with IST-Lisbon (Profs. M. G. Carvalho, T. Farias), and was applied earlier by Aerojet Corp. to develop (NASA support) a model for application to rocket chambers and nozzles. Extensions to jet engine nozzles have been made by M.T. Nys at Pratt & Whitney Engine Business in W. Palm Beach FL. Applications of our AFOSR and DOE-supported research (on the correlation of inertial impaction by cylinders in crossflow) recently made by the National Engineering Laboratory (NEL) of Glasgow and somewhat similar to those reported earlier by the Combustion R&D groups at MIT, Sandia-Livermore CRF and Penn State U, are now being taken up by VTT-Energy/Aerosol Technology Group, in Finland.

For calculating suspended particle concentrations along trajectories outside of aircraft (involved in atmospheric sampling), or inside of CVD reactors, A. S. Geller and D. J. Rader of Sandia-Albuquerque have adopted a method developed in our earlier AFOSR work (Fernandez de la Mora, 1981), and recently applied in our own studies of particle motion in laminar boundary layers with streamwise curvature (Konstandopoulos and Rosner, 1995). Some of this work may also be useful in future sampling studies of condensation nuclei emerging from stratospheric aircraft.

Earlier work at MIT, PSI and Sandia CRF had incorporated our rational correlation of *inertial particle impaction* (*e.g.* a cylinder in cross-flow) in terms of our *effective Stokes number* (see, *eg.* Rosner and Tandon, 1995a,b). Now our correlations of deposition by simultaneous thermophoresis and inertia are being used in the interpretation of heat exchanger fouling data in Grenoble, France.

In the area of multicomponent *vapor* deposition in combustion systems our discussion in the 26th *Comb. Symposium* of the paper of Steinberg and Schofield (Re: alkali salt deposition experiments) cites our earlier relevant work and may lead to future extensions. Another of our discussions in the 26th *Comb. Symposium* pertains to the potentially important role of temperature "jump" phenomena (see, *eg.*, Rosner and Papadopoulos, 1996) in the CARS temperature experiments of Bertagnolli and Lucht on the growth of diamond films using combustion techniques.

Fruitful *opportunities* for the further application of our recent research on the morphology/transport properties of combustion-generated particles and "non-Brownian" convective mass transfer for particles and vapors now exist in many of the programs currently supported by the US Air Force, as well as civilian sector R&D. This includes mass transfer and fouling aspects of fuel-coolant breakdown upstream of high pressure aircraft gas turbine combustors.

4. CONCLUSIONS

The ability to reliably predict the transport properties and stability of *aggregated* flame-generated particles (carbonaceous soot, B₂O₃, Al₂O₃,...)† is important for many technologies relevant to the U.S.A.F., especially jet engine and ramjet combustor design. Indeed, realistic soot morphology is not yet even a part of chemically complex sooting *laminar* flame models, and the computational methods used to include coagulation dynamics (*eg.*, "moment" or "sectional" finite-difference) methods) do not lend themselves to this next step. Also, some properties needed to correctly interpret the results of recently introduced laser diagnostics applied in research on soot formation/suppression (*eg.*, laser-induced incandescence (LII)) are not yet available. In this AFOSR program (94-1-0143) considerable experimental and theoretical progress along these lines has been made (Section 2) and reported (Section 5). These experimental techniques, together with closely coupled theoretical calculations of particle birth/dynamics in counterflow diffusion flames and mixing/boundary layers, are leading to a valuable understanding of combustion-generated ultra-fine particles, including their evolution/deposition dynamics in turbulent high pressure systems.

†Finely divided boron- and aluminum-based fuel additives for performance enhancement lead to non-carbonaceous "soots" in many air-breathing and rocket combustor situations. Moreover, trace inorganics in petroleum-based fuels, or in the air breathed for combustion likewise lead to submicron inorganic aerosols affecting system performance, including jet-engine contrail formation in the stratosphere. In this AFOSR program we have shown that soot aggregates from a wide variety of organic and inorganic combustion systems exhibit interesting and mechanistically significant morphological similarities (Rosner, 1996, Koylu *et al.*, 1995, Xing *et al.*, 1996)

5. REFERENCES

5.1 PUBLICATIONS WHICH APPEARED* BASED ON GRANT AFOSR 94-1-0143

- Castillo, J.L. and Rosner, D.E., "Role of High Activation Energy Homogeneous Chemical Reactions in Affecting CVD Rates and Deposit Quality for Heated Surfaces", *Chemical Engineering Sci.* 51 (24) 5325-5340 (1996)
- Collins, J., **Effects of Homogeneous Reaction on the Chemical Vapor Deposition of Titanium Dioxide**, PhD Dissertation, Yale University-Graduate School, Dept. Chemical Engineering, 1994
- Farias, T.L., Koylu, U.O., and Carvalho, M.G., "Effects of Polydispersity of Aggregates and Primary Particles on Radiative Properties of Simulated Soot", *J. Quant. Spectros. Radiat. Transfer* 55 (3) 357-371 (1996)
- Gokoglu, S.A., Stewart, G.D., Collins, J., and Rosner, D.E., "Numerical Analysis of an Impinging Jet Reactor for the CVD and Gas Phase Nucleation of Titania", *Mat. Res. Sympos. Proc. Vol. 335*, 171-176 (1994)
- Khalil, Y. F. and Rosner, D.E., "Erosion Rate Prediction and Correlation Technique for Ceramic Surfaces Exposed to High-Speed Flows of Abrasive Suspensions", *WEAR* 201, 64-79 (1996)¶

¶Reproduced (with Form 298) in Section 6; all other archival papers have been included in our previous Annual Reports on this Grant.

- Kho, T., Collins, J. and Rosner, D. E., "Development, Preliminary Testing, and Future Applications of a Rational Correlation for the Grain Densities of Vapor-Deposited Materials" *J. Materials Sci.*, **30** 3440-3448 (1995)
- Konstandopoulos, A.G. and Rosner, D.E., "Inertial Effects on Thermophoretic Transport of Small Particles to Walls With Streamwise Curvature---I. Theory, *Int. J. Heat Mass Transfer* (Pergamon) **38** (12) 2305-2315 (1995)
- Konstandopoulos, A.G. and Rosner, D.E., "Inertial Effects on Thermophoretic Transport of Small Particles to Walls With Streamwise Curvature---II. Experiment, *Int. J. Heat Mass Transfer* (Pergamon) **38** (12) 2317-2327 (1995)
- Koylu, U.O. and Faeth, G.M., "Spectral Extinction Coefficients of Soot Aggregates From Turbulent Diffusion Flames", *J. Heat Transfer* (ASME) **118** (5) 415-421 (1996)
- Koylu, U.O., Xing, Y., and Rosner, D.E., "Fractal Morphology Analysis of Combustion-Generated Aggregates Using Angular Light Scattering and Electron Microscope Images", *Langmuir* (Amer. Chem. Soc.) **11** (12) 4848-4854 (1995)
- Koylu, U. O., "Quantitative Analysis of *In-situ* Optical Diagnostics for Inferring Particle/Aggregate Parameters in Flames: Implications for Soot Surface Growth and Total Emissivity", *Comb & Flame* **109**, 488-500 (1996)
- Mackowski, D.W., Tassopoulos, M. and Rosner, D.E., "Effect of Radiative Heat Transfer on the Coagulation Dynamics of Combustion-Generated Particles", *Aerosol Sci. Technol.*(AAAR) **20** (1) 83-99, (1994)
- Neimark, A.V., Koylu, U. O., and Rosner, D.E., "Extended Characterization of Combustion-Generated Aggregates: Self-Affinity and Lacunarities", *J. Colloid Int. Sci.*, **180**, 590-597(1996)¶
- Rosner, D.E. and Tandon, P., "Prediction and Correlation of 'Accessible' Area of Large Multi-particle Aggregates", *AIChE J.* **40** (7), 1167-1182 (1994)
- Rosner, D.E., Tandon, P. and Konstandopoulos, A.G., "Rational Prediction of Inertially Induced Particle Deposition Rates for a Cylindrical Target in Dust-Laden Streams", *Proc. 1st Int. Particle Technology Forum*, AIChE, Vol. II, 374-381 (1994).
- Rosner, D. E., Tandon, P., and Labowsky, M.J., "Rapid Estimation of Cylinder Erosion Rates in Abrasive Dust-Laden Streams: Effects of Erosion Rate Law and Dust Polydispersity on Predicted Local and Total Target Wear", *AIChE J.*, **41**(5) 1081-1098 (1995)
- Rosner, D.E., Khalil, Y.F. and Tandon, P., "Prediction/Correlation of Erosion Rates and Shape Evolution for Ceramic Surfaces Exposed to Flows of Abrasive Suspensions", *Proc. Fifth World Congress of Chemical Engineering*, AIChE, San Diego, CA, July 14-18, 1996 Paper #112e, Vol. IV, 1013-1018 (1996)
- Rosner, D.E. and Tandon, P., "Rational Prediction of Inertially Induced Particle *Deposition* Rates for a Cylindrical Target in a Dust-Laden Stream" *Chem Eng. Sci.* **50** (21) 3409-3431(1995a)
- Rosner, D. E., Tandon, A.G., and Konstandopoulos, A.G., "Local Size Distributions of Particles Deposited by Inertial Impaction on a Cylindrical Target in Dust-Laden Streams", *J. Aerosol Sci.*,(Pergamon) **26** (8) 1257-1279 (1995b)
- Rosner, D.E. and Papadopoulos, D., "Jump, Slip and Creep Boundary Conditions at Nonequilibrium Gas/Solid Interfaces", *Ind Eng Chem-Res* (ACS) **35**(9) 3210-3222 (1996) ¶
- Tandon, P., and Rosner, D. E., "Translational Brownian Diffusion Coefficient of Large (Multi-Particle) Suspended Aggregates", *Ind Eng Chem-Res* (ACS) **34** 3265-3277(1995)
- Tandon, P., and Rosner, D. E., "Co-deposition on Hot CVD Surfaces: Particle Dynamics and Deposit Roughness Interactions", *AIChE J.* **42** (6) 1673-1684 (1996)
- Tandon P., **Transport Theory for Particles Generated in Combustion Environments**, PhD Dissertation, Yale University-Graduate School, Dept. Chemical Engineering, May 1995
- Xing, Y., Köylü Ü. Ö., Tandon P. and Rosner D. E., "Measuring and Modeling the Synthesis and Morphological Evolution of Particles in Counterflow Diffusion Flames", *Proc. Fifth World Congress of Chemical Engineering*, AIChE, San Diego, CA, July 14-18, 1996 Paper #88d, Vol. V, pp 43-48.

Xing, Y., and Rosner, D.E., "Surface Melting of Particles: Predicting Spherule Size in Vapor-Phase Nanometer Particle Formation", Paper#V5.36, MRS Fall 1996 Meeting, Dec. 4, 1996, Boston MA

Xing, Y., Köylü Ü. Ö., and Rosner D. E., "Synthesis and Restructuring of Inorganic Nano-particles in Counterflow Diffusion Flames", *Comb & Flame* 107 85-102(1996)

5.2 PAPERS SUBMITTED BASED ON GRANT AFOSR 94-1-0143

Koylu, U.O., McEnally, C.S., Rosner, D.E and Pfefferle, L.D., "Simultaneous Measurements of Soot Volume Fraction and Particle Size/Microstructure in Flames Using a Thermophoretic Sampling Technique", *Comb & Flame* 110 494-507(1997)

McEnally, C.S., Koylu, U.O., Pfefferle, L.D. and Rosner, D.E., "Soot Volume Fraction and Temperature Measurements in Laminar Non-Premixed Flames Using Thermocouples", *Comb & Flame* 109 701-720(1997)

Rosner, D.E., "Combustion Synthesis and Materials Processing", *Chemical Engineering Education* (ASEE), Fall 1997 Graduate Issue (ca. November 1997)

Tandon, P., and Rosner, D.E., "Monte-Carlo Simulation of Simultaneous Fractal Particle Aggregation and Restructuring", *J Colloid Interface Sci.* (in press, 1997)

Xing, Y., Rosner, D.E., Koylu, U.O. and Tandon, P., "Morphological Evolution of Oxide Nano-particles in Laminar Counterflow Diffusion Flames---Measurements and Modelling", *AIChE J.* (Special Issue on Ceramics Processing)(in press, Fall 1997); *AIChE '97 Mtg.*, Invited Lecture (Nov. 1997)

LIST OF ABBREVIATIONS

ALS	Angular Light Scattering	BL	Boundary layer
CDF	Counterflow diffusion flame	TEM	Transmission Electron Microscopy
CVD	Chemical vapor deposition	CRF	Combustion Research Facility
CSL	Chemical sublayer	CFD	Computational Fluid Dynamics
D_f	Fractal dimension	GRA	Graduate research Asst.
G/S	Gas/solid interface	IJHMT	<i>Int. J. Heat/Mass Xfer</i>
LDV	Laser Doppler Velocimetry	LII	Laser-induced incandescence
LLS	Laser light scattering	LTCE	local thermochemequilibrium
PBE	Population Balance Eq.	<i>pdf</i>	Probability density function
PI	Principal Investigator	PSD	Particle size distribution
MRS	Materials Research Society	TMA	Trimethyl aluminum
VS	Visiting Scholar	TPD	Thermocouple Particle Densitometry

6. APPENDICES (Complete Papers Published During Period: 2/15/94 -2/14/97 on GRANT AFOSR 94-1-0143; including Form 298 for each)

PIADC INFO (cf. Sections 5.1, 6) to follow:

PIADC INFO (cf. Sections 5.1, 6):

Name of Journal: *Comb & Flame*

Title of Article: "Synthesis and Restructuring of Inorganic Nano-particles in Counterflow Diffusion Flames"

Authors: Xing, Y., Koçylu, U. O., and Rosner, D.E.

Publisher: Combustion Inst. (Pittsburgh PA)

Volume: **107** Pages: 85-102 Month Published: Year: (1996)

Name of Journal: *Ind. Engrg. Chem- Research*

Title of Article: "Jump, Slip and Creep Boundary Conditions at Non-equilibrium Gas/ Solid Interfaces"

Authors: Rosner, D.E. and Papadopoulos, D.

Publisher: Amer. Chem Soc.

Volume: **35** Pages: 3210-3222 Month Published: September Year: (1996)

Name of Journal: *WEAR*

Title of Article: "Erosion Rate Prediction and Correlation Technique for Ceramic Surfaces Exposed to High-Speed Flows of Abrasive Suspensions"

Authors: Khalil, Y.F. and Rosner, D.E.

Publisher: Elsevier

Volume: **201** Pages: 64-79 Month Published: Year: (1996)

REPORT DOCUMENTATION PAGE

Form Approved
OMB No. 0704-0188

Public reporting burden for this collection of information is estimated to average 1 hour per response, including the time for reviewing instructions, searching existing data sources, gathering and maintaining the data needed, and completing and reviewing the collection of information. Send comments regarding this burden estimate or any other aspect of this collection of information, including suggestions for reducing this burden, to Washington Headquarters Services, Directorate for Information Operations and Reports, 1215 Jefferson Davis Highway, Suite 1204, Arlington, VA 22202-4302, and to the Office of Management and Budget, Paperwork Reduction Project (0704-0188), Washington, DC 20503.

1. AGENCY USE ONLY (Leave blank) 2. REPORT DATE *1996* 3. REPORT TYPE AND DATES COVERED Reprint

4. TITLE AND SUBTITLE *✓*
Synthesis and Restructuring of Inorganic Nano-Particles in Counterflow Diffusion Flames

5. FUNDING NUMBERS
PE - 61102F
PR - 2308
SA - BS
G - F49620-94-1-0143

6. AUTHOR(S)
YANGCHUAN XING, ÜMIT Ö. KÖYLÜ,* and DANIEL E. ROSNER

7. PERFORMING ORGANIZATION NAME(S) AND ADDRESS(ES)
Yale University
High Temperature Reaction Engineering Laboratory
Department of Chemical Engineering
PO Box 208286 YS, New Haven, CT 06520-8286 USA

8. PERFORMING ORGANIZATION REPORT NUMBER

9. SPONSORING/MONITORING AGENCY NAME(S) AND ADDRESS(ES)
AFOSR/NA
110 Duncan Avenue, Suite B115
Bolling AFB DC 20332-0001

10. SPONSORING/MONITORING AGENCY REPORT NUMBER

11. SUPPLEMENTARY NOTES
COMBUSTION AND FLAME 107: 85-102 (1996)
Copyright © 1996 by The Combustion Institute
Published by Elsevier Science Inc.

12a. DISTRIBUTION/AVAILABILITY STATEMENT
Approved for public release; distribution is unlimited

12b. DISTRIBUTION CODE

13. ABSTRACT (Maximum 200 words)

The formation/growth/coagulation/sintering of flame-generated inorganic aggregates at low particle volume fractions ($O(10^{-1})$ ppm) was investigated. Al_2O_3 particles synthesized in a $AKCH_3$ (TMA)-seeded atmospheric pressure counterflow diffusion flame (CDF) fueled with $CH_4/O_2/N_2$ were used as the model material/combustion system. Experimental techniques included thermocouple, laser light scattering (LLS) and thermophoretic sampling/Transmission Electron Microscopy (TEM). Local aggregate morphology evolution was characterized in terms of "primary" particle size, aggregate size, and fractal structure. Additionally, the effects of temperature and TMA concentrations on morphology and size were also investigated systematically in the CDF. Light scattering signals as well as TEM analysis clearly illustrated particle/aggregate size and morphology evolution as a result of two competing processes, with coagulation increasing aggregate sizes, and sintering reducing aggregate surface areas. Mean "primary" particle diameters were found to be in the range of 13-47 nm, increasing with TMA concentration and sampling position (increasing residence time). On the other hand, mean aggregate sizes reached a maximum at about 4 nm above the bottom fuel duct (corresponding to a local temperature of only 1250 K) and increased with TMA seed level. Fractal dimension and fractal prefactor of alumina aggregates with negligible sintering rates were found to be 1.52 and 2.4, respectively. The final products were larger spherical particles with up to 60 nm diameter, resulting from complete "collapse" of the aggregates. These observations were shown to be compatible with our independent evaluation of the characteristic times associated with the participating rate processes in this class of two-phase CDFs. Systematic modification of these characteristic times can be used to control the size and morphology of flame-synthesized particles.

14. SUBJECT TERMS
nano-particle synthesis, sintering, thermophoretic particle sampling,
nano-particle formation/restructuring in flames, Brownian coagulation of aggregates

15. NUMBER OF PAGES
18

16. PRICE CODE

17. SECURITY CLASSIFICATION OF REPORT
Unclassified

18. SECURITY CLASSIFICATION OF THIS PAGE
Unclassified

19. SECURITY CLASSIFICATION OF ABSTRACT
Unclassified

20. LIMITATION OF ABSTRACT
UL

Synthesis and Restructuring of Inorganic Nano-Particles in Counterflow Diffusion Flames

YANGCHUAN XING, ÜMIT Ö. KÖYLÜ,* and DANIEL E. ROSNER
Yale Center for Combustion Studies, Department of Chemical Engineering, Yale University, New Haven, CT 06520-8286

The formation/growth/coagulation/sintering of flame-generated inorganic aggregates at low particle volume fractions ($C(10^{-1}$ ppm)) was investigated. Al_2O_3 particles synthesized in a $Al(CH_3)_3$ (TMA)-seeded atmospheric pressure counterflow diffusion flame (CDF) fueled with $CH_4/O_2/N_2$ were used as the model material/combustion system. Experimental techniques included thermocouple, laser light scattering (LLS) and thermophoretic sampling/Transmission Electron Microscopy (TEM). Local aggregate morphology evolution was characterized in terms of "primary" particle size, aggregate size, and fractal structure. Additionally, the effects of temperature and TMA concentrations on morphology and size were also investigated systematically in the CDF. Light scattering signals as well as TEM analysis clearly illustrated particle/aggregate size and morphology evolution as a result of two competing processes, with coagulation increasing aggregate sizes, and sintering reducing aggregate surface areas. Mean "primary" particle diameters were found to be in the range of 13–47 nm, increasing with TMA concentration and sampling position (increasing residence time). On the other hand, mean aggregate sizes reached a maximum at about 4 nm above the bottom fuel duct (corresponding to a local temperature of only 1250 K) and increased with TMA seed level. Fractal dimension and fractal prefactor of alumina aggregates with negligible sintering rates were found to be 1.52 and 2.4, respectively. The final products were larger spherical particles with up to 60 nm diameter, resulting from complete "collapse" of the aggregates. These observations were shown to be compatible with our independent evaluation of the characteristic times associated with the participating rate processes in this class of two-phase CDFs. Systematic modification of these characteristic times can be used to control the size and morphology of flame-synthesized particles.

NOMENCLATURE

a	"primary" particle radius	K	population-averaged collision frequency of aggregates, Eq. 10
A_s	projected area of aggregate constant, Eq. 13	K'	product of reaction rate constant and water vapor number density
b	constant, Eq. 13	L	projected maximum length of aggregate
b'	constant, Eq. 13	m	mass of particles/aggregates
c	dimensionless coefficient, Eq. 13	M	molecular weight
c_g	mean thermal speed of gas molecules	n	number density
d_a	area-equivalent diameter, Eq. 1	N	number of "primary" particles in an aggregate
d_p	"primary" particle diameter	N_A	Avogadro number
D	width-surface/width-grain boundary/volume diffusivity	r	hard sphere radius of molecule
D_f	fractal dimension	R	universal gas constant
I_s	scattered light intensity	R_a	area-equivalent radius
k	reaction rate constant for bimolecular collisions	R_g	radius of gyration
k_a	correlation coefficient, Eq. 2	Re	Reynolds number
k_B	Boltzmann constant	t	time
k_g	fractal prefactor, Eq. 3	t_c	characteristic coagulation time, Eq. 11
k_L	correlation coefficient, Eq. 4	t_H	characteristic TMA hydrolysis time, Eq. 8
		$t_{\text{heat}, e}$	thermal response time of aggregate

* Corresponding author.

COMBUSTION AND FLAME 107: 85–102 (1996)
 Copyright © 1996 by The Combustion Institute
 Published by Elsevier Science Inc.

0010-2180/96/\$15.00
 PII S0010-2180(96)00005-3

- t_L characteristic coalescence time for liquid particles, Eq. 15
- $t_{nom,a}$ stopping time of aggregate, Eq. 18
- t_R characteristic residence time, Eq. 16
- t_S characteristic sintering time for solid-(like) particles, Eq. 14
- t_T characteristic heating (cooling) time, Eq. 17
- T temperature
- u_z vertical velocity (z-direction)
- V_p volume of a primary particle
- x horizontal coordinate parallel to the length of the lower burner slot (see Fig. 1)
- y horizontal coordinate parallel to the width of the lower burner slot (see Fig. 1)
- z vertical height above the lower burner slot (see Fig. 1)

Greek Symbols

- α projected area exponent, Eq. 2
- α_{nom} momentum accommodation coefficient (gas/particle)
- β_{ij} collision frequency of particles
- δ neck radius
- ϕ_p particle volume fraction
- Φ equivalence ratio
- Γ nominal CDF strain rate
- μ_L viscosity of liquid alumina
- ρ_g density of host gas
- ρ_p density of alumina particles
- σ_L surface tension for liquid state
- σ_s surface energy for solid state
- ω width of surface layer
- ν molecular volume of alumina
- ξ reaction probability
- Ψ fuel-to-oxidizer momentum flux ratio

Subscripts

- a aggregate property or area-equivalent property
- A, B TMA and H₂O molecules, respectively
- p "primary" particle property

Superscripts

- () mean value over a population

INTRODUCTION

Inorganic particles produced during combustion processes are almost always coagulated due to Brownian motion and often partially sintered due to high temperatures [1-4]. Consequently, the resulting aggregates can be quite different in morphology and size according to the flame conditions under which they are generated and "processed." At low temperatures, particle/aggregate evolution is dominated by coagulation, which leads to tenuously-structured aggregates that can be described using fractal concepts [5, 6]. When the temperature level is sufficiently high to cause sintering, such aggregates may have time to undergo restructuring processes leading to more compact morphologies ($2 \leq D_f \leq 3$). Since the morphology of aggregates and their transport properties are interrelated [7, 8], it is important to understand not only synthesis but also the morphological evolution of aggregates in flames.

In this study, we examine a model laboratory system in which Al₂O₃ aggregates are formed and restructured in a well-characterized locally flat laminar counterflow diffusion flame (CDF). This flame configuration provided access via both laser light scattering (LLS) and thermophoretic sampling probes for Transmission Electron Microscopy (TEM) analysis. Our goal is to demonstrate quantitatively how an understanding and control of the relevant chemical and physical rate processes can be used to generate ultrafine inorganic oxides of tailored size and morphology in such combustion environments.

EXPERIMENTAL METHODS

Apparatus

Burner

A rectangular counterflow diffusion flame (CDF) burner, similar in dimensions to that first developed by Chung and Katz [9], was constructed as the combustion environment in which ultrafine particles can be generated and modified in a controllable manner. Figure 1 illustrates a schematic of the CDF burner, which consisted of two identical rectangular

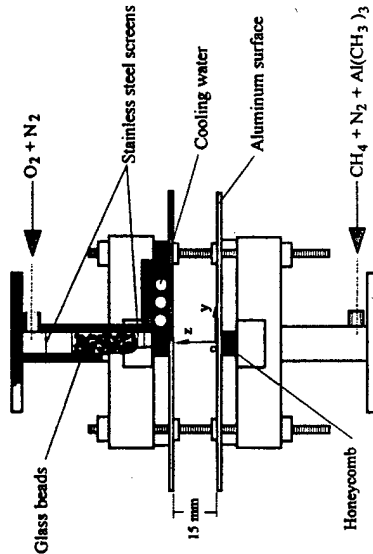


Fig. 1. Schematic of the rectangular counterflow diffusion flame (CDF) burner assembly.

slots positioned in vertically opposite directions. Each slot was divided into three channels by thin stainless steel sheets; a main channel (64 x 13 mm) for fuel/oxidizer/inert gases and two side channels (6 x 13 mm) for shroud gas. Each slot contained four wire screens (40 mesh), a 35 mm deep bed of glass beads (3 mm in diameter) and a honeycomb (40 mesh) in order to obtain uniform gas flows at the burner exits. Two aluminum plates (100 x 145 mm x 3 mm thick), both with rectangular openings identical to the size of the slots, were mounted at the slot mouths to confine and smooth the flow of exhaust gases. The upper and lower parts were separated by a distance of 15 mm using four adjustable screws. The burner was also water-cooled to minimize temperature increases with time at the burner surfaces during experiments. The entire burner assembly was mounted on a translation stage, which allowed positioning in all three directions. It should be noted that the origin of our cartesian coordinate system is considered to be at the center of the lower slot (see Fig. 1) so that $z = 15$ mm ($x = y = 0$) indicates the center of the upper burner surface.

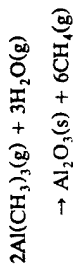
Methane and oxygen were introduced from the lower and upper main channels of the burner, respectively. Both fuel and oxidizer were diluted by nitrogen, which was also used as the shroud gas through the side channels. All gases were ultra purity level (99.99% or

higher). The flow rates were controlled using calibrated variable-area flowmeters within 5%. The fuel stream gases (i.e., CH₄ and N₂) were further dried and deoxidized by a gas purifier (Matheson 6412) to remove water vapor and oxygen amounts exceeding 0.5 and 0.1 ppm, respectively. CH₄/N₂ flowing upward and O₂/N₂ flowing downward formed a blue (non-sooting) flame sheet, which was stable and flat with uniform properties across the horizontal planes at fixed vertical directions, i.e., temperature, species concentrations and particle volume fraction were functions of only z . This one-dimensional feature, as will be discussed later on, makes the CDF burner an attractive configuration, i.e., a well-defined flame environment—for systematic studies of particle formation/evolution in diffusion flames [9].

Precursor

Liquid trimethylaluminum (TMA) was used as the precursor material to produce Al₂O₃ (alumina) particles. TMA (Strem Chemicals), containing 97% Al(CH₃)₃ and 3% AlH(CH₃)₂, was fed into an evaporator using a calibrated syringe (Hamilton 1001, 1 mL), which was controlled by a piston pump (Harvard Apparatus, 55-2226). The evaporator, a Pyrex tube (30 cm long and 3 cm diameter), was maintained at a temperature of 343 K using a heating tape to completely evaporate liquid TMA before being introduced to the burner. TMA reacts with

water vapor to produce alumina according to the following overall reaction:



During the present study, the evaporator was only connected to the fuel stream so that TMA reacted solely with flame-generated water vapor to form nanosized Al_2O_3 particles since, as discussed above, H_2O and O_2 in CH_4/N_2 gas stream were eliminated using a purifier before entering the evaporator. Extreme caution must be practiced in handling TMA since it can react with both oxygen and water vapor in room air even at a temperature of 300 K.

Instrumentation

Thermophoretic Sampling (TS)

Thermophoretic sampling procedures were based on our adaptation of the experimental and theoretical methods established by Dobbins and Megaridis [10] and Rosner et al. [11], respectively. The technique involved quick insertion of a cold sampling surface into the hot flame environment to extract representative organic particles/aggregates using the phenomenon of thermophoresis. The cold surfaces were carbon-supported 400 mesh copper TEM grids with a 3 mm diameter (Electron Microscopy Sciences, CF-H4-spec-Cu). Each grid had a solid square area at the center and a thicker copper arrow from the side toward the center which allowed accurate positioning. The grids were attached onto a circular recess at the tip of a stainless-steel probe. The sampling probe was stored outside the flames with an alignment parallel to the flow field. A double-action pneumatic cylinder with a 51-mm stroke rapidly inserted the probe to the desired sampling position in the CDF. A single probe was inserted into one position at a time to minimize disturbances to the flow field. The special grid type used, together with careful alignment with respect to the flame (using laser light and cathetometer) provided a spatial resolution of about 0.4 mm. The actuation of a four-way valve, determining the insertion, sampling and

retraction times, typically resulted in a total of 100-ms exposure. Sampling times, measured using a translation potentiometer with output recorded on a digital oscilloscope, were selected to be about 70 ms in order that the collected particles/aggregates covered no more than 10% of the TEM grid. Sampling in the CDF was done at the four vertical positions of $z = 2, 4, 6$ and 8 mm along the burner axis, i.e., $x = y = 0$.

TEM and Image Processing

The particles/aggregates extracted from several positions in the CDF burner were subsequently observed using a Zeiss EM-10A Transmission Electron Microscope. The microscope had a point-to-point resolution of 0.3 nm and a maximum magnification of 2×10^5 . The procedure to obtain images involved selecting aggregates randomly at relatively low magnifications near the center of our special grids. Aggregates were generally photographed at a magnification of 4×10^4 while additional photographs were taken at a magnification of 1.6×10^5 for obtaining detailed information regarding individual "primary" particles. The photographs taken at the TEM facility were ultimately digitized using a scanner (Microtek, ScanMaker IIG). The digitized images were saved on a personal computer and analyzed with image processing software (Media Cybernetics, Image-Pro Plus). Each pixel on the digitized computer images was represented by a gray level between 0 and 255 together with a pair of coordinate numbers. The TEM images were calibrated by photographing a calibration grid (1134 parallel lines/mm) at each magnification used and by digitizing/analyzing with the same hardware/software. This made it possible to obtain a precise conversion from pixels to nanometers on the digitized images, yielding resolutions of 2 and 0.5 nm/pixel for aggregates and primary particles, respectively. It should be emphasized that such high image resolution was necessary to accurately identify individual "primary" particles (ca. 20 nm diameter) in aggregates. The TEM measurements included "primary" particle diameters (d_p) and projected areas (A_d) and maximum lengths (L) of aggregates. Experimental uncertainties of these morphological measurements on any

INORGANIC NANO-PARTICLES IN DIFFUSION FLAMES

one aggregate/particle were expected to be less than 5%.

Laser Light Scattering (LLS)

Preliminary light scattering experiments were also conducted in order to supplement TS/TEM measurements. This involved a 5-W Ar-ion laser (Coherent, Innova 70) operating at 514.5 nm. The incident beam was first passed through a polarization rotator and then steered by a couple of mirrors towards the burner. The beam, modulated by a light chopper (EG & G, 197) at a frequency of 1200 Hz, was focused at the center of the burner ($x = y = 0$) using a 350 mm focal length lens. This resulted in a waist diameter of 160 μm with a confocal length of 140 mm. The scattered light was collected at 90 degrees using a 125 mm focal length lens, a polarizer, a laser line filter (1 nm bandwidth), and a photomultiplier tube (EMI, 9558B). The apertures in front of the collecting lens and PMT defined a solid angle of 0.2 mrad with a 1 mm long sampling volume at 90 degree scattering angle. The signal from the PMT was fed into a lock-in amplifier (EG & G, 5208) to discriminate unwanted photon sources, e.g., flame radiation, room light. The experimental uncertainties (95% confidence interval) of the LS measurements were estimated to be less than 10%, generally dominated by finite sampling times. Note that light extinction (transmission) measurement was not possible in these TMA-seeded CDFs because alumina particles do not appreciably absorb light, i.e., its refractive index is approximately real.

Thermocouple (TC)

Temperatures in the CDF reactor were measured using a Pt/Pt-6% Rh thermocouple in the absence of alumina particles since the seeding of the fuel with particle precursor (TMA) in such small amounts (vapor mole fractions of less than 0.24%) is estimated to affect the thermal field insignificantly (less than 50 K) in the CDF. The TC lead wires were 250 μm , resulting in a junction bead diameter of about 450 μm . These measurements involved insertion of the thermocouple into desired sampling position (along z axis, $x = y = 0$) and averaging the signal over 10 s. The TC output reading was corrected for radiative heat

transfer losses, which basically included a radiation/convection heat transfer balance assuming negligible lead loss by conduction due to TC assembly alignment with isotherms. Note that the Nusselt number was essentially equal to 2 for this low-velocity ($\text{Re} < 0.1$) flow around the spherical TC bead in the CDF. Additionally, the emissivity of the TC bead was calculated from $0.1(T/1000)^{0.76}$. Positioning of the TC was accomplished using a cathetometer with better than 0.5 mm accuracy. The experimental uncertainties (95% confidence interval) in temperature measurements were estimated to be generally less than 80 K, largely dominated by possible errors in the above-mentioned systematic radiation corrections (less than 265 K).

Flame Conditions

Several flames were tested at the beginning of this investigation; however, only one particularly suitable flame was chosen for a detailed study of the synthesis and restructuring of alumina particles. The experimental conditions for this laminar counterflow diffusion flame are summarized in Table 1. The fuel (CH_4/N_2) and oxidizer (O_2/N_2) gas flow rates were adjusted to obtain relatively high fuel-to-oxidizer momentum flux ratio ($\Psi = 3.5$) and small equivalence ratio ($\Phi = 0.68$). The sum of total fuel and oxidizer side exit velocities of 13.1 and 6.5 cm/s divided by the burner separation distance of 15 mm yielded a nominal strain rate of $\Gamma = 13 \text{ s}^{-1}$ for this CDF. These parameters, as will be discussed in detail in the next section, determine the general flame structure. Briefly, the location of gas stagnation plane is

TABLE I
Flame Conditions

Flow Rates* (cm ³ /s)		Flame Parameters					
Fuel Side	Oxidizer Side	N ₂	O ₂	N ₂	Ψ^b	Φ^c	Γ^d (s ⁻¹)
CH ₄	N ₂	79.6	43.5	3.4	3.5	0.68	13

* At normal temperature and pressure.

^b Fuel-to-oxidizer momentum flux (ρv_i^2 at burner exits) ratio.

^c Equivalence ratio.

^d Nominal strain rate.

controlled by Ψ , flame location by Φ , and residence time and flame temperature by Γ . Additionally, the effect of TMA concentration on the morphological evolution of alumina particles were studied using four different seed levels of 0.2, 0.4, 0.8 and 1.6 mL/h. These pumping rates yielded TMA vapor mole fractions of less than 0.24% entering the burner with the fuel stream, resulting in Al_2O_3 particle volume fractions less than 0.3 ppm in the flame. Finally, it is to be noted that the flame conditions were repeatable within 5% from one experiment to another.

RESULTS AND DISCUSSION

Flame Structure

Figure 2 shows as-measured and radiation-corrected temperatures as a function of vertical position, z , in our CDF reactor. Although high temperature gradients (ca. 450 K/mm) were present in the z direction, it was found that temperature variations in x - y planes at fixed z positions were always less than 1% for $|x| < 32$ mm, $|y| < 6.5$ mm. This observation, together with similar invariance of scattered signal in x - y planes, indicated that our flame was indeed flat and stable. As can be seen from Fig. 2, the maximum temperature was about 2270 K in the CDF after a radiation heat loss correction of ca. 265 K. The flame (FL) position, here defined by the location of this peak temperature, was at $z_{\text{FL}} = 6.3$ mm. The particle stagnation plane (PSP), measured from the falloff of the light scattering signal, was at $z_{\text{PSP}} = 8.7$ mm. The gas stagnation plane (GSP) was estimated to be near the particle stagnation plane ($z_{\text{GSP}} = 8.5$ mm) using z_{PSP} and the local $(dT/dz)/T$ [12]. Under the present test conditions, the general structure of our counterflow diffusion flame is illustrated in Fig. 3, which includes representative gas streamlines, thermophoretic sampling positions, particle and gas stagnation planes as well as flame position. The PSP is relatively close to the top burner exit allowing a larger spatial scale for evolution of alumina particles. In this flame structure, particles formed well below the flame (fuel side) can pass higher temperature regions and ultimately through the flame. Since particles

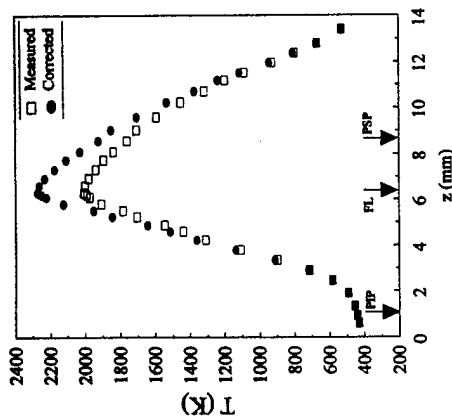


Fig. 2. As-measured and radiation-corrected temperatures as a function of vertical position z (at $x = y = 0$) in the CDF burner.

cannot cross and flow further upward in the burner beyond PSP, due to a balance of aerodynamic and thermal forces, the relative location of this plane dictates particle synthesis and restructuring processes in CDFs by controlling the temperature-time history of the particles [12-14].

Overview of Particle Synthesis and Restructuring in CDF

Figure 4 shows typical TEM photographs of alumina particles/aggregates thermophoretically extracted from four different vertical positions in our CDF reactor. Only the images corresponding to 0.8 mL/h TMA seed level (corresponding to a particle volume fraction of ca. 0.3 ppm) are illustrated since the particle/aggregate morphologies for other seeding levels were essentially similar. Note that the magnification for these four images is identical and equal to 8×10^4 . Figure 4 clearly demonstrates the evolution of alumina particles as they move from the particle inception plane (PIP) to the particle stagnation plane (PSP). PIP is the location at which the precursor (TMA) first reacts with the water vapor in the

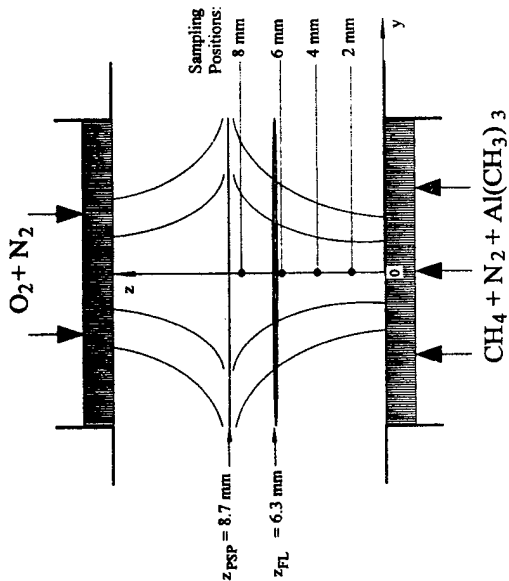


Fig. 3. General structure of the CDF, showing representative flow field, particle stagnation plane (PSP), flame position (FL), and thermophoretic sampling positions.

flame to form "embryonic" alumina particles. The PIP, taken to be at the onset of measurable light scattering intensity, was around 1.0 mm for this precursor seed level, shifting to slightly higher positions with increasing TMA concentration. Once the particles nucleate upon completing the chemical reaction step on a time scale estimated to be ca. 10 μs (see Fig. 9), they grow by chemical vapor deposition and coagulation with coalescence. At the lowest sampling position of $z = 2$ mm, "primary" particles are generally spherical and small (ca. 10-20 nm). These nearly monodisperse particles coagulate to form polydisperse aggregates as they flow upward from $z = 2$ mm to $z = 4$ mm. The aggregates observed at this point in the CDF structure are similar in morphology to other flame-generated materials (e.g., carbonaceous soot) probably due to the predominant cluster-cluster aggregation mechanism [5, 15]. However, as the aggregates move toward the flame, the coagulation rate drops, and they encounter higher temperatures, resulting in noticeable "coarsening." As the TEM image at $z = 6$ mm indicates, aggregates start collapsing

to more compact particles due to this sintering process. Obviously, the resulting nearly spherical single particles are larger than the "primary" particles in the parent aggregates. Sintering and aggregation processes contribute to the net growth of aggregates in opposite directions, i.e., sintering decreases the mean aggregate size, \bar{N} , whereas aggregation tends to increase \bar{N} . From $z = 6$ mm to $z = 8$ mm, the mixture of particles and aggregates crosses the flame (the highest temperature region) where sintering becomes the dominating mechanism. At the highest position of thermophoretic sampling, mostly single particles with diameters exceeding 50 nm are observed. Beyond this location, particles at most reach the PSP, at which they flow out of the burner. The above stages generally describe how the alumina evolves from small (sub-nanometer) "primary" particles to large aggregates ($z = 2$ -4 mm) and then aggregates to larger particles ($z = 4$ -8 mm) because of the thermal and flow structure of the counterflow diffusion flame. This is of great importance in many engineering applications in which the objective

200 nm

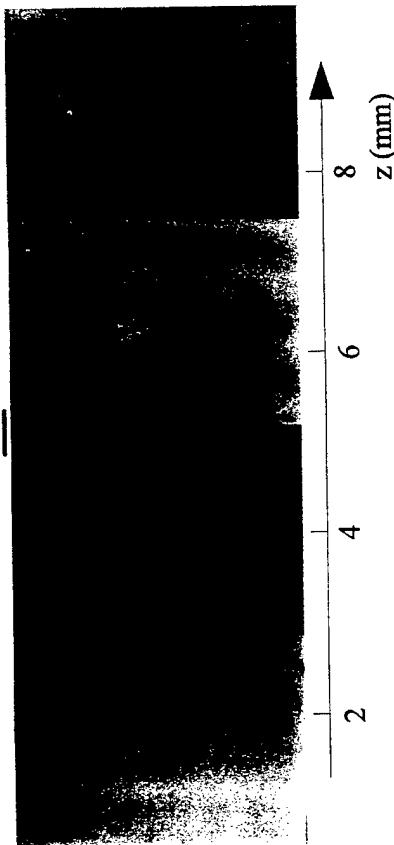


Fig. 4. Typical TEM images of alumina aggregates/particles thermophoretically extracted from four vertical positions in the CDF for 0.8 mL/h TMA concentration.

is to produce particles/aggregates with known size and morphology, in a controllable manner. To illustrate the use of CDF for particle production, the nucleation/growth/aggregation/sintering mechanisms will be quantified by analyzing our TEM and LLS results in detail below. The effect of precursor concentration on the particle/aggregate size and morphology will also be discussed.

"Primary" Particle Characteristics

"Primary" particle sizes represented here were measured directly from digitized TEM micrographs by detecting the apparent spherical profiles of the constituent particles near the peripheries of aggregates at relatively high microscope magnifications. When single particles rather than aggregated particles were present due to sintering at high temperatures, measurements of particle sizes simply involved the unambiguous diameters. Particles for a particular sampling condition are represented here by a mean diameter because of the narrow prevailing size distribution. Mean particle diameters, \bar{d}_p , were obtained by averaging over about 80 obvious particles at the corresponding sampling positions for each precursor concentration. The mean particle diameter as a function

of vertical position in our CDF burner is shown in Fig. 5 for four different TMA seed levels. The locations of the flame (FL) as well as the particle stagnation plane (PSP) are also indicated for reference. Mean "primary" particle diameters were measured to be in the range of

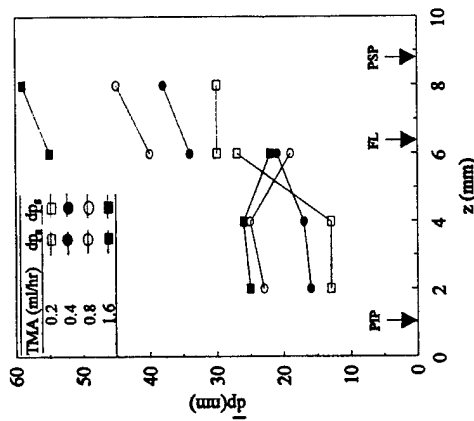


Fig. 5. Mean "primary" particle diameter as a function of vertical position in the CDF for various TMA seed levels.

13–25 nm at $z = 2$ mm, only about 1 mm downstream of the corresponding particle inception planes (PIP). Generally, the change in particle sizes for a specific precursor seed level was insignificant in low temperature regions, including $z = 2$ and 4 mm. In this region of the CDF, only aggregated particles were observed so that the \bar{d}_p results shown in Fig. 5 for these two lowest positions represented mean diameters of particles in aggregates. However, as the thermophoretic sampling location was moved to $z = 6$ mm, a mixture of single particles and aggregated particles started appearing on TEM grids. The difference in sizes between the unaggregated and aggregated particles were so significant that it was necessary to consider these two diameters separately at 6 mm. Consequently, Fig. 5 includes both mean particle sizes; one due to particles in aggregates, $\bar{d}_{p,a}$, and the other due to single (coalesced) particles, \bar{d}_p . As can be noticed, the mean diameter of aggregated particles changed slightly from 4 mm to 6 mm, following the similar trend from 2 mm to 4 mm. This observation implies that the growth rate of particles in the absence of sintering is relatively small in this CDF configuration. On the other hand, the mean diameter of single particles increased drastically for all precursor seedings at $z = 6$ mm, apparently due to sintering effects at high temperatures (this sampling position was the closest to the flame). For example, \bar{d}_p was 40 nm, compared with $\bar{d}_{p,a} = 19$ nm, at 6 mm for 0.8 mL/h TMA concentration. As the mixture of single and aggregated particles passed through the flame, most of the remaining aggregates continued to restructure into spherical forms, minimizing the free energy. Since the final alumina products were mostly compact particles resulting from the complete collapse of the aggregates in such a high-temperature environment, the largest single spherical particles, with mean diameters ranging from 30 to 58 nm, were measured at $z = 8$ mm in the CDF. It is also to be noted that \bar{d}_p increased slightly from $z = 6$ to 8 mm, which was the closest sampling location to PSP.

The effect of precursor concentration on the mean "primary" particle diameter in this particular CDF environment was also studied by considering four successively doubled TMA

seed levels. As can be seen in Fig. 5, from 0.2 mL/h to 1.6 mL/h of TMA, the mean diameter of particles within aggregates increased almost 100% for the sampling positions of $z = 2$ and 4 mm. Although coarsening of the aggregates made it somewhat difficult to accurately measure individual profiles of particles in aggregates at the higher position of 6 mm, the results indicated a relatively small variation of \bar{d}_p with respect to TMA concentration. However, as a result of sintering, \bar{d}_p clearly increased 100% as the TMA seed level was increased 8 times from 0.2 to 1.6 mL/h at this position close to the flame. Moreover, the difference between \bar{d}_p and $\bar{d}_{p,a}$ was higher for higher precursor concentration at $z = 6$ mm. Finally, similar behavior was observed at 8 mm, where a four fold TMA increase resulted in approximately doubling the final mean diameter of the sintered particles.

Aggregate Characteristics

After particles reach certain sizes (ca. 10 nm) at relatively low temperatures in our CDF, size dependent coalescence becomes too slow and these "primary" particles start forming tenuously-structured aggregates. Although the "primary" particles are nearly monodisperse, the variations in aggregate sizes are usually considerable, i.e., they are noticeably polydisperse. Generally, projected areas of aggregates, A_a , as well as their maximum lengths, L , can be directly measured from the analysis of TEM images. The area-equivalent diameter, d_a , is calculated as follows:

$$d_a = \left(\frac{4A_a}{\pi} \right)^{1/2} \quad (1)$$

This length scale, d_a , is related to the free molecule regime mobility diameter of aggregates and also to the number of particles contained in an aggregate [15–18]. Therefore, the area-equivalent diameters were calculated from the measured projected areas following Eq. 1 for 50 to 140 aggregates/particles at each sampling condition during the present investigation. d_a for alumina produced in the CDF was observed to lie mostly in the range of 20 to

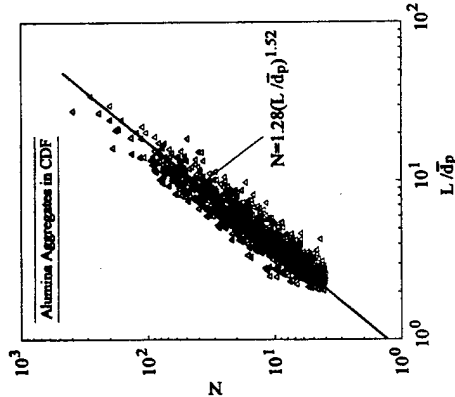


Fig. 7. Number of "primary" particles in an aggregate as a function of its normalized maximum projected length for more than 1000 alumina aggregates (with insignificant sintering) thermophoretically extracted from TMA-seeded CDF burner.

gyration, R_g [5, 6]:

$$N = k_g \left(\frac{2R_g}{d_p} \right)^{D_f} \quad (3)$$

where k_g , \bar{d}_p , and D_f are the fractal prefactor, mean "primary" particle diameter, and fractal dimension, respectively. It has been recently emphasized that k_g as well as D_f must be known in order to properly characterize the structure of combustion-generated fractal-like aggregates [15, 18]. Indeed, more elegant treatment of Neimark et al. [19] demonstrated that the aggregates produced in combustion environments are more precisely described as *self-affine* rather than self-similar objects.

Since the actual three-dimensional radii of gyration of aggregates are not readily available from the projected TEM images, an alternative form of Eq. 3 can be expressed as follows:

$$N = k_L \left(\frac{L}{\bar{d}_p} \right)^{D_f} \quad (4)$$

where the correlation constant, k_L , is related to k_g in Eq. 3 by

$$\frac{k_L}{k_g} = \left[\frac{(D_f + 2)}{D_f} \right]^{D_f/2} \quad (5)$$

Equation 5 was the result of the detailed analysis of Ref. 15, in which it was shown that this approximate relationship not only applies to straight chains ($D_f = 1$), disks ($D_f = 2$), and spheres ($D_f = 3$) but also to combustion-generated aggregates with $D_f \approx 1.7$ (within 10% accuracy).

Figure 7 illustrates the number of particles in an aggregate as a function of its maximum length (outer diameter) for more than 1000 alumina aggregates thermophoretically extracted from the TMA-seeded CDF. Note that maximum lengths of individual aggregates are normalized by the mean particle diameter associated for each sampling condition. The aggregates shown in Fig. 7 included only those with $N > 4$ and sampled from $z = 2, 4, 6$ mm so that the ones experiencing significant high temperature sintering were avoided. The least-square fit to this data in the form of Eq. 4

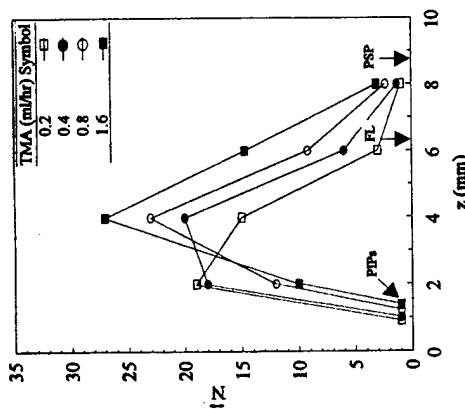


Fig. 6. Mean number of "primary" particles per aggregate as a function of vertical position in the CDF for various TMA seed levels.

200 nm. Additionally, the distribution of d_a at all sampling locations was found to be best represented by log-normal pdf's with geometric standard deviations in the range 1.4-1.9.

In order to quantify aggregate size and the degree of aggregation in the flame, the measurements of d_a were used to estimate the number of "primary" particles in aggregates (N), following the specific methods of Köylü et al. [15, 18], i.e.,

$$N = k_g \left(\frac{d_a}{\bar{d}_p} \right)^{2\alpha} \quad (2)$$

where $k_g = 1.15$, $\alpha = 1.09$, and \bar{d}_p represents the mean diameter averaged over all particles for a specific sample. Note that Eq. 2 can still be applied in the $N \rightarrow 1$ limit. The mean number of particles per aggregate (\bar{N}), calculated by averaging over 50-140 aggregates per sample, is illustrated as a function of the vertical position in Fig. 6 for the experimental conditions of the present study. Near PIP, aggregation starts presumably from a "burst" of quasi-spherical sub-nanometer single particles. In general, the mean number of particles per aggregate reached maximum values of 15 to 27 at $z = 4$ mm, after which \bar{N} decreased monotonically. The increase in \bar{N} at the beginning is obviously the result of the rapid Brownian-diffusion-driven aggregation process with negligible restructuring. On the other hand, the large increase in \bar{N} is due to sintering of these larger "primary" particles, accompanied by "coarsening" of the aggregates at sufficiently high temperatures. These two competing mechanisms changed surface areas of aggregates in the opposite directions. The z -location where \bar{N} peaks, which depends on the detailed kinetics of aggregation and sintering in any given experiment, was about 4 mm for the present experiments. Beyond this location, sintering effects became significant compared to aggregation, causing \bar{N} to approach unity near PSP, at which final alumina products were ejected from the CDF.

Figure 6 also shows the effect of TMA seed level on aggregate sizes. Noticeably, at $z = 2$ mm, \bar{N} increased from 10 to 19 as the TMA

concentration was reduced from 1.6 to 0.2 mg/L/h. This trend is rather different from the rest of the sampling positions in which an increase in the precursor seed level by 8-fold resulted in an corresponding increase of about 100% in \bar{N} . This behavior at 2 mm was evidently due to the shifting of PIP upwards in the flame with increasing precursor concentration, as will be discussed in detail later in conjunction with LLS results. Close to PSP ($z = 8$ mm), \bar{N} was near unity, implying that by then most of the aggregates had restructured into compact, nearly spherical shapes.

Fractal Characteristics

Prior to the onset of sintering at sufficiently high temperatures in our CDF, the alumina aggregates exhibited tenuous structures. We have verified below that the complex morphology of aggregates with wide size and shape variations can be characterized as mass fractals in the absence of surface energy driven restructuring. This implies the following statistical relationship between the number of particles in an aggregate, N , and its radius of

PSP, they completely collapsed to form single spherical particles due to significant sintering/coalescence rate process. In this case of compact shapes at $z = 8$ mm, $N \rightarrow 1$, implying $D_f \rightarrow 3$. This evolution of the fractal dimension from 1.5 to 3 is mainly the result of two competing processes: aggregation and sintering. When the aggregation was rapid enough to dominate sintering ($z < 6$ mm), the observed aggregates appeared tenuous and exhibited low fractal dimensions (< 2). As expected from a cluster-cluster aggregation mechanism, the aggregation process in our CDF increased the aggregate sizes but had little effect on the fractal dimension. However, when the sintering dominated, initially open structures became compact ($D_f \rightarrow 3$) within the high temperature regions of the flame. Note that in this limit of $N \rightarrow 1$, $k_f = (5/3)^{3/2} = 2.15$ since $R_f/d_p = (3/20)^{1/2}$ for a sphere. This implies that although sintering increases the fractal dimension [22], it has relatively small effect on the fractal prefactor.

In Situ LLS Evidence of Morphological Evolution

Figure 8 shows the LLS measurements of the present study for three TMA seed levels. The first noticeable feature of Fig. 8 is that the scattered intensity increased with increasing TMA concentration. Noting that, approximately, $I_s \propto n_s d_p^6 N$ [23], this is expected since a change in the precursor level, without considering other effects on morphology, directly corresponds to a change in particle number density. Additionally, as the TMA seed level was increased, PIP moved slightly to higher positions in the flame. This observation, together with the existence of a clear-cut onset of light scattering for each seed level, suggests that the extremely fast reaction of TMA is mainly controlled by the back-diffusion of water vapor produced in the "downstream" CH_4 combustion reaction.

The scattering results shown in Fig. 8 have similar profiles, implying that the alumina particles go through similar stages in the CDF for all TMA concentrations. Indeed, the steep in-

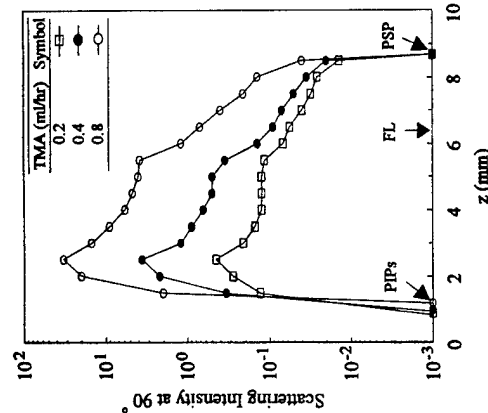


Fig. 8. Laser light scattering intensity at 90 degrees as a function of vertical position in the CDF for various TMA seed levels.

crease in scattering intensity from PIP up to 2.5 mm indicates that "primary" particle as well as aggregate sizes increase in this initial formation step. Moreover, the peak in the scattering intensity at about $z = 2.5$ mm was relatively insensitive to the precursor seed level. Considering that mean "primary" particle diameter does not change between 2 and 4 mm for a specific TMA level (see Fig. 5), this peak scattering intensity should correspond to a peak in number of primary particles per aggregate at around 2.5 mm. This is consistent with the TEM measurements shown in Fig. 6, which indicates that N increases to a peak at $z = 4$ mm (note that no thermophoretic sampling was available for $2 < z < 4$ mm). After $z = 2.5$ mm, the scattering intensity decreased slightly as a result of decreasing N since sintering started balancing the effect of coagulation. As seen from the plateau region in the light scattering between $z = 4$ and 5 mm, the competition between coagulation and sintering seemed to reach some kind of equilibrium state at these positions in the CDF. This local level-off in the scattering intensity in Fig. 8 is probably

stant, k , for a bimolecular reaction is given by [25]

$$k = \xi N_A \left[\left(\frac{8RT}{\pi} \right) \left(\frac{1}{M_A} + \frac{1}{M_B} \right) \right]^{1/2} \cdot (\pi r_{A,B}^2) \quad (6)$$

where subscripts A and B represent TMA and H_2O , respectively, ξ is the reaction probability normally less than unity, and $r_{A,B} = r_A + r_B$. In a batch system, the reaction rate is given as $dn_A/dt = -K'n_A$, where $K' = kn_B$. By neglecting the depletion of H_2O , K' can be taken as constant, resulting in the following relationship:

$$\frac{n_A}{n_A(0)} = \exp(-K't). \quad (7)$$

Then the TMA hydrolysis lifetime, here defined as the time when 99% TMA reacts with water vapor, can be expressed

$$t_H = \frac{4.6}{K'}. \quad (8)$$

Coagulation Time

The collision frequency of particles with rapid coalescence in the free molecular regime is given by [26]

$$\beta_{ij} = \left[\frac{8k_B T}{\pi} \left(\frac{1}{m_i} + \frac{1}{m_j} \right) \right]^{1/2} \cdot \pi (r_i + r_j)^2. \quad (9)$$

When the particles are so large as to not coalesce upon collision under given conditions, the above relation must be modified to apply to aggregates [27, 28]. In practice, it is convenient and sufficiently accurate to use the length scale $R_g (= d_p/2)$, easily obtainable from TEM measurements. Additionally, R_g correlates with the collision radius with a coefficient of the order of unity [16, 17, 27]. Therefore, the collision cross section for aggregates is expressed as $\pi(R_{g,i} + R_{g,j})^2$. The mass of the aggregate is related to the number of primary particles in the aggregate, i.e., $m = N(\rho_p V_p)$ with the volume of a primary particle being $V_p = \pi d_p^3/6$. Substituting these relationships into Eq. 9, and using the population-averaged values, we ob-

tain the result of a compromise between the increase in d_p and the decrease in N . Beyond $z = 5.5$ mm, the scattering intensity decreased continuously because of the dominant sintering mechanism at higher positions between flame and PSP. Therefore, a temperature of about 1900 K can be considered sufficient to cause significant collapse of these alumina aggregates. Finally, scattered laser light intensity drops to a molecular level at $z = 8.7$ mm (PSP) since the final alumina products, with spherical shapes, here exit the CDF burner.

The above in situ LLS results clearly track the morphology evolution of alumina from individual particles to aggregates due to coagulation (between PIP and $z = 2.5$ mm), aggregate restructuring due to the competition between coagulation and sintering (between $z = 2.5$ and 5.5 mm), and from aggregates to mostly compact particles due to high-temperature sintering (between $z = 5.5$ mm and PSP). In the next section these simultaneous processes are discussed in greater detail by considering their relevant characteristic times to obtain a better insight into the synthesis and restructuring of inorganic particles in such flame environments.

Restructuring and Characteristic Times

Since many rate processes occur simultaneously in the CDF, consideration of their characteristic times [24] is useful in gaining an understanding of this chemically reacting system. For the system at hand, viz. inorganic particle formation and evolution in CDFs, the following characteristic times are relevant: homogeneous chemical reaction times, coagulation times, coalescence times, flow (residence) time, and aggregate (momentum, heat transfer) response times. In any system in this broad class, these times completely control the size and morphology of the inorganic particles for tailoring the desired final product.

Reaction Time

Since the kinetic data for the TMA hydrolysis reaction is not readily available, we apply the bimolecular collision rate theory, assuming hard sphere collisions, to estimate the TMA hydrolysis time (t_H). The reaction rate con-

Y. XING, Ü. Ö. KÖYLÜ, AND D. E. ROSNER

tain

$$K = \beta \gamma_{T-N} - N_j = 16 \left(\frac{6k_g T}{\rho_p d_p^3 N} \right)^{1/2} \cdot R_s^2 \quad (10)$$

Then, the characteristic time for aggregate coagulation, t_c , defined as the average time between aggregate collisions, can be written [29]

$$t_c = \frac{2}{K n_s} \quad (11)$$

Assuming that the particles/aggregates follow the host fluid closely (which is the case here, see below), and that there are no further sources or sinks of particles, then the ratio of particle volume fraction (ϕ_p) and gas phase density (ρ_g) is conserved at any residence time in the flame, i.e., $\phi_p(t)/\rho_g(t) \approx$ constant. Since the initial volume fraction (near PIP) is known from the TMA seed level, this relationship can be used to estimate ϕ_p at any residence time, provided that $\rho_g(t)$ is also known. Therefore, the number density of aggregates, n_s , can be expressed as follows using the initially known quantities of $\phi_p(0)$ and $\rho_g(0)$:

$$n_s = \frac{\phi_p}{V_p N} = \left(\frac{\phi_p(0)}{\rho_g(0)} \right) \cdot \left(\frac{\rho_g}{V_p N} \right) \quad (12)$$

which can be used in Eq. 11 to estimate characteristic aggregate coagulation times in our CDF.

Sintering Times

Sintering is a very important physical phenomenon in the fabrication of various powder precursor materials. Mechanisms proposed for sintering include evaporation-condensation, condensed phase diffusion (volume diffusion, grain boundary diffusion, and surface diffusion) and surface-energy-driven viscous flow [30]. Most inorganic oxides, such as Al_2O_3 , TiO_2 , and SiO_2 , have very low vapor pressures even at high temperatures (say, 1000 K), making the first mechanism negligible for such particles. Thus, we only consider the last two mechanisms in the following.

¹ It is important to note that sintering models derived for hot-pressed granular materials may not be suitable for the relatively unpressed particles in flames.

and temperature, we also compute the characteristic stopping time, $t_{nom,s}$, and associated thermal response time, $t_{heat,s}$ [24] both evaluated in the free-molecular limit. According to Ref. 33, $t_{nom,s}$ will be larger than that of each of its primary particles by about the factor $1.02N^{0.14}$ (for $D_p \approx 1.8$) due to a slight "shielding" effect.² Accordingly, we estimate

$$t_{nom,s} \approx \frac{1}{\left(1 + \frac{\pi \alpha_{nom}}{8}\right)} \left(\frac{\rho_p}{\rho_g}\right) \cdot \left(\frac{a}{c_g}\right) \times (1.02N^{0.14}), \quad (18)$$

where \bar{c}_g is the mean thermal speed of background gas molecules. Since the specific heat capacity of the "primary" particles is close to that of the background gas, and the relevant gas/particle thermal accommodation coefficient is unlikely to be much smaller than unity, we can take $t_{heat,s}$ to be comparable to $t_{nom,s}$. In the following subsection we find that these aggregate response times are less than 1 μ s and, hence, smaller than the above-mentioned flow times by some 4 decades. We conclude that, apart from aggregate thermophoretic drift relative to the gas [12], aggregates in this CDF

² As found for the accessible area of fractal aggregates [7], these power laws are only locally valid approximations.

are strongly coupled to the local gas velocity and temperature.

Characteristic Time Map for Particle / Aggregate Formation / Evolution in CDF

While a more detailed theoretical treatment of the structure in our two-phase CDF, including particle morphology evolution, is beyond the scope of the present paper [34], our objective in this section is to elucidate the evolution processes of alumina particles with the help of the above-mentioned characteristic times. In calculating these times, the following assumptions and simplifications, in addition to the ones already discussed in the previous section, are considered to be suitable for the TMA-seeded CDF: (1) TMA hydrolysis is complete, i.e., all TMA reacts with water vapor to form alumina, implying that the "initial" solid volume fraction ($\phi_s(0)$) is known immediately beyond PIP. (2) Some bulk properties are approximately applicable even to "nanosized" particles. The physical data used in our present estimates are summarized in Table 2.

Figure 9 shows the characteristic times for alumina evolution in our CDF on an "Arrhenius-like" plane, i.e., logarithm of characteristic time vs. reciprocal absolute temperature. The flow times, t_R and t_T , were calcu-

TABLE 2 Data Used for Estimating Characteristics Times for Alumina Formation/Evolution in CDF

Property	Value	Reference
\bar{c}_g	1	
r_A	3.08 Å	Moore and Pearson [25]
r_B	1.41 Å	Mole and Jeffrey [40]
M_A	72.09 g/g-mol	Rosner [24]
M_B	18.02 g/g-mol	
σ_s	905 erg/cm ²	Dynys et al. [41]
σ_L	2797.24-0.8913T	Kingery [42]
ρ_p	3.97 g/cm ³	
$\phi_p(t=0)$	2.74×10^{-7} for a TMA seed level of 0.8 mL/h	
D	225 for surface diffusion; 120 for volume diffusion	Coblenz et al. [31]
$D = \omega D_s$	$1.89 \times 10^5 \exp(-80523/T)$ cm ² /s	Dynys et al. [41]
$D = D_v$	$1.36 \times 10^5 \exp(-69401/T)$ cm ² /s	Cannon et al. [43]
v	2.2×10^{-29} m ³	Dynys et al. [41]
μ_L	$1.12 \times 10^{-4} \exp(13832/T)$ Ns/m ²	Turkdogan [44]
$T_{melting point}(\alpha-Al_2O_3)$	2327 K	

^a Calculated from the stereo structure of TMA.

^b Calculated from Lennard-Jones size-parameter results.

For solid(-like) particles, surface- or bulk-diffusion may account for their sintering rates. For the three diffusion models reviewed by Coblenz et al. [31], the following relationship is generalized for the neck growth of two spherical particles at the initial stage:

$$\left(\frac{\delta}{a}\right)^b = \left(\frac{cD\omega t}{RTa^2}\right)^c \quad (13)$$

where $a = d_p/2$, $b = 5$, $b' = 3$ for volume diffusion, $b' = 4$ for grain boundary and surface diffusion, and c is a dimensionless coefficient, which also depends on the sintering processes. If Eq. 13 is formally extrapolated to the later stages, then the characteristic sintering time for two adjacent solid particles, t_s , can be expressed:

$$t_s = \frac{RTa^{b'}}{cD\omega r} \quad (14)$$

For the coalescence of liquid particles, surface-energy driven Newtonian viscous flow occurs and the following relationship should apply [32]:

$$t_L = \frac{\mu_L d_p}{\sigma_L} \quad (15)$$

Flow Times

A local residence time for any non-uniform steady flow system can be defined as $[v \cdot \text{grad}(\ln|v|)]^{-1}$, or in our CDF,

$$t_R = \left| \frac{dv_z}{dz} \right|^{-1} \quad (16)$$

where z is measured along the flow direction. This can be regarded as the residence time associated with an appreciable fractional change in fluid velocity. Perhaps more significant for temperature dependent processes is the characteristic time

$$t_T = \left| v_s \frac{d(\ln T)}{dz} \right|^{-1} \quad (17)$$

which is a measure of the local cooling (or heating) rate along the axial streamline.

Aggregate Response Times

To assess the ability of aggregates to "track" the above-mentioned changes in gas velocity

each of these chemical and physical processes. Indeed, these nanoparticles are able to restructure (collapse) by a condensed state diffusion-sintering process despite the fact that the peak flame temperature never reached the equilibrium melting point of crystalline Al_2O_3 . However, surface-energy-driven viscous flow restructuring was evidently too slow to prevent "fractal" aggregate formation even between 800 and 1800 K in this TMA-seeded CDF.

This research was sponsored by AFOSR Grant No. 94-1-0143 with J. M. Tishkoff serving as Technical Monitor, and the Yale High Temperature Chemical Reaction Engineering Laboratory Industrial Affiliates: DuPont and ALCOA. The authors would like to thank D. Albagli for the initial design of experimental apparatus, P. Tandon for his recent computational predictions of CDF structure, and C. S. McEnally for improving the accuracy of our thermocouple measurements of temperature.

REFERENCES

- Ulrich, G. D., and Subramanian, N. S., *Combust. Sci. Technol.* 17:119-126 (1977).
- Hebble, J. J., and Samoil, A. F., *J. Colloid Int. Sci.* 128:348-362 (1989).
- Zachariah, M. R., Chin, D., Semerjian, H. G., and Katz, J. L., *Combust. Flame* 78:287-298 (1989).
- Katz, J. L., and Hung, C.-H., *Combust. Sci. Technol.* 82:169-183 (1992).
- Jullien, R., and Bolet, R., *Aggregation and Fractal Aggregates*, World Scientific, Singapore, 1987.
- Feder, J., *Fractals*, Plenum, New York, 1988.
- Rosner, D. E., and Tandon, P., *AIChE J.* 40:1167-1182 (1994).
- Tandon, P., and Rosner, D. E., *Chem. Eng. Comm.*, in press.
- Chung, S.-L., and Katz, J. L., *Combust. Flame* 61:271-284 (1985).
- Dobbins, R. A., and Megaridis, C. M., *Langmuir* 3:254-259 (1987).
- Rosner, D. E., Mackowski, D. W., and Garcia-Ybarra, P., *Combust. Sci. Technol.* 80:87-101 (1991).
- Gomez, A., and Rosner, D. E., *Combust. Sci. Technol.* 89:335-362 (1993).
- Katz, J. L., and Miquel, P. F., *NanoStructured Mater.* 4:551-557 (1994).
- Miquel, P. F., Ph.D. thesis, Johns Hopkins University, 1995.
- Köylü, Ü. Ö., Xing, Y., and Rosner, D. E., *Langmuir* 11:4848-4854 (1995).
- Meakin, P., Donn, B., and Mulholland, G. W., *Langmuir* 5:510-518 (1989).
- Rogak, S. N., and Flagan, R. C., *Aerosol Sci. Tech.* 18:25-47 (1993).
- Köylü, Ü. Ö., Faeth, G. M., Farias, T. L., and Carvalho, M. G., *Combust. Flame* 100:621-633 (1995).
- Neimark, A. V., Köylü, Ü. Ö., and Rosner, D. E., *J. Colloid Int. Sci.*, in press.
- Megaridis, C. M., and Dobbins, R. A., *Combust. Sci. Technol.* 71:95-109 (1990).
- Köylü, Ü. Ö., and Faeth, G. M., *Combust. Flame* 89:140-156 (1992).
- Schmidt-Ott, A., *Appl. Phys. Lett.* 52:954-956 (1988).
- Köylü, Ü. Ö., and Faeth, G. M., *J. Heat Transf.* 116:152-159 (1994).
- Rosner, D. E., *Transport Processes in Chemically Reacting Flow Systems*, Butterworths, Boston, 1986 (1990, third printing).
- Moore, J. W., and Pearson, R. G., *Kinetics and Mechanism*, Wiley, New York, 1981.
- Hidy, G. M., and Brock, J. R., *Dynamics of Aerosol-Liquid Systems*, Pergamon, New York, 1970.
- Mulholland, G. W., Samson, R. J., Mountain, R. D., and Ernst, M. H., *Energy Fuels* 2:481-486 (1988).
- Masonkas, T., and Friedlander, S. K., *J. Colloid Int. Sci.* 146:505-506 (1991).
- Friedlander, S. K., *Smoke, Dust, and Haze*, Wiley, New York, 1977.
- Kingery, W. D., Bowen, H. K., and Uhlmann, D. R., *Introduction to Ceramics*, Wiley, New York, 1976.
- Coblentz, W. S., Dynys, J. M., Cannon, R. M., and Coble, R. L., *Mater. Sci. Res.* 13:141-157 (1980).
- Frenkel, J., *J. Phys.* 9:385-391 (1945).
- Cai, J., and Sorensen, C. M., *Phys. Rev. E* 50:3397-3400 (1994).
- Xing, Y., Köylü, Ü. Ö., Tandon, P., and Rosner, D. E., *Fifth World Congress of Chemical Engineering*, Paper No. 866, San Diego, 1996.
- Formenti, M., Juillet, P., Merlaud, P., Teichner, S. J., and Vergnon, P., *J. Colloid Int. Sci.* 39:79-89 (1972).
- Wu, M. K., Wideler, R. S., Steiner, C. K. R., Boris, T., and Friedlander, S. K., *Aerosol Sci. Technol.* 19:527-548 (1993).
- Rosner, D. E., Cohen, R. D., and Tandon, P., *AAAR Twelfth Annual Meeting*, Paper No. 8D4 (1993).
- Tandon, P., and Rosner, D. E., *J. & EC Res.* 34:3265-3277 (1995).
- Zachariah, M. R., and Semerjian, H. G., *AIChE J.* 35:2003-2012 (1989).
- Mole, T., and Jeffrey, E. A., *Organizationalism Compendium*, Elsevier, Amsterdam, 1972.
- Dynys, J. M., Coble, R. L., Coblentz, W. S., and Cannon, R. M., *Mater. Sci. Res.* 13:391-404 (1980).
- Kingery, W. D., *Property Measurements at High Temperature*, Wiley, New York, 1959.
- Cannon, R. M., Rhodes, W. H., and Heuser, A. H., *J. Am. Ceram. Soc.* 62:46-53 (1980).
- Turkdogan, E. T., *Physicochemical Properties of Molten Slags and Glasses*, The Metals Society, London, 1983.

Received 20 September 1995; revised 7 December 1995

REPORT DOCUMENTATION PAGE

Form Approved
OMB No. 0704-0188

Public reporting burden for this collection of information is estimated to average 1 hour per response, including the time for reviewing instructions, searching existing data sources, gathering and maintaining the data needed, and completing and reviewing the collection of information. Send comments regarding this burden estimate or any other aspect of this collection of information, including suggestions for reducing this burden, to Washington Headquarters Services, Directorate for Information Operations and Reports, 1215 Jefferson Davis Highway, Suite 1204, Arlington, VA 22202-4302, and to the Office of Management and Budget, Paperwork Reduction Project (0704-0188), Washington, DC 20503.

1. AGENCY USE ONLY (Leave blank)		2. REPORT DATE 1996	3. REPORT TYPE AND DATES COVERED Reprint	
4. TITLE AND SUBTITLE Jump, Slip, and Creep Boundary Conditions at Nonequilibrium Gas/Solid Interfaces [†]			5. FUNDING NUMBERS PE - 61102F PR - 2308 SA - BS G - F49620-94-1-0143	
6. AUTHOR(S) Daniel E. Rosner and Dimitrios H. Papadopoulos				
7. PERFORMING ORGANIZATION NAME(S) AND ADDRESS(ES) Yale University High Temperature Chemical Reaction Engineering Laboratory Department of Chemical Engineering PO Box 208286 YS, New Haven, CT 06520-8286 USA			8. PERFORMING ORGANIZATION REPORT NUMBER	
9. SPONSORING/MONITORING AGENCY NAME(S) AND ADDRESS(ES) AFOSR/NA 110 Duncan Avenue, Suite B115 Bolling AFB DC 20332-0001			10. SPONSORING/MONITORING AGENCY REPORT NUMBER	
11. SUPPLEMENTARY NOTES Ind. Eng. Chem. Res. 1996, 35, 3210-3222				
12a. DISTRIBUTION/AVAILABILITY STATEMENT Approved for public release; distribution is unlimited			12b. DISTRIBUTION CODE	
13. ABSTRACT (Maximum 200 words) <p>The notion of <i>local</i> (dynamical, thermal, and chemical) <i>equilibrium</i> at fluid/solid interfaces which are the site of interesting <i>nonequilibrium</i> processes has proven useful to engineers for nearly a century and provides the basis for widely used methods described in textbooks on <i>Transport Processes</i>. Indeed, <i>continuity</i> of tangential velocity ("no-slip"), temperature, and species chemical potential are usually treated as "commandments", rather than often-useful approximations! However, in many current and emerging applications this class of approximations becomes unacceptable for easily understood reasons. We illustrate this here for <i>ideal gas/solid interfaces</i> across which, or tangent to, there are nonzero molecular fluxes of momentum, energy, and/or species mass. We make use of the concept of a <i>Knudsen sublayer</i>, at most several gaseous mean-free paths thick, inevitably present adjacent to the solid surface. While many scientific aspects of these phenomena have been known since the earliest studies of J. C. Maxwell (1879), we show that their engineering importance is now such that their understanding should be part of the education of all chemical engineers. Moreover, molecular-level numerical techniques can now be brought to bear to illuminate the nature of these near-interfacial regions, under more realistic nonequilibrium circumstances. Analogous phenomena occur in <i>dense vapor/solid</i> and <i>liquid/solid</i> cases. Such systems, far less well understood theoretically, are characterized by effects which are smaller numerically but which may still be quite exploitable (as for separations (Giddings, 1991; Caldwell, 1988)).</p>				
14. SUBJECT TERMS boundary conditions, gas/solid interfaces, thermal creep, temperature jump, Knudsen sublayer, accommodation coefficients			15. NUMBER OF PAGES 13	
			16. PRICE CODE	
17. SECURITY CLASSIFICATION OF REPORT Unclassified	18. SECURITY CLASSIFICATION OF THIS PAGE Unclassified	19. SECURITY CLASSIFICATION OF ABSTRACT Unclassified	20. LIMITATION OF ABSTRACT UL	

Jump, Slip, and Creep Boundary Conditions at Nonequilibrium Gas/Solid Interfaces¹

Daniel E. Rosner^{2*} and Dimitrios H. Papadopoulos

High Temperature Chemical Reaction Engineering Laboratory, Chemical Engineering Department, Yale University, New Haven, Connecticut 06520-8286

The notion of *local* (dynamical, thermal, and chemical) equilibrium at fluid/solid interfaces which are the site of interesting nonequilibrium processes has proven useful to engineers for nearly a century and provides the basis for widely used methods described in textbooks on Transport Processes. Indeed, continuity of tangential velocity ("no-slip"), temperature, and species chemical potential are usually treated as "commandments", rather than often-useful approximations! However, in many current and emerging applications this class of approximations becomes unacceptable for easily understood reasons. We illustrate this here for *ideal gas/solid interfaces* across which, or tangent to, there are nonzero molecular fluxes of momentum, energy, and/or species mass. We make use of the concept of a *Knudsen sublayer*, at most several gaseous mean-free paths thick, inevitably present adjacent to the solid surface. While many scientific aspects of these phenomena have been known since the earliest studies of J. C. Maxwell (1879), we show that their engineering importance is now such that their understanding should be part of the education of all chemical engineers. Moreover, molecular-level numerical techniques can now be brought to bear to illuminate the nature of these near-interfacial regions, under more realistic nonequilibrium circumstances. Analogous phenomena occur in *dense vapor/solid* and *liquid/solid* cases. Such systems, far less well understood theoretically, are characterized by effects which are smaller numerically but which may still be quite exploitable (as for separations (Giddings, 1991; Caldwell, 1988)).

1. Introduction

The assumption of continuity of tangential velocity ("no-slip"), temperature, and Gibbs chemical potentials across interfaces between phases is so deeply ingrained in the psyche of engineers that certain pitfalls and missed opportunities are inevitable in dealing with nonequilibrium applications of current importance. This is especially true for either gaseous systems at subatmospheric pressure or systems with small dimension, on which we focus here. Because of the current importance of "dry" semiconductor processing reactors (for selective etching, chemical vapor deposition, local-ized doping, ...) and emerging "nanotechnologies" (synthesis and unique properties of solid materials at the or. 10 nm scale), it would be prudent for chemical engineers to understand the conditions under which the above-mentioned continuity of tangential velocity, temperature, and Gibbs chemical potentials break down and the engineering consequences thereof. Because ChEs appear to have little difficulty with the concept of chemical (species) nonequilibrium¹ at gas/catalytic solid interfaces (because very low chemical reaction probabilities are the rule rather than the exception), our examples, starting with the most familiar, will deal with drag reduction, heat-transfer reduction, particle thermophoresis (Rosner et al., 1991), and convection driven by nonequilibrium walls in crystal growth ampoules (Rosner, 1989; Papadopoulos and Rosner, 1995). In all cases we will emphasize ideal gas systems satisfying the necessary conditions: $t_f \gg \lambda \gg \sigma$, where t_f is the gas molecule mean-free path, λ is the gas number density ($\rho/\mathcal{M}T$), and σ is the effective molecular diameter. Moreover, we focus on the near-continuum limit in which t_f is much smaller than the

¹ Dedicated in honor of Eli Ruckenstein's 70th birthday.
² Professor/Chair, Chemical Engineering, Director Yale HT-CRE Laboratory.

08988-5885(90)00035-6 CCC: \$12.00

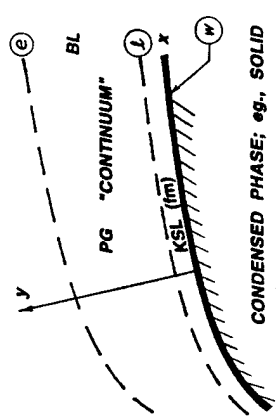


Figure 1. Configuration considered and station nomenclature: boundary layer (BL) and Knudsen sublayer (KSL) adjacent to solid surface; energy, momentum, energy, and/or species mass with a moving "perfect" (ideal) gas (PG); $L \gg \lambda \gg \sigma$, $\lambda \gg \sigma$, concentration gradients tangent to the surface, outlining old and new approaches to deriving the associated tangential "creep" velocities. Section 4 describes several instructive applications in which these KSL phenomena have important macroscopic consequences, even in the near-continuum ($Kn \approx \lambda/L \ll 1$) limit. Section 5 concludes with necessary generalizations of these results/methods and the "lessons" to be learned from these "old" and "new" examples.

2. Slip and Jump Boundary Conditions: Diffusion Fluxes Across Gas/Solid Interfaces

As indicated above, a troublesome question for most engineering students and designers, and one with which we believe, they have not been adequately prepared to deal, is the question of when "local equilibrium" can be assumed to prevail at interfaces, even in the presence of nonequilibrium phenomena—i.e., in the presence of nonzero fluxes of tangential momentum, energy, and/or species mass. In most textbooks one finds the usual "commandments", such as the no-slip condition (of classical viscous fluid mechanics) or continuity of temperature between phases, leaving the student with the false impression that these postulates stand on an equal footing with the principles of conservation of mass, momentum, and energy. Corollaries of this confusion are the inability to assess when these commandments will lead one far astray and an inability to deal with nonequilibrium physicochemical situations in which such field variables as the tangential velocity, temperature, and chemical potentials undergo significant "jumps" across the interfaces (Rosner, 1976, 1986). We discuss here the types of systems in which such jumps can be expected and how these inevitable jumps depend on the net transport fluxes across, or tangent to, the interfacial region. We acquaint the reader with the important notion that interfaces, like bulk phases, have transport properties and associated transport "resistances". We deliberately demonstrated these concepts below in very simple terms for perhaps the best understood interfacial region—viz., that comprised of the so-called *Knudsen sublayer* (with thickness on the order of a few gas mean-free paths) which inevitably exists between a gaseous continuum and an adjacent condensed (e.g., smooth impenetrable solid) phase continuum. It is hoped that this elementary presentation clarifies the essential points and will facilitate the incorporation of this subject matter in engineering courses on momentum, energy, and/or mass transport (Rosner, 1976, 1986).

This paper will be structured as follows. In section 2 we consider the momentum, energy, and mass-transport consequences of the thin Knudsen sublayer when there is molecular transport across the interface (i.e., in the direction of the outward normal; Figure 1), associated with large components of the gradient of all field variables in that direction. Section 3 deals with the considerably less familiar case of large temperature or

2.1. Jump Conditions at a Gas/Solid Interface. For definiteness, consider a gas/solid interface (Figure 1) across which there is a transfer of tangential momentum, energy, and/or species mass \rightarrow e.g., a gas/not catalytic solid interface subject to a tangential stress (friction drag), heat transfer, and a net normal flux of some species (reactant A present in the gas). We adopt the local coordinates x (along the surface) and y (normal to the surface) and measure velocities relative to the solid surface itself. The surface is considered smooth on the scale of t_f , and subscript t will denote tangential.

The conservation constraints alone certainly admit jumps in many field variables (e.g., $v_t(0^+) \neq 0$, $T(0^+) \neq T_w$, $\gamma_A(0^+) \neq \gamma_A(LTCS)$) associated with the dynamical, thermal, and chemical nonequilibrium. In what follows, using a simple yet rather general approach, we derive the jump conditions which must prevail at a gas/condensed phase interface across which there is a net transfer of tangential momentum, energy, and/or species mass. Basically, in addition to the battle-tested conservation laws, we introduce the transport (constitutive) laws governing the interfacial region in question (in this case the Knudsen sublayer (see Section 2.3)), along with the familiar transport laws governing the (apparently) adjacent continua (section 2.2).

2.2. Diffusion through the Gaseous Continuum. The diffusion of tangential momentum, energy, and species mass normal to the interfaces across the gaseous continuum is governed by simple "gradient" laws (Rosner, 1986), such as:

$$-T_x = -\mu \frac{\partial v_t}{\partial y} \quad (2-1)$$

$$q_y' = -k \frac{\partial T}{\partial y} = -\frac{c_p}{Pr} \mu \frac{\partial T}{\partial y} \quad (2-2)$$

$$J_{y,z} = -D_{yz} \frac{\partial m_i}{\partial y} = -\frac{m_i}{n} \frac{\partial v_i}{\partial y} \quad (2-3)$$

where μ is the gas viscosity ($\approx (1/2)\rho\lambda$), k_g is the gas thermal conductivity, and D_{yz} is the Fick diffusivity for species i ($i = A, B, \dots$), and, for simplicity, we neglect thermal diffusion vapor mass transfer.

2.3. Net Transport across the Knudsen Sublayer. The net fluxes across a thin³ (locally planar) Knudsen sublayer (KSL) are governed by laws of a rather different kind (see, e.g., Edwards et al., 1978, who assume $\alpha = 1$), e.g.:

$$-T_x = -\alpha_{\text{mom}} Z'' \tau_{\text{mom}}(t_f) \quad (2-4)$$

$$q_y' = \alpha_{\text{en}} Z'' \left(C_p - \frac{Pr}{2} \right) T_w - T q_y \quad (2-5)$$

$$J_{y,z} = \alpha_{\text{sp}} Z'' \tau_{\text{sp}}(t_f) - \gamma_i(t_f) \quad (2-6)$$

where Z'' ($\approx (1/4)\rho\lambda$) is the local flux of all molecules in one direction across each area (e.g., in the "plane" $y = \text{const.}$), and the α values, essentially defined by these equations, describe the nature of the gaseous molecule/molecule interactions with the solid surface; i.e., $\alpha_{\text{mom}} = \text{molecule/interfacial momentum accommodation coefficient}$ ($0 \leq \alpha_{\text{mom}} \leq 1$), $\alpha_{\text{en}} = \text{molecule/interfacial energy accommodation coefficient}$ ($0 \leq \alpha_{\text{en}} \leq 1$), $\alpha_{\text{sp}} = \text{molecule/interfacial mass accommodation coefficient}$ ($0 \leq \alpha_{\text{sp}} \leq 1$). These normalized coefficients are, in effect, dimensionless rate "constants" accessible to measurement and, in some cases, a molecular theory. Also noteworthy is the

effective (molar) heat capacity $C_p - (R/2)$ appearing in eq 2-6. This is a consequence of the fact that the average translational kinetic energy of the molecules crossing each plane $y = \text{const.}$ is $2kT$ per molecule (not $(3/2)kT$; see, e.g., Edwards et al., 1979, section 6.6.9) and has interesting consequences when applied to energetic surface reactions at low densities (Kiela et al., 1984). Equations 2-6, as written, allow for the transport of energy beyond translational—i.e., $C_p \geq (5/2)R$, in which case α is an overall effective energy accommodation coefficient. Finally, we remark that eq 2-6 neglects minor complications associated with *stimulated* mass transfer.

2.4. "Matching" the Gas BL to the KSL. Suppose the Knudsen sublayer is sufficiently thin, or the surface sufficiently flat, that, by conservation, the fluxes of tangential momentum, energy, and species mass are the same across the GKSL and KSL/solid "interfaces". Then, since we can assume the field variables themselves are continuous across $y = l_g$, we can write:

$$(-\tau_y)_0 = (-\tau_y)_{KSL} \quad (2-7)$$

$$(q_y^0)_0 = (q_y^0)_{KSL} \quad (2-8)$$

$$(f_y^0)_0 = (f_y^0)_{KSL} \quad (2-9)$$

Each of the field variables evaluated at $y = l_g$ (cf. eqs 2-4-2-6) can be expressed in terms of its value at (projected to) $y = 0$ via a (truncated) Taylor series:

$$v_i(y_g) = v_i(0^+) + \left(\frac{\partial v_i}{\partial y}\right)_{y=0^+} l_g + \text{h.o.t.} \quad (2-10)$$

with similar estimates for T and y_i . Combining these relations and solving for the corresponding non-equilibrium jumps, we readily find the local "slip" (jump) boundary conditions:

$$v_i(0^+) = \left(1 - \frac{1}{2}\frac{\alpha_{m_{i,j}}}{\alpha_{m_{m,j}}}\right) \left(2l_g \left(\frac{\partial v_i}{\partial y}\right)_{y=0^+}\right) \quad (2-11)$$

$$T_w - T(0^+) = \left(\frac{1 - \frac{1}{2}\alpha_c}{\alpha_c}\right) \left(2l_g \left(\frac{-\partial T}{\partial y}\right)_{y=0^+}\right) \quad (2-12)$$

$$y_{i,j} \alpha_{m_{i,j}} \text{LUTCEB} - y_i(0^+) = \left(\frac{1 - \frac{1}{2}\alpha_{m_{i,j}}}{\alpha_{m_{i,j}}}\right) \left(2l_g \left(\frac{-\partial y_i}{\partial y}\right)_{y=0^+}\right) \quad (2-13)$$

where

$$\alpha_c = \alpha_m \left(\frac{l_g + 1}{2l_g}\right) \tau \quad (2-14)$$

$$\alpha_{m_{i,j}} = Sc_{i,j}^{1/2} \alpha_{m,j} \quad (2-15)$$

This level of approximation will be sufficient for the following purposes.

2.5. Conclusions Regarding Discontinuities at the G/S Interface. It is now instructive to introduce the gaseous boundary layer "slope" thicknesses: δ_{mom} , δ_h , and δ_f , defined by the analogous expressions:

$$\left(\frac{\partial v_i}{\partial y}\right)_{y=0^+} = \frac{U - v_i(0^+)}{\delta_{\text{mom}}} \quad (2-16)$$

where $U = v_{i,e}$

$$\left(\frac{-\partial T}{\partial y}\right)_{y=0^+} = \frac{T(0^+) - T_w}{\delta_h} \quad (2-17)$$

$$\left(\frac{-\partial y_i}{\partial y}\right)_{y=0^+} = \frac{y_i(0^+) - y_{i,e}}{\delta_{f,i}} \quad (2-18)$$

For our present purposes these BL slope thicknesses will be estimated from their corresponding values in the continuum limit ($l_g \rightarrow 0$). In terms of the corresponding Knudsen numbers defined as follows:

$$Kn = l_g/\delta \quad (2-19)$$

(where δ refers to the appropriate boundary layer thickness), eqs 2-11-2-13 can now be written in the instructive *dimensionless* forms:

$$\frac{v_i(0^+)}{U} = \left\{1 + \left(\frac{\alpha_{m_{i,j}}}{1 - \frac{1}{2}\alpha_{m_{i,j}}}\right) \frac{1}{2Kn_{m,j}}\right\}^{-1} \quad (2-20)$$

$$\frac{T_w - T(0^+)}{T_w - T_e} = \left\{1 + \left(\frac{\alpha_c}{1 - \frac{1}{2}\alpha_c}\right) \frac{1}{2Kn_h}\right\}^{-1} \quad (2-21)$$

$$\frac{y_{i,j} \alpha_{m_{i,j}} \text{LUTCEB} - y_i(0^+)}{y_{i,j} \alpha_{m_{i,j}} \text{LUTCEB} - y_{i,e}} = \left\{1 + \left(\frac{\alpha_{m_{i,j}}}{1 - \frac{1}{2}\alpha_{m_{i,j}}}\right) \frac{1}{2Kn_{m,j}}\right\}^{-1} \quad (2-22)$$

Inspection of these analogous equations leads to the following important conclusions:

C1. Whenever the diffusion fluxes of tangential momentum $-\tau_y$, energy q_y^0 , and/or species mass f_y^0 evaluated at the wall ($y = 0^+$) are nonzero (i.e., whenever there is a departure from strict mechanical, thermal, and/or chemical equilibrium), there must be corresponding nonzero jumps in the associated field variables at the gas/solid interface.

C2. Only when $2Kn_m/(1 - (1/2)Kn_m) \ll 1$ do these jumps become negligible, leading to the often-quoted no-slip (jump) conditions. Note that $Kn \ll 1$ is *not sufficient* to neglect such a jump if the corresponding *effective accommodation coefficient*, α (eqs 2-14 and 2-15), is itself very small! (see sections 3 and 4).

C3. When α is near unity, then the condition $Kn \ll 1$ ensures approximate local equilibrium. In such cases jumps can only be important under rarefied (noncontinuum) BL gas flow conditions.

Regarding the effects of accommodation coefficient and Knudsen number (when $Kn \ll 1$) on near-continuum momentum, energy, and mass-transfer rates, since $N_{0,i}(0) = L/\delta_h$, etc., eqs 2-20-2-22 immediately imply the success of correlations of the simple non-dimensional form:

$$C_i = \frac{C_i(0)}{1 + \text{const.} Kn_i Re C_i} \quad (2-23)$$

and

irrespective of direction and speed, a fraction $1 - \alpha$ reflects with zero accommodation—i.e., "specularly, and with the fraction α adsorbs and is later resmitted "diffusely", with no memory of its initial state.

3. "Creep" Conditions: Energy and/or Mass Diffusion Fluxes Parallel to Surfaces

Less familiar, but of growing importance, are systems in which appreciable energy and/or mass diffusion fluxes occur parallel to the solid surface.

3.1. Thermal Creep. The first example of this type was pointed out as early as 1879 by J. C. Maxwell in explaining both the popular "radiometer" effect and O. Reynolds' experimental observations on nonisothermal porous "membrane" gas flow (see, e.g., Brush and Everett, 1969). Without a detailed KSL analysis Maxwell demonstrated that, if $T_w(0^+) \neq 0$, this must be associated with a tangential mass-averaged velocity (directed from cold-to-hot) of about:

$$v_x(0^+) = v_{x,w} = (3/4) \gamma_g (\delta \ln T_w) / (\delta x) \quad (3-1)$$

(see, e.g., Kennard, 1938, who comments that "molecules impinge obliquely upon it (this nonisothermal solid surface) strike it with higher average velocity when they come from the hotter region than when they come from the colder, and so are kicked back more strongly by the wall...with the result that the gas acquires tangential momentum directed toward the hotter side"). Here, as before, γ_g is the momentum diffusivity ("kinematic viscosity", μ/ρ) of the gas, approximately given by $(1/2) \tau_{T_g}$, where τ_{T_g} is the mean thermal speed of the gas molecules. More refined KSL structure analyses based on a linearized Boltzmann equation led to theoretical "creep velocity" results of the same order of magnitude but with the numerical constant $3/4$ replaced by a dimensionless coefficient, C_t , weakly dependent upon both α_{mass} (TMAC) and the nature of the gas intermolecular force law (see, e.g., Kogan, 1973; Loyalka and Cipolla, 1971). The tangential thermal creep velocity $v_x(0^+)$ must be added to (or subtracted from) the α_{mass} (TMAC)-sensitive slip velocity presented in section 2 above both velocities being linearly proportional to the mean-free path l_g . Two applications in which the thermal creep effect dominates, and has important macroscopic consequences even when $Kn_g \ll 1$, are discussed in section 4 below. One deals with suspended solid particle migration in a nonisothermal gas—i.e., "particle thermophoresis". The second deals with circulating flows induced (even in the absence of gravity) in nonisothermal vapor ampules used to grow crystals.

3.2. Concentration Creep. The species mass-transfer analog of thermal creep is, as might be expected, associated with concentration gradients along solid surfaces. For binary mixtures this was apparently first pointed out and estimated for Maxwell molecules and diffuse reflection ($\alpha_{\text{mass}} = 1$) by Kramers and Kistemaker (1943) and subsequently refined by, among others, Loyalka (1971) and Mason and Chapman (1962). These authors provide expressions for the dimensionless *diffusional creep coefficient* C_{12} , appearing in:

$$v_x^i(0^+) = C_{12} D_{12} (\delta \ln y_i / \delta x)_{y=0} \quad (3-2)$$

where D_{12} is the Fick binary diffusion coefficient, y_i is the mole fraction of species i , and, for a given intermolecular force law, we expect

$$Nu = \frac{Nu(0)}{1 + \text{const.} Kn_i Nu(0)} \quad (2-24)$$

where $\text{const.} = 2(1 - (1/2)\alpha) \alpha_{m,i} = \alpha_{\text{mass}}$, α_c , or $\alpha_{m,i}$, C_i is a dimensionless friction factor (Roemer, 1986). $Nu = Nu_h$ or Nu_m for heat or mass transfer, respectively (Roemer, 1986). Kn is based on the same reference length used in the definition of the non-dimensional fluxes: C_h , Nu_h , and Nu_m , and the superscript (0) pertains to the continuum (no-slip) limit, all other conditions being held constant. Some practical consequences of eqs 2-23 and 2-24 will be taken up in section 4.

Concerning our second point, early experimental values of α_{mass} (TMAC) and α_c (EAC) (see, e.g., the survey of Schaaf and Chambre, 1958) indicated that they were close to unity ($0.79 \leq \alpha \leq 1$), undoubtedly because they all pertained to surfaces which were either "rough", contaminated with adsorbed gases, and/or pertained to gas/solid systems which did not have sufficiently dispersive molecular weights. However, more recent measurements (Saxena and Joshi, 1989) as well as theory (see, e.g., Goodman and Wachtman, 1976), indicate that, for sufficiently smooth, clean solid surfaces struck by much lighter (or heavier) gas molecules, α values much lower than unity are expected and observed. While the lowest TMAC value inferred from Shields' (1983) gas-in-capillary sound-speed measurements was 0.55 (for He(g) on clean Pt(s)), he inferred EAC values as low as about 0.07 for this system. For ca. 60% of $N_2H_4(g)$ molecules reflecting off Ir(s) decomposition catalyst between 1300 and 2100 K, earlier work in this laboratory (Kiela et al., 1984) indicated values of EAC near $1/2$. More dramatically, for the He(g)/W(s) system EAC ≈ 0.005 (Aihara et al., 1987). Clearly, such systems will exhibit large departures from no-slip, no (temperature) jump behavior, even in the near-continuum ($Kn_g \ll 1$) limit (see, e.g., section 4). Of course, if Kn_g is not small (e.g., $O(1)$), these slip/jump effects will render ordinary continuum estimates practically useless.

In closing this section it should be commented that these "accommodation" coefficients α_{mass} , α_c , $\alpha_{m,i}$, while normalized in the sense that $\text{max } \alpha = O(1)$, are not what might be called "elementary" (step) rate constants. For one thing they represent averages over molecules which arrive from all directions and at all speeds, according to the prevailing (often non-Maxwellian) molecular velocity distribution function. Similarly, the desorbing or scattered molecules are distributed with respect to direction, velocity, and possibly internal state (see, e.g., Halpern and Roemer, 1978; Mantell et al., 1986). Finally, the "acts" of tangential momentum transfer, gas/solid energy exchange, and species mass accommodation (equilibration) are often mechanistically complex, involving a sequence of (more-or-less) elementary steps, which may include adsorption, surface migration to singular sites, and activated desorption. This implies that the coefficients α_{mass} , α_c , and $\alpha_{m,i}$ cannot be expected to be "constants" but can depend on many variables (besides the solid and gas temperatures) that determine adsorbed molecule populations and surface structure (morphology, ...). Nevertheless, there are many practical problems which can be solved at the level of information of these accommodation coefficients (see, e.g., section 4), and these coefficients are far more accessible to direct measurement than the elementary-step rate constants underlying them. One highly idealized way of "interpreting" these α values, which dates back to Maxwell's time and is computationally easy to implement, is the following: of all incident molecules,

$$C_{1,1s} = \frac{m_1}{m_1 + m_2} \gamma_1 \sigma_{\text{max},1} \sigma_{\text{max},2} \quad (3-3)$$

The Kramers-Kristenaker (1943) estimate, supported by their experiments using disparate molecular weight binary gas mixtures (H₂ + air) with $m = \gamma_1 m_1 + \gamma_2 m_2$, was

$$C_{1,1s} = \frac{(m_1/m_2) - (m_2/m_1)(m_1/m_2)^{1/2}}{\gamma_1(m_1/m_2)^{1/2} + \gamma_2} \quad (3-4)$$

(which vanishes when $m_1 = m_2$). This analysis was recently generalized by Noever (1980), who relaxed the diffuse-reflection restriction to obtain (in our notation):

$$C_{1,1s} = \left[\frac{m_2}{m_1} - \frac{m_1}{m_2} \right] - \frac{\alpha_2 - \alpha_1(m_1/m_2)^{1/2}}{\gamma_2 + \gamma_1(m_1/m_2)^{1/2}} \quad (3-5)$$

More generally, Loyalka and Cipolla (1971) had previously shown that the simple Kramers-Kristenaker expression was reasonable for $\alpha = 1$ and $m_1 \gg m_2$ but that $C_{1,1s}$ did not necessarily vanish when $m_1 = m_2$. While not explicitly discussed below, Annis and Mason (1976) have shown that this form of result can be readily used to predict the phoresis of aerosol particles in a spatially nonuniform composition gas mixture—i.e., aerosol particle diffusiophoresis, over a broad range of Knudsen numbers, $1/4 \leq Kn \leq 10$. Another interesting result is that thermophoresis and diffusiophoresis are not simply “additive”—there is a nonzero coupling term estimated by Annis and Mason (1976) using the “dusty gas” (disparate mass) limit of Enskog-Chapman theory.

3.2. Molecular-Level Numerical Simulation Methods. As we have seen, the discontinuities associated with diffusion fluxes either across or parallel to solid surfaces in gaseous systems arise from the existence of Knudsen sublayers within which the continuum approximation fails since the length scale characterizing these layers is the local mean-free path. However, as one moves sufficiently far from the boundary (i.e., several mean-free paths away), the continuum approximation becomes valid, so that fluid flow can usually be described by the well-known macroscopic differential balance equations; e.g., Navier-Stokes equations and associated total mass, heat, and species mass balance equations incorporating linear diffusion flux laws. Knudsen sublayer problems have been successfully attacked in the past using analytical/numerical techniques within the framework of the linearized Boltzmann equation for the one-particle distribution function. Unfortunately, mathematical complexities call for drastic simplifications for progress to be made. Typically, approximations involve linearization of governing equation(s) and boundary conditions, one-dimensional geometry, and model kinetic equations (e.g., the BGK linearized collision-operator model). The latter limitation has been removed in more recent numerical implementations of such schemes (see, e.g., Loyalka, 1989). Nevertheless, very useful results have been obtained which, apart from serving their primary purpose, can be invoked as limiting-case benchmarks in validating more general schemes. With the advent of high-speed scientific computing, attractive alternatives have indeed emerged—i.e., particle-level simulation methods.

Microscopic simulations of dilute gases have chiefly been pursued by employing direct simulation Monte Carlo methods, hereafter abbreviated DSMC (Bird, 1994). In DSMC, the governing Boltzmann equation is attacked by combining a deterministic treatment of the

streaming part of the equation with a probabilistic evaluation of the more complicated (nonlinear) integral collision term. In these simulations, a collection of “particles” is distributed within the chosen computational domain, each particle corresponding to a large number of actual fluid molecules. Subsequently, particles are allowed to interact according to prescribed rules. Quantities of interest, such as mass-average velocity, temperature, etc., are calculated by locally averaging the collected statistics. Clearly then, information on the microscopic as well as the macroscopic scale is obtained. Advantages of this method include CPU time linearity related to the total number of computational particles (and this allows total particle numbers in the range between 10^6 and 10^8 , depending on the resources available) and computational domains with macroscopic dimensions, a prerequisite for practical applications. Although the original formalism is limited to dilute gases where gas molecules have finite cross section but occupy negligible volume, newly developed algorithms allow for a generalization of the DSMC algorithm to account for higher density effects, in particular the excluded-volume effects of the Enskog theory of dense gases (see Alexander *et al.*, 1995). DSMC techniques have proven to be quite successful in elucidating the phenomena of slip, jump, and creep in rarefied gases (Bird, 1976; Morris *et al.*, 1992; Wadsworth, 1993; Papadopoulos, 1996; Papadopoulos and Rosner, 1996). Studies in this research area were initiated by Bird (1976), who considered the classical incompressible Kramers problem (the rarefied counterpart of the Rayleigh impulsive flat plate motion in a viscous fluid). The main objective of his study was to compute the velocity slip and velocity “defect” from the linear profile when a macroscopically linear velocity profile is imposed in the vicinity of a solid wall. Although statistical scatter was considerable as a result of their limited computational power and relatively low Mach numbers, his results compared well with existing analytical results. The problem has been extensively revisited since that time to address more subtle questions (Morris *et al.*, 1992).

The temperature jump problem has also received attention because of its relevance in experimental measurements of heat transfer using small diameter probes (hot-wire anemometry, thermocouples). In Figure 3 we present a typical computed temperature profile for a planar, one-dimensional geometry. Notice that the profile is nearly linear sufficiently far from the walls, but suffers discontinuities in the vicinity of the walls, the magnitudes of which are a function of the local mean-free path (note that on the “hot” side the jump is slightly more pronounced) and bulk temperature gradient. The completely analogous phenomenon of composition jump has been detected in simulations of gas mixtures by Bird (1994) and Papadopoulos and Rosner (1996).

The interesting phenomena related to diffusion fluxes parallel to the bounding surface, namely, thermal and concentration creep, had not been simulated until recently, one of the reasons being that the Mach number of these creeping flows is very small and, as a result, resolution requirements become quite stringent. In the case of concentration creep there are also implementation difficulties related to establishing a steady-state concentration gradient in a certain direction. Our work (see Papadopoulos, 1996; Papadopoulos and Rosner, 1996, 1996) regarding the effects of thermal creep in enclosure flows often encountered in crystal growth

applications is reviewed in section 4.4. Here we merely mention that such simulations can successfully model two-dimensional geometries of macroscopic dimensions with arbitrary collision dynamics and appreciable gradients irrespective of the flow Knudsen number (although, obviously, the true continuum limit ($Kn \ll 1$) is neither interesting nor computationally attractive).

The second of the two major categories of particle simulations, called *molecular dynamics* (MD), is a deterministic scheme in which the equations of motion governing classical particles are numerically integrated in time. Domain dimensions and integration time steps are inherently limited by the prevailing molecular dimensions and collision times, respectively. The established procedure is to invoke similarity arguments to extract macroscopic behavior from such microscopic simulations. Both liquids and fluid densities corresponding to dense gases can be simulated, but potential pitfalls exist in the simulation of dilute gases where excluded-volume effects are negligible (Bird, 1987). The important question of when the “no-slip” condition is justifiable for dense fluid systems has received well-deserved attention from the MD community. MD simulations of Couette and Poiseuille liquid flows by Koplik *et al.* (1989) have demonstrated that the no-slip condition is established as a consequence of solid surface roughness on the molecular scale. However, at lower fluid densities they reported velocity slip associated with velocity gradients normal to the bounding walls. This slip was also found to be independent of the particular type of flow and well-predicted using analyses based on slip-length arguments. Interestingly enough, the authors proposed that previous theoretical difficulties regarding moving contact lines between two immiscible fluids can be remedied by relaxing the no-slip condition in the seemingly singular region. Related studies by Mo and Rosenberger (1990) on the effect of various roughness models on slip conditions suggested the relevance of a Knudsen number based on mean roughness height. Because MD has proven to be a valuable tool in exploring the supercritical fluid regime under equilibrium and near-equilibrium conditions (see, e.g., Kincaid *et al.*, 1992), very likely it can be used to investigate jump and creep phenomena in dense fluid systems near solid boundaries. This task has evidently not been undertaken to date, perhaps because of the above-mentioned difficulties related to velocity-scale resolution and thermal noise.

4. Applications and Implications

Some important examples in which slip, jump, and creep phenomena influence macroscopic transport rates even in the near-continuum limit ($Kn \ll 1$) are indicated below.

4.1. Drag and “Stopping Time” of a Suspended Solid Spherical Particle. For $Re \ll 1$ near-continuum flow about a solid sphere, Bassett (1988) derived a result equivalent to:

$$C_D = (C_D)_{\text{Stokes}}/C_{\text{slip}} \quad (4-1)$$

where $(C_D)_{\text{Stokes}} = 24/Re$ is the well-known Stokesian (no-slip) drag coefficient, and C_{slip} is the corresponding correction factor (> 1) for nonzero slip:

$$C_{\text{slip}} = \frac{1 + 12 \left[\left(1 - \frac{1}{2} \sigma_{\text{max}}\right) \sigma_{\text{max}} \right] Kn_a}{1 + 8 \left[\left(1 - \frac{1}{2} \sigma_{\text{max}}\right) \sigma_{\text{max}} \right] Kn_a} \quad (4-2)$$

Expanding this for small Kn_a gives

$$C_{\text{slip}} \approx 1 + 4 \left[\left(1 - \frac{1}{2} \sigma_{\text{max}}\right) \sigma_{\text{max}} \right] Kn_a + h.o.t. \quad (4-3)$$

Comparison of this result with the functional form of $C_{\text{slip}}(Kn_a)$ recommended by Millikan (1923) for the entire Kn_a range, viz.:

$$C_{\text{slip}} = 1 + 2Kn_a[A_1 + A_2 \exp(-A_3/Kn_a)] \quad (4-4)$$

shows that:

$$A_1 \approx 2 \left[\left(1 - \frac{1}{2} \sigma_{\text{max}}\right) \sigma_{\text{max}} \right] \quad (4-5)$$

i.e., A_1 is σ_{max} -sensitive, not (necessarily) the constant 1.26 cited in the literature based on Millikan’s careful oil drop experiments. Clearly, then, the all-important *particle stopping (relaxation) time*, t_p (Friedlander, 1977; Fernandez de la Mora and Rosner, 1981, 1982; Rosner, 1986; Konstantopoulos and Rosner, 1995), is given by:

$$t_p = 1/\rho_p d_p^2 (18\mu) / [C_{\text{slip}}(Kn_p) \sigma_{\text{max}}] \quad (4-6)$$

where the dependence on σ_{max} is now highlighted. Note that this will affect the familiar “sedimentation” velocity, U_p , as well as the Brownian diffusion coefficient, D_p , which, according to Einstein, can be expressed as

$$D_p = (k_B T/m_p) \lambda_p \quad (4-7)$$

Even for, say, $Kn_a = 1/50$, with TMAC = 0.86 (the He-(g)/Pt(s) system) t_p and D_p are increased by 26% over the Stokesian values.

As a historical note, we remark that the first major engineering applications of “slip-induced drag reduction” arose in the fields of “vacuum” flow system design (now of even greater importance to chemical, mechanical, and electrical engineers because of the solid-state microelectronic industry) and “high”-altitude aerodynamics (Nien, 1948), both subsonic and supersonic. These activities spawned the *Rarefied Gas Dynamics Symposia*, 19 of which proceedings are available covering the period 1958 to the present.

4.2. Reduced Heat Transfer in “Light Gas/Heavy Solid” Systems. In 1956, Kavanagh experimentally verified the success of the Nu_d -correlation form given by eq 2–24, where Nu_d is the Nusselt number based on $T_w - T_\infty$ and sphere diameter d , and the dimensionless “constant” $2(1 - (1/2)\sigma_{\text{max}})\sigma_{\text{max}}$ was determined by matching the available experimental data (see, e.g., Schauf and Chambré, 1968). The approach of Fuchs and Sutugin (1970), which considers the KSL to be a thermal resistance in series with the continuum “outer” gas layer, as expected, leads to the same result as eq 2–24 in the small Kn_a limit. Using the general σ_{max} -dependent Nu_d value leads to startling conclusions; e.g., for a system like He(g)/W(s) with $\sigma_{\text{max}} \approx 0.005$, $\gamma = 1/4$, $Pr = 1/2$, even at $Kn_a = 1/50$ the heat-transfer coefficient Nu_d will be reduced by a factor of about $1/4$ (see, also, Alghara *et al.*, 1987). For example, on this same basis we expect that many “radiation-corrected” thermocouple temperature measurements in combustion gases (often made using alloys of Pt and/or Ir) are systematically too low because of failure of the investigators to take into account this important “temperature jump” phenomenon.

4.3. Suspended Particle Thermophoresis in Gases. Even allowing for slip associated with low Kn_a , the Brownian diffusivity (eq 4–7) of suspended aerosol

particles is much smaller than the host gas momentum diffusivity. This causes *isothermal* aerosol convective-diffusion problems to be excellent examples of high Schmidt number mass transfer (see, e.g., Friedlander, 1977; Fernandez de la Mora and Rosner, 1981, 1982), with the Brownian diffusion boundary layer embedded well within the momentum (or vorticity) boundary layer. As a consequence, convective-diffusion particle capture efficiencies, or mass-transfer Stanton numbers (Rosner, 1986), are quite small, often below 10^{-3} for particles in the super-100-nm diameter range. However, it is now known that simultaneous heat transfer (e.g., particle collection by a solid target colder than the "dusty" mainstream) dramatically alters this situation because of the efficient collection mechanism of *particle thermophoresis*. For example, one industrially significant application is the collection of doped glass microdroplets in the fabrication of optical waveguide glass fibers (Walker et al., 1979; Rosner and Park, 1989).

If one formally writes the local thermophoretic particle drift velocity in the form:

$$V_p = (\alpha_T D_p) X \cdot (-\text{grad } T) / T_p^2 \quad (4-8)$$

where D_p is the corresponding particle Brownian diffusion coefficient (4-7), then our attention is properly focused on the *dimensionless thermophoretic diffusion factor* (α_T). Because of the thermal creep velocity induced at the surface of the nonisothermal solid sphere, it is "propelled" through the gas, moving from hot to cold. With this picture Epstein (1929) estimated that in the near-continuum limit:¹⁰

$$(\alpha_T)_p \approx C_1 [1 + (1/2)(\lambda_p/k_p)]^{-1} (Sc_p) \quad (4-9)$$

where the dimensionless creep coefficient C_1 ($\alpha_{\text{continuum}}$ intermolecular force law) is defined above. This means that when Sc_p increases, so does $(\alpha_T)_p$, with the interesting result that the relevant product $\alpha_T D_p$ appearing in eq 4-8 remains a size-independent constant. Accordingly, despite the smallness of D_p for particles above about 100 nm diameter, the product $\alpha_T D_p$ remains proportional to λ_p albeit with the factor $C_1 [1 + (1/2)(\lambda_p/k_p)]^{-1}$, which will inevitably be smaller for highly conducting particles (silver, diamond, ...) than thermal "insulators". Mackowski (1990) has applied this method to predict the phoretic motion of two touching spheres, including unsymmetrical combinations at arbitrary orientations with respect to $-\text{grad } T_p$, as well as quasi-spherical particle clusters simulating soot aggregates (Rosner et al., 1991). From these and related studies it appears that the orientation-averaged $\alpha_T D_p$, written $(\alpha_T D_p)_0$, is remarkably insensitive to aggregate size and morphology—a result also obtained for swarms of colloidal particles in electrophoretic applications (Acroff et al., 1990). Moreover, this result provides the theoretical basis for the widely used method of "thermophoretic (soot) sampling" (Dobbins and Megaridis, 1987; Koylu et al., 1996; King et al., 1996a,b). Such sampling is "gentle" enough, relatively unbiased with respect to aggregate size, morphology, and orientation, and associated with adequate capture efficiencies.

In summary, we see that, in all of these cases, the thermal creep velocity associated with tangential temperature gradients is "responsible" for the efficient collection of aerosol particles (by colder solid targets) which would be difficult to collect by the methods of (a) isothermal convective-diffusion (D_p , too small), or inertia (λ_p , too small), as we have also experimentally (and theoretically) studied situations in which *thermophore-*

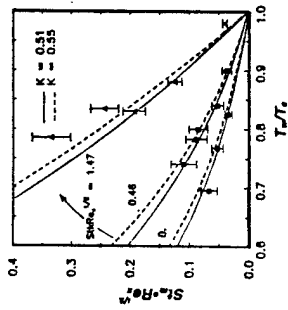


Figure 3. Dimensionless mass-transfer rate parameter $St_p Re_p^{1/2}$ vs T_p/T_w for forced flow past a cold concave surface (simulating a combustion turbine blade). Predictions displayed are for the best values of the dimensionless property $St_p Re_p^{1/2}$ for the ca. 0.85 μm diameter particles used. Maximum value (0.658) occurs at the Waldmann free-molecule limit using $\alpha_{\text{continuum}} = 1$ (after Konstantopoulos and Rosner, 1988).

sis and inertia "cooperate" to increase cooled wall deposition rates (Konstantopoulos and Rosner, 1995). Figure 2 shows our results for the dimensionless particle mass-transfer rate parameter $St_p Re_p^{1/2}$ as a function of both T_p/T_w and the relevant particle inertia parameter $St_p Re_p^{1/2}$ for forced flow past a "cold" concave surface (simulating apart from turbulence) the pressure side of a combustion turbine blade). Predictions displayed are for estimated values of the dimensionless property parameter $(\alpha_T D_p)_0$ for the ca. 0.85 μm diameter particles used, with the maximum value corresponding to the Waldmann free-molecule limit: $(34)(1 + (\lambda_p/k_p))^{-1}$ evaluated using $\alpha_{\text{continuum}} = 1$. For larger, suspended particles than those used (ca. 0.84 μm) in these experiments, carried out at T_p values near 1500 K, the thermophoretically dominated $St_p Re_p^{1/2}$ values would be smaller (due to the reduction in $(\alpha_T)_p$) for a given T_p/T_w , but the inertia enhancement (concave surface) would be greater (via $St_p Re_p^{1/2}$) than those shown in Figure 2. In some applications, "overheated" surfaces can be used to reduce mass-transfer rates *vis* the equivalent of "thermophoretic blowing" (see, e.g., Cokoglu and Rosner, 1984, 1986; Park and Rosner, 1989).

Since this type of phoresis depends on a nonuniform gas temperature adjacent to the surface, other methods of inducing this (e.g., nonuniform absorption of electromagnetic radiation within the particle) will also produce particle phoresis. For a recent account of the theory of particle photophoresis, including the near-continuum limit ($Kn_p \ll 1$), see Mackowski, 1989, and the summary in Rosner et al., 1992. For engineering consequences (increased soot deposition rates) in environments with high radiation energy fluxes and absorbing particles, see Carrillo et al., 1990. For an interesting situation in which thermophoresis affects even the population dynamics of "radiation-cooled" coagulating soot particles, see Mackowski et al., 1994.

Before concluding this brief discussion of "small" particle thermophoresis, we should briefly consider the limit of particles that are really "heavy molecules" (polymers in "solution"). In this limit the coefficient $(\alpha_T)_p$ may be interpreted as the conventional *Ludwig-Soret coefficient* for molecular thermal diffusion (Rosner, 1980), and a purely hydrodynamic/macroscopic approach to its prediction inevitably becomes problematic (as in the case of applying the Einstein-

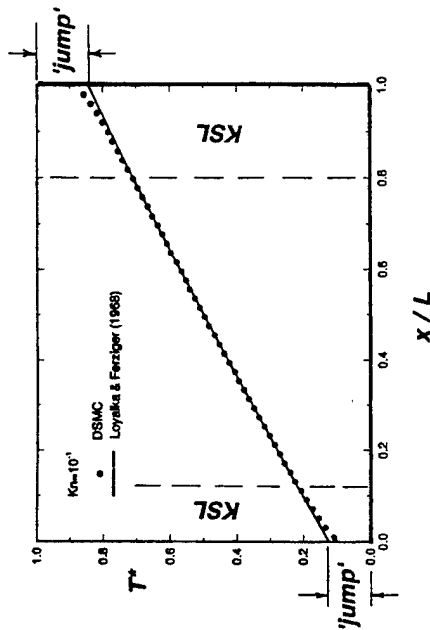


Figure 4. Dimensionless temperature vs distance plot for a stratified gas contained within a one-dimensional gap. The cold wall at $x/L = 0$ is kept at the relative dimensionless temperature zero and the hot wall at $x/L = 1$ at unit temperature. The nominal Knudsen number is 10^{-3} . Solid circles represent computational results, whereas the line gives the prediction based on linearized Boltzmann equation theory proposed by Loyalka and Ferriger (1968). The broken lines give an estimate of the local mean-free path (after Papadopoulos, 1996).

Stokes equation for Brownian diffusion to molecular solutes in viscous solvents). In the case at hand, apart from the proper interpretation of the "particle" thermal conductivity, k_p (eq 4-9), one must account for the appreciable Brownian motion of the "target" particle (Garcia-Ybarra and Rosner, 1989). Alternatively, from the perspective of Enskog-Chapman gas kinetic theory, the "heavy" species should predominantly be engaged in sequential binary collisions. A conceptually and practically interesting "hybrid" case in this class would be the thermal diffusion factor, α_T , for the highly symmetrical "Buckyball" C₆₀ molecule (now called fullerene) in combustion gases above atmospheric pressure. Each such carbon "nanoparticle" weighs only 1.2×10^{-21} g and has a diameter of only ca. 0.71 nm.

We should also note (see, also, section 6) that there appear to be few experimental measurements of $(\alpha_T)_p$ (or C_1) for submicron particles suspended in dense vapors or true liquids (McNab and Meisen, 1973; Shundu et al., 1995). Inferred $(\alpha_T)_p$ values in liquids appear to be of order unity (calculated using the thermal fractionation data of Shundu et al., (1996)), making the phenomenon of particle thermophoretic mass transport in liquids unlikely to be of major engineering importance (see, e.g., Rosner et al., 1992). However, the situation is less clear for nonisothermal supercritical fluids (e.g., "thermally stressed" jet aircraft fuels) of current technological importance. In either case, from a theoretical viewpoint such measurements would be quite valuable, especially if the particles had well-characterized surfaces, and competing phenomena (sedimentation, ...) could be suppressed (see section 5).

4.4. Wall-Driven Convective Flows in Nonisothermal Crystal Growth Annuales. Rosner (1989) pointed out for the first time that gas-filled nonisothermal ampoules operating in microgravity for purposes of crystal growth will experience appreciable convection driven by "wall-induced thermal creep" (as well as, perhaps, nonnegligible thermal stresses in the bulk gas). Using Maxwell's original estimate (eq 3-1), Rosner concluded that the thermal creep velocity under typical

ampule conditions was comparable to the characteristic diffusion velocity of the pseudo-binary mixture. His estimates showed that even for "Earth-bound" experiments ($g = 9.8 \text{ m/s}^2$) thermal creep-induced flow can cause a nonnegligible effect when compared to buoyancy-induced convection. The fact that the presence of the nonisothermal side walls induces a flow from cold-to-hot implies that, by virtue of total mass conservation, a flow of comparable magnitude will be induced in the opposite direction in the enclosure core region. Consequently, with the help of the end walls, the fluid is forced into a circulatory motion with two counterrotating vortices.

These qualitative and semiquantitative predictions were corroborated in a recent paper by Papadopoulos and Rosner, 1995. The authors used a direct simulation Monte Carlo technique (see section 3.3) to compute the gas flow due to side-wall thermal creep in a Cartesian, two-dimensional geometry charged with a monatomic, ideal gas. A temperature gradient predominantly in the direction parallel to the enclosure side walls was imposed on the microscopic level by assigning the velocities of molecules after collision with the solid wall from a local nondrifting Maxwellian, the temperature of which varied linearly between the values assigned at the end walls. The particular implementation followed an algorithm proposed by Stefanov and Cervigni (1998) for a hard-sphere gas but is readily modified to account for other, more realistic, molecular interaction potentials (see Bird, 1994). One of the most appealing features of this approach is that its validity is not limited to any specific range of Knudsen numbers, since it is based on the Boltzmann equation. We emphasize that in these simulations thermal creep and temperature jump are directly determined by the microscopic formulations.

In Figure 4 we show a vector velocity field for the specific choice of parameters indicated in the figure caption. Indeed, our DSMC simulation successfully captures the vortical structures referred to above. Since

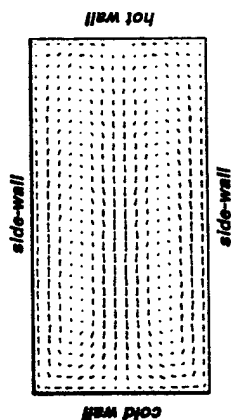


Figure 4. Flow field caused by thermal creep in an annulus of aspect ratio of 2. Relevant parameters are $Er = 16(\Delta T/T) = 6.6 \times 10^{-4}$, $T_1 = 600$ K, and $\Delta T/T = 0.66$. Symmetry of the geometry and imposed boundary conditions allow for a reduction of computational cost by a factor of 2. Two vortices are established, which are mirror images of each other (after Papadopoulos and Roemer, 1996).

the calculation is for a two-dimensional enclosure, the vortices are essentially rolls that extend in the third direction, with the vorticity vector changing direction across the symmetry plane $y = 1/2$. It is quite remarkable that without assigning a slip velocity explicitly or implicitly at the boundary and in the complete absence of body forces, convective motion arises merely as a consequence of interactions between molecules and the nonisothermal solid boundaries and between molecules and other molecules, confirming the expectations of Roemer (1988).¹⁶ Put another way, despite the small Knudsen numbers typically associated with these flows (0.10^{-3}), one cannot apply no-slip boundary conditions along the nonisothermal annular walls—*i.e.*, the walls drive a significant amount of convection. Incidentally, the appreciable statistical scatter appearing in Figure 4 is directly related to the very low Mach numbers characterizing creeping flow problems. As a result, adequate resolution of small-velocity scales requires an increased amount of statistics, which inevitably leads to longer computational execution times. For these reasons, one of the ultimate objectives in performing microscopic simulations is to guide the development of efficient, and accurate, continuum computational schemes (e.g., Mackowski *et al.*, 1998; Viviani and Savino, 1993) based on the more detailed information now becoming available, rather than using DSMC as a routine predictive tool. However, for some applications in which the relevant local Knudsen number is $O(1)$, as in submicroscopic pressure CVD reactors, DSMC-type simulations may be "inescapable" (see e.g., Cornwell and Jensen, 1998; Barrioli, 1996).

Recently, the authors extended this technique to compute internal flows induced by the analogous phenomenon of concentration creep (Papadopoulos and Roemer, 1996). The DSMC procedure developed allows for the simulation of both equal and disparate mass gas mixtures. Reported results reveal significant confinement effects for a range of Er values, which cannot be accounted for by macroscopic calculations incorporating a one-dimensional kinetic boundary layer theory.

5. Generalizations and Conclusions

We have emphasized here perhaps the simplest (and best understood) fluid/solid interface, *viz.*, the ideal gas/smooth crystalline solid interface. Not only is this limiting case easiest to understand and therefore instructive but the dynamical, thermal, and chemical nonequilibrium effects of concern to us are actually of

engineering importance, as the examples of section 4 demonstrate. Moreover, reasonably direct measurements of the relevant accommodation coefficients can be made using molecular beam/surface science techniques (see e.g., Fenn *et al.*, 1967). However, before turning to dense vapor and true liquid/solid interfaces, it would be misleading to imply that important questions do not remain concerning momentum, energy, and mass exchanges at nonequilibrium gas/solid interfaces. In this connection, mention should be made of the ubiquitous complexities of dealing with polyatomic gas mixtures, surfaces which are either partially covered by adsorbed molecules from the vapor phase or rough on many scales (up to and including l_p), and very high driving forces (values of the product $K_n(\Delta T/T)$ which do not satisfy the inequality $Er(\Delta T/T) \ll 1$).

For reasons similar to those underlying large "dense vapor" corrections to the ideal gas Newtonian viscosity, Fourier thermal conductivity, and Fick diffusivity, we anticipate large but systematic departures from the above-mentioned slip, jump, and creep results (section 3) as one considers nonequilibrium dense vapor/solid and, ultimately, liquid/solid interfaces. While no rational theoretical formalism (akin to the binary-solution Boltzmann equation) is available, theoretical progress in this area will probably come principally via the route of relevant molecular dynamics "computer experiments" focused on the fluid/solid interfacial region (see, e.g., Koplik *et al.*, 1989; Mo and Rosenberger, 1990). Very likely, the most demanding calculations will pertain to the most subtle effects, so that from an engineering viewpoint, when l_p , n , σ , and σ become comparable, slip, jump, and creep effects will be small enough that their neglect will (usually) be an acceptable approximation (cf. our examples in section 4).

Regarding physical experiments as pointed out in our review of the thermally-induced porridge phenomenon (section 4.3), these "thermal creep" boundary condition phenomena determine the readily observed migration rates of suspended small solid particles. This leads to the idea that careful porosity measurements in a suitably designed microgravity environment (to preclude complications, such as "sedimentation" for particles large enough both to sustain large-temperature differences and to avoid appreciable Brownian motion) could be used to obtain unambiguous information about the nature of the tangential momentum transfer boundary condition over a broad range of Newtonian fluid densities. This would be especially interesting since present theoretical methods are really valid only in the low-density (ideal) gas limit. To clarify the nature of the BC transition from the Enskog–Chapman regime to the technologically important but theoretically less tractable case of liquid-like densities (including supercritical polyatomic vapors), it is inevitable that high-quality experimental data for carefully selected fluid/solid interfaces will be required. The best environment for obtaining these data, since one can escape buoyancy and sedimentation phenomena, may indeed be the "microgravity" environment.

Of course, there are many other types of sharp transitions that can be fruitfully considered to be "interfacial" separating adjacent continua, other than the fluid/solid (phase) boundaries examined here (Roemer, 1976, 1986; Brenner and Leal, 1982). Extrapolating from the specific but instructive examples we have selected here, it can be said that if the transport properties of any kind of "interfacial region" were known, analogous jump expressions could be derived, as well as the necessary conditions for the neglect of such jumps. Thus, the general situation is seen to be

similar to heat conduction across a composite material. If there is an (unseen) thermal resistance between two adjacent conductors, it will appear that the temperature is discontinuous in going from one conductor to the next. Moreover, the magnitude of this "jump" will increase with the magnitude of the energy flux through the interface. Similarly, when there is species mass transport across any interface (as in the selective dissolution of gases into metals (e.g., Roemer *et al.*, 1976) or the sublimation of a multicomponent solid), there must be an associated jump in chemical potential, etc. Indeed, gaining a quantitative understanding of the nature of interfacial resistances to transport is an important goal of the science of interfacial chemistry. Fortunately, in many cases of engineering importance it can be assumed that the "interfacial resistances" are negligible, especially compared to other resistances in series with the interface. Then, and only then, phase equilibrium relationships can be invoked as a locally valid approximation, even in the presence of a net transfer rate. However, as emphasized by our present selection of gas/solid examples (section 4), it is more prudent for the engineer/scientist to view continuity of the relevant field variables across an interface (e.g., tangential velocity, temperature, chemical potential(s)) as a potentially useful approximation rather than a rule comparable in stature to a conservation principle. This viewpoint was expressed well by Standart (1968), perhaps appropriate for concluding this paper: "Only accept continuity of a variable when we can prove it to exist".

Acknowledgment

It is an honor and a pleasure to be included in this birthday celebration of Eli Ruckenstein's extensive contributions to the fields of physical chemistry and chemical engineering science and to acknowledge Prof. Ruckenstein's occasional but timely guidance (to D.E.R.) over a ca. 30 year period. Eli's career-long fascination with (a) interfacial phenomena, (b) simultaneous methods which establish quantitative relationships between complex convective–diffusion situations and their simpler (limiting-case) counterparts, (c) the exploitation of rational asymptotic approximations (especially $Sc \gg 1$), and (d) non-Brownian mechanisms of suspended particle transport either have proven to be extremely contagious or are remarkably shared by at least one of us (D.E.R.). This particular contribution places our recent research at the Yale University Chemical Engineering Department High Temperature Chemical Reaction Engineering Laboratory (especially in the areas of particle thermophoresis across combustion gas boundary layers and wall creep-driven flows in microgravity crystal growth) into the broader historical and pedagogical context of jump, slip, and creep effects at fluid/solid interfaces, including not only ideal gas mixtures but also dense vapors and electrolyte solutions. We are indebted to our sponsor AFOSR (Grant No. 94-1-0143), NASA-MSAD (Grant No. NAG 3-1664), and the HYCRE Lab (Industrial Affiliates: ALCOA, DuPont, Union Carbide, Praxair, Shell, SCM-Chemicals, General Electric, Babcock and Wilcox) for helping to make this fundamental research, and its publication, possible. D.E.R. would also like to acknowledge the contributions of all of his co-authors (section 6), Yale faculty colleagues (J. B. Fenn, A. Gomez, and J. Fernandez de la Mora), and former students in helping to shape many of the ideas summarized here. In some sense, this paper can be considered an intellectual "sequel" to his paper *Chem. Eng. Educ.* (AIChE, CHE Div.) 1976, X (4), 190–194 on

Nomenclature

- $A(i=1,2,3)$ = coefficients in C_{30} expression, eq 4-4
 z = mean molecular thermal speed
 C_p = molar heat capacity
 C_f = specific heat
 C_f = skin friction coefficient (dimensionless), e.g., Roemer, 1986
 C_D = drag coefficient (dimensionless)
 C_r = thermal creep coefficient
 C_{30} = slip correction factor, eq 4-1
 C_{30} = concentration creep coefficient, eq 3-2
 C_{30} = fullerene (carbon)
 D_{12} = binary diffusion coefficient
 d_p = particle diameter
 G = net mass flux through interface
 h_s = specific enthalpy
 h_s = stagnation enthalpy, e.g., Roemer, 1986
 J = species mass diffusion flux vector
 k_B = Boltzmann constant
 k_p = gas thermal conductivity
 k_p = particle thermal conductivity
 K = $(\sigma_p D)/\nu$, Figure 2
 K_n = Knudsen number, l_p/L or l_p/δ
 l_p = gas mean-free path
 L = macroscopic length scale
 M = molecular weight
 n_i = species i molecular mass
 N_A = Avogadro number
 Nu = Nusselt number, e.g., Roemer, 1986
 n = number density
 P_r = Prandtl number (momentum/energy diffusivity ratio)
 p = pressure
 q'' = energy diffusion flux vector
 q'' = Reynolds number, $U l_p/\nu$
 R = universal gas constant
 Sc = Schmidt number, ν/D_1
 St = Stanton number, e.g., Roemer, 1986
 StH = particle Stokes number, $\nu/(LU)$
 T = absolute temperature
 T_p = dimensionless temperature, Figure 3
 t_p = particle stopping time; eq 4-6
 U = mainstream gas velocity
 v = gas velocity
 x = distance measured along the wall
 y = distance measured normal to the wall
 Y = species i mole fraction
 Y = dimensionless distance in the vertical direction
 Z^* = molecular flux
Greek Symbols
 α = accommodation coefficient
 α_T = thermal diffusion factor
 δ = boundary layer thickness; Figure 1
 μ = dynamic viscosity
 ν = momentum diffusivity, μ/ρ
 ρ = mass density of mixture
 σ = molecular diameter
 τ = local shear stress
 ω = species mass fraction
Subscripts and Superscripts
 e = pertaining to the outer edge of the viscous boundary layer; Figure 1
 E, G = pertaining to the gas

- h = pertaining to heat transfer
 i = species index
 m = pertaining to mass transfer
 mom = pertaining to momentum transfer
 p = pertaining to the particle
 t = tangential component
 y = normal component (of vector)
 y = pertaining to the surface y = const.
 (o) = evaluated in the $Kx - 0$ (continuum) limit
 (+) = evaluated on the positive side of $y = 0$
- Abbreviations, Acronyms, and Operators**
 AC = accommodation coefficient
 A = pertaining to species A in a gas mixture
 BC = boundary condition
 BKG = Bhatnagar-Gross-Krook
 BL = boundary layer
 CVD = chemical vapor deposition
 CPU = central processing unit
 DSMC = direct simulation Monte Carlo
 EAC = energy accommodation coefficient, on grad = spatial gradient operator
 fm = free molecule ($Kx \gg 1$)
 G/S = gas/solid (interface)
 h.o.t. = higher order terms
 KSL = Knudsen sublayer (Figure 1)
 LTCE = local thermochemical equilibrium
 LBL = laminar boundary layer
 MAC = mass accommodation coefficient, on max() = maximum value operator
 MC = Monte Carlo
 MD = molecular dynamics
 OD = order-of-magnitude
 TMAC = tangential momentum accommodation coefficient,
- Equations**
 [] = "jump operator", i.e., $[T] = T(0^+) - T_0$
 { } = argument of a function

Literature Cited

- Acivros, A.; Jeffrey, D. J.; Saville, D. A. Particle Migration in Suspensions by Thermocapillary or Electroosmotic Motion. *J. Fluid Mech.* 1990, 213, 85-110.
- Albers, Y.; Kasey, D.; Libby, P. A. Heat Transfer From Circular Cylinders at Low Reynolds Numbers. II. Experimental Results and Comparisons With Theory. *Phys. Fluids* 1967, 10(6), 947-952.
- Alexander, F. J.; Garcia, A. L.; Alder, B. J. A Consistent Boltzmann Algorithm. *J. Colloid Interface Sci.* 1996, 26, 6212-6216.
- Anderson, J. Colloid Transport by Interfacial Forces. *Annu. Rev. Fluid Mech.* 1990, 22, 61-81.
- Annis, B. K.; Mason, E. A. Theory of Thermofluorophoresis of Spherical Aerosol Particles. *Chem. Soc. Trans.* 1976, 6, 106-117. See also: Annis, B. K. *J. Chem. Phys.* 1974, 57(7).
- Bartell, T. J. Low Density Gas Modeling in the Micro-electronics Industry. In *Rarefied Gas Dynamics*; Proceedings of the 19th International Symposium, Oxford, July 1994; Harvey, J., Lord, G., Eds.; Oxford University Press: Oxford, U.K., 1995; pp 611-620.
- Beesony, S.; Chernyuk, V. Thermophoresis of a Spherical Particle in a Rarefied Gas: Numerical Analysis Based on the Model Kinetic Equations. *Phys. Fluids* 1996, 7(7), 1713-1766.
- Bird, G. A. Direct Simulation of the Incompressible Kraemer Problem. *Proc. Simulation of Turbulence*, 1976, 51, 323-333.
- Bird, G. A. Direct Simulation of High Velocity Gas Flows. *Phys. Fluids* 1987, 30, 364-366.
- Bird, G. A. *Molecular Gas Dynamics and the Direct Simulation of Gas Flows*; Clarendon Press: Oxford, U.K., 1994.
- Brown, H.; Lee, L. O. Conservation and Constitutive Equations for Adhesive Shear-Induced Surface Diffusion and Convection in a Fluid-Fluid Interface. *J. Colloid Interface Sci.* 1982, 89(1), 136-154.
- Brock, J. R. On the Theory of Thermal Forces Acting on Aerosol Particles. *J. Colloid Sci.* 1962, 17, 765-780.
- Brush, S. G.; Everitt, C. W. Maxwell, Osborne Reynolds and the Radiometer. *Historical Studies in the Physical Sciences*; University Pennsylvania Press: Philadelphia, PA, 1969; Vol. 1, pp 116-132.
- Caldwell, R. D. Field-Flow Fractionation. *Anal. Chem.* 1988, 60(11), 969-971A.
- Castillo, J. L.; Mackowski, D. W.; Roemer, D. E. Thermophoretic Contribution to the Transport of Absorbing Particles Across Combustion Gas Boundary Layers. *Prog. Energy Combust. Sci.* 1980, 16, 263-280.
- Castillo, J. L.; Garcia-Ybarra, P. G.; Roemer, D. E. Morphological Instability of a Thermophoretically Growing Deposit. *J. Cryst. Growth* 1991, 116, 105-126.
- Cornwell, D. J.; Jensen, K. F. Models of Rarefied CVD Processes at Reduced Pressures and Reduced Dimensions. *Proc. CVD XII*, Electrochem. Soc. 1983, 92(2), 87-83. Cf. also: *J. Electrochem. Soc.* 199(6), 2264-2273.
- Davis, E. J. Micro-Chemical Engineering: The Physics and Chemistry of the Microparticle. *Advances in Chemical Engineering*; Academic Press: New York, 1992; Vol. 16, pp 1-94.
- Davis, R. W.; Moore, E. F.; Zachariah, M. R. *J. Cryst. Growth* 1983, 132, 813. See also: Davis, R. W.; Burns, T. J. Numerical Modeling of Particle Transport in Rotating Disk and Barrel-Type CVD Reactors. AIChE 1986 Meeting; Paper 168e.
- Dobinin, R. A.; Megaritis, D. Morphology of Flame-Generated Soot as Determined by Thermophoretic Sampling. *Langmuir* 1997, 3, 254-259.
- Edwards, D.; Denny, V.; Mills, A. Transfer Processes—An Introduction to Diffusion, Convection and Radiation, 2nd ed.; Holt, Reinhart & Winston: New York, 1979.
- Edwards, D. A.; Brenner, H.; Waan, D. T. *Interfacial Transport Processes and Rheology*; Butterworth-Heinemann: Stoneham, MA, 1991.
- Epruin, P. S. Zur Theorie der Radiometer. *Z. Phys.* 1928, 54, 637-668.
- Fenn, J. B.; Anderson, J. B.; Kostoff, R. N. Measurements of Momentum Accommodation of Gas Molecules at Surfaces. In *Fundamentals of Gas-Surface Interactions*; Satake, H., et al., Eds.; Academic Press: New York, 1987.
- Fernandes de la Mora, J.; Roemer, D. E. Inertial Deposition of Particles Revisited and Extended: Eulerian Approach to a Traditionally Lagrangian Problem. *J. PhysicoChem. Hydrodyn.* 1991, 2, 1-21.
- Fernandes de la Mora, J.; Roemer, D. E. Effects of Inertia on the Diffusional Deposition of Small Particles to Spheres and Cylinders at Low Reynolds Numbers. *J. Fluid Mech.* 1982, 125, 379-395.
- Friedlander, S. K. *Smoke, Dust and Haze—Fundamentals of Aerosol Behavior*; Wiley: New York, 1977.
- Fuchs, N. A. *The Mechanics of Aerosols*; Pergamon: Oxford, U.K., 1964.
- Fuchs, N. A.; Sutugin, A. G. *Highly Dispersed Aerosols*; Ann Arbor Science Publishers: Ann Arbor, MI, 1970.
- Garcia-Ybarra, P.; Roemer, D. E. Thermophoretic Properties of Non-spherical Particles and Large Molecules. *AIChE J.* 1989, 35(1), 139-147.
- Giddings, J. C. *Unified Separation Science*; Wiley: New York, 1991.
- Gokoglu, S. A.; Roemer, D. E. Correlation of Thermophoretically Modified Small Particle Diffusional Deposition Rates in Forced Convection Systems with Variable Properties, Transpiration Cooling and/or Viscous Dissipation. *Int. J. Heat Mass Transfer* 1994, 37, 639-646.
- Gokoglu, S. A.; Roemer, D. E. Prediction and Rational Correlation of Thermophoretically Reduced Particle Mass Transfer to Hot Surfaces Across Laminar or Turbulent Forced-Convection Gas Boundary Layers. *Chem. Eng. Commun.* 1996, 44, 107-119.
- Gomes, A.; Roemer, D. E. Thermophoretic Effects on Particles in Counterflow Laminar Diffusion Flames. *Combust. Sci. Technol.* 1993, 89, 335-362.
- Goodman, F. O.; Wechtman, H. Y. *Dynamics of Gas-Surface Scattering*; Academic Press: New York, 1976.
- Halpern, B.; Roemer, D. E. Chemical Energy Accommodation at Catalyst Surfaces; Flow Reactor Studies of the Association of Nitrogen Atoms on Metals at High Temperatures. *J. Chem. Soc., Faraday Trans. 1* 1978, 74, 1893-1912.
- Kamotani, Y.; Otsuchi, S.; Pine, A. A Thermocapillary Convection Experiment in Microgravity. *J. Heat Transfer* 1996, 117, 611-618.
- Kennard, E. H. *Kinetic Theory of Gases*; McGraw-Hill: New York, 1988.
- Kiela, J.; Halpern, B. H.; Roemer, D. E. Chemical and Physical Energy Accommodation in the Metal Surface-Catalyzed Decomposition of Hydrazine Vapor. *J. Phys. Chem.* 1984, 88, 4622-4627.
- Kincaid, J. M.; Li, X.; Hsifakidis, B. Non-equilibrium Molecular Dynamics Calculation of the Thermal Diffusion Factor. *Fluid Phase Equilib.* 1992, 76, 113-121.
- Kogan, M. N. *Molecular Gas Dynamics*. *Annu. Rev. Fluid Mech.* 1978, 6, 383-404.
- Kogan, M. N. Non-Navier-Stokes Gas Dynamics and Thermal Stress Phenomena. *Proceedings of the 16th International Symposium Rarefied Gas Dynamics*; Tuebingen: Stuttgart, Germany, 1986; Vol. 1, pp 15-24.
- Konstantopoulos, A. G.; Roemer, D. E. Inertial Effects on Thermophoretic Transport of Small Particles to Walls with Streamline Curvature. *Int. J. Heat Mass Transfer* 1998, 39(12), 2305-2315 (Part 1), 2317-2327 (Part II).
- Koplik, J.; Banerji, J.; Willemssen, J. F. Molecular Dynamics of Fluid Flow at Solid Surfaces. *Phys. Fluids A* 1989, 1, 761-784.
- Koylu, U. O.; King, Y.; Roemer, D. E. Fractal Morphology Analysis of Combustion-Generated Aggregates Using Angular Light Scattering and Electron Microscopy Images. *Langmuir* 1993, 11, 4848-4854. See also: King, Y.; Koylu, U. O.; Roemer, D. E. *Combust. Flame* 1998, in press.
- Kramer, H. A.; Kitzmeyer, J. On the Slip of a Diffusing Gas Mixture Along a Wall. *Physica* 1943, 10(8), 689-713.
- Li, W.; Davis, E. J. Measurement of the Thermophoretic Force by Electroosmotic Levitation: Microspheres in Air. *J. Aerosol Sci.* 1994, 25(7), 1063-1083.
- Li, W.; Davis, E. J. The Effects of Gas and Particle Properties on Thermophoresis. *J. Aerosol Sci.* 1995b, 26(7), 1085-1099.
- Li, W.; Davis, E. J. Aerosol Evaporation in the Transition Regime. *Aerosol Sci. Technol.* 1996, in press.
- Loyalka, S. K.; Ferriger, J. H. Model Dependence of the Temperature Slip Coefficient. *Phys. Fluids* 1988, 11, 1688-1671.
- Loyalka, S. K.; Cipolla, J. W., Jr. Thermal Creep Slip With Arbitrary Accommodation at the Surface. *Phys. Fluids* 1971, 14(8), 1656-1661.
- Loyalka, S. K. Temperature Jump and Thermal Creep Slip: Rigid Sphere Gas. *Phys. Fluids A* 1989, 1(2), 403-408.
- Mackowski, D. W. Photophoresis of Aerosol Particles in the Free-Molecular and Slip-Flow Regimes. *Int. J. Heat Mass Transfer* 1989, 32(6), 843-854.
- Mackowski, D. W. Phoretic Behavior of Asymmetric Particles in Thermal Non-equilibrium With the Gas: Two-Sphere Aggregates. *J. Colloid Interface Sci.* 1990, 140(1), 139-157.
- Mackowski, D. W.; Rao, V. R.; Walker, D. G.; Knight, R. W. Numerical Investigation of the Effects of Thermal Creep in Physical Vapor Transport. *J. Cryst. Growth* 1994, in press.
- Mackowski, D. W.; Tsaproulis, M.; Roemer, D. E. Effect of Radiative Heat Transfer on the Coagulation Rates of Combustion-Generated Particles. *Aerosol Sci. Technol.* (AIChE) 1994, 20(1), 83.
- Mantell, D. A.; Kunitomi, K. K.; Ryall, S. B.; Haller, G. L. The Dynamics of CO Oxidation on Pt From Translational, Rotational and Vibrational Excitation in the Product CO. *Surf. Sci.* 1984, 172, 281.
- Mason, E. A.; Chapman, S. Motion of Small Suspended Particles in Non-Uniform Gases. *J. Chem. Phys.* 1942, 36(3), 627-632.
- McNabb, G.; Meisen, A. J. Thermophoresis in Liquids. *J. Colloid Interface Sci.* 1978, 67, 339-346.
- Millikan, R. A. Coefficients of the Slip in Gases and the Law of Reflection of Molecules from the Surface of Solids and Liquids. *Phys. Rev.* 1925, 27, 217-238.
- Miquel, P. F. Flame synthesis of Nanostructured Mixed Oxides and its Application to the Formation of Catalysts. Ph.D. Dissertation, Department of Chemical Engineering, Graduate School, Johns Hopkins University, 1995.
- Mo, G.; Rosenberger, F. Molecular Dynamics Simulation of Flow in a Two-Dimensional Channel With Atomically Rough Walls. *Phys. Rev. A* 1990, 42, 4698.
- Morris, D. J.; Hanson, L.; Garcia, A. L. Slip Length in Dilute Gas. *Phys. Rev. A* 1992, 46, 6279-6291.
- Nowrer, D. A. The Bary-Effect and An Appropriate Momentum Boundary Condition. *Phys. Fluids A* 1990, 2(6), 858-865.
- Papadopoulos, D. H. Internal Flows Induced by Kinetic Boundary Layer Phenomena. Ph.D. Dissertation, Department of Chemical Engineering, Graduate School, Yale University, 1996.
- Papadopoulos, D. H.; Roemer, D. E. Enclosure Gas Flows Driven by Non-isothermal Walls. *Phys. Fluids* 1995, 7(11), 2635-2637.
- Papadopoulos, D. H.; Roemer, D. E. Direct Simulation of Concentration Creep in a Binary Gas-Filled Enclosure. *Phys. Fluids* 1994, to appear.
- Park, H. M.; Roemer, D. E. Combined Inertial and Thermophoretic Effects on Particle Deposition Rates in Highly Loaded Dusty Gas Systems. *Chem. Eng. Sci.* 1989, 44(10), 2233-2244.
- Probst, R. F. *Physicochemical Hydrodynamics*; Butterworth-Heinemann: Stoneham, MA, 1989. For a recent account of Marangoni-driven flow experiments under microgravity conditions, see Kamotani et al., 1995.
- Rosenblatt, G. M.; Lee, P. K. *J. Chem. Phys.* 1969, 49, 2995.
- Roemer, D. E. High Temperature Gas-Solid Reactions. *Annu. Rev. Mater. Sci.* 1972, 2, 573-606.
- Roemer, D. E. Energy, Mass, and Momentum Transport: The Treatment of Jump Conditions at Phase Boundaries and Fluid-dynamic Discontinuities. *Chem. Eng. Educ.* 1978, X(4), 190-194.
- Roemer, D. E. Thermal (Soret) Diffusion Effects on Interfacial Mass Transport Rates. *PhysicoChem. Hydrodyn.* 1980, 1, 169-185.
- Roemer, D. E. Mass Transfer Across Combustion Gas Thermal Boundary Layers Power Production and Materials Processing Implications. *Heat Transfer in Fire and Combustion Systems*; HTD 45; ASME: New York, pp 8-8. See also: Proc. Symp. High Temp. Lump Chem., *Electrochem. Soc.* 1988, 88-4, 111-138.
- Roemer, D. E. Side-Wall Gas "Creep" and Thermal Stress Convection in Microgravity Experiments on Film Growth by Vapor Transport. *Phys. Fluids A* 1989, 1(1), 1761-1763.
- Roemer, D. E. Transport Processes in Chemically Reacting Flow Systems, 2nd ed.; Butterworth-Heinemann: Stoneham, MA, 1986; 3rd printing, 1990; 2nd edition, in preparation.
- Roemer, D. E.; Chung, H. M.; Fong, H. Resistance Relaxation Studies of Gas/Metal Reactions Leading to Simultaneous Dissolution and Gasification. *J. Chem. Soc., Faraday Trans. 1* 1978, 72, 842-867, 853-875.
- Roemer, D. E.; Mackowski, D. W.; Garcia-Ybarra, P. Size- and Structure Insensitivity of the Thermophoretic Transport of Aggregated "Soot" Particles in Gases. *Combust. Sci. Technol.* 1991, 80(1-3), 87-101.
- Roemer, D. E.; Mackowski, D. W.; Tsaproulis, M.; Castellino, J. L.; Garcia-Ybarra, P. Effects of Heat Transfer on the Dynamics and Transport of Small Particles in Gases. *Ind. Eng. Chem. Res.* 1992, 31, 760-769.
- Roemer, D. E.; Park, H. Thermophoretically Augmented Mass Momentum and Energy Transfer Rates in High Particle Mass Loaded Laminar Forced Convection Systems. *Chem. Eng. Sci.* 1988, 43(10), 2689-2704.
- Ruckenstein, E. Can Phoretic Motions be Treated as Interfacial Tension Gradient-Driven Phenomena? *J. Colloid Interface Sci.* 1981, 83(1), 77-81.
- Sarasa, S. C.; Joshi, R. K. *Thermal Accommodation and Adsorption Coefficients of Gases*; Hemisphere: Washington, DC, 1989.
- Schaeff, S. A.; Chembok, P. L. Flow of Rarefied Gases. Section H. *Fundamentals of Gas Dynamics*; Princeton University Press: Princeton, NJ, 1968; pp 697-739.
- Shields, F. D. Energy and Momentum Accommodation Coefficients on Platinum and Silver. *J. Chem. Phys.* 1963, 38(6), Part I, 3329-3333.
- Shields, F. D.; Lee, K. P. and Wiley, W. J. Numerical Solution for Sound Velocity and Absorption in Cylindrical Tubes, 1. *J. Acoust. Soc. America* 1968, 57(4), 724-729.
- Shimizu, M.; Liu, G.; Giddings, J. C. Separation of Particles in Non-Aqueous Suspensions by Thermofield-Flow Fractionation. *Anal. Chem.* 1995, 67(14), 2705-2713.
- Somorjai, G. A. *Chemistry in Two Dimensions*; Cornell University Press: Ithaca, NY, 1981.
- Somorjai, G. A.; Lester, J. E. Evaporation Mechanisms of Solids. *In Progress in Solid State Chemistry*; Reiss, H., Ed.; Pergamon Press: Oxford, U.K., 1987; Chapter 1, Vol. 4, pp 1-52.
- Standard, G. The Thermodynamic Significance of "Danceworld" Boundary Conditions. *Chem. Eng. Sci.* 1968, 23, 645-655.
- Stefanov, S.; Corciunan, C. Monte-Carlo Simulation of the Taylor-Couette Flow of a Rarefied Gas. *J. Fluid Mech.* 1993, 256, 199.
- Talbot, L. Thermophoresis. *AIChE J.* 1963, 9, 467-483.
- Tandon, P.; Roemer, D. E. International Brevian Diffusion Coefficient of Large (Multiparticle) Suspended Aggregates. *Ind. Eng. Chem. Res.* 1995, 34, 3265-3277.

- Tsien, H.-S. *Supercavitodynamics: Mechanics of Rarefied Gases*, *J. Aeronaut. Sci.* 1948, 15, 663-664.
- Viviani, A.; Savino, R. *Recent Developments in Vapor Crystal Growth Fluid Dynamics*, *J. Cryst. Growth* 1993, 131, 217-229.
- See, also: Napolitano, L. G.; Viviani, A.; Savino, R. *Acta Astronaut.* 1992, 29, 197.
- Wadsworth, D. *Slip Effects in a Confined Rarefied Gas*, I. *Temperature Slip*, *Phys. Fluids A* 1993, 5, 1831-1839.
- Walker, K. L.; Honey, G. M.; Geyling, F. T. *Thermophoretic Deposition of Small Particles in Laminar Tube Flow*, *J. Colloid Interface Sci.* 1979, 71, 130-147.
- Williams, M. M. R.; Loyalka, S. K. *Aerosol Science: Theory and Practice With Special Applications to the Nuclear Industry*; Pergamon: Oxford, U.K., 1991.
- Xing, Y.; Koylu, U. O.; Roemer, D. E. *Synthesis and Restructuring of Nanoparticles in Counterflow Diffusion Flames*, *Combust. Phys.* 1995, 81, 1-10.
- Xu, W.; Koylu, U. O.; Tisdon, P.; Roemer, D. E. *Measuring and Modeling the Size, Shape and Morphological Evolution of Particles in a Single Counterflow Diffusion Flame*, *Proceedings of the 5th World Congress on Chemical Engineering*, San Diego, CA, July 1996; Paper 684, Vol. V, pp 43-48.

Footnotes

- (1) However, mention should be made of low sublimation (or desublimation) probabilities, α_s , when even single-component solids evaporate (or are condensed). This causes sublimation rates based only on equilibrium vapor pressure data to be overpredicted (and also underpredictions of the sensitivity of the sublimation rate to surface temperature). Low and T_s -dependent α_s values are associated with smooth solid surfaces in systems where the act of "physical" sublimation involves considerable steric rearrangement (as in the sublimation of arsenic: $4As(s) = As_4(g)$, for which $\alpha_s = O(10^{-9})$ (Rozenblat and Lee, 1968). A compendium of such evaporation coefficient data is given in, e.g., Somorjai and Lester, 1987; Henschel, 1981. Of course, some chemical reaction probabilities are high ($O(10^{-1}-10^7)$), especially for atoms (radical/oxid reactions forming volatile products (see, e.g., Roemer, 1972).
- (2) Rozenblat (1981) also established conditions under which such phoresis is analogous to the Marangoni motion of emulsion droplets (see, e.g., Probert, 1986; Edwards *et al.*, 1991) in the sense that the corresponding phoretic velocity can be expressed as the product of the fluidity of the host solvent and the change in surface energy over one appropriate interaction length (Debye sheath thickness, ...).
- (3) When the Knudsen sublayer thickness is not negligible compared to the local radius of curvature of the condensed phase interface, we must account for the differences in area across the KSL. This is the case for the evaporation or growth of small droplets in, say, air under conditions such that the mean-free-path, λ , is nonnegligible compared to the droplet radius (Fuchs and Sutugin, 1970; Fuchs, 1964; Williams and Loyalka, 1991).
- (4) Recall that if the KSL/condensed phase interface is itself the site of chemical and/or phase change, then λ_f will generally not be continuous across it and there will be a net mass flux G passing through the interface. In such cases we can usually impose $[G] = 0$ and $[G\lambda_f] = [G\lambda_f]$ where λ_f is the "total" specific activity (Roemer, 1989).
- (5) When the "solid" is itself porous, there is only an apparent slip due to the permeability of the porous medium (see, e.g., Tisdon and Roemer, 1995). We do not consider such interfaces here (see, e.g., section 6).
- (6) For polyatomic gas molecules a reasonable approximation to the Froude number Fr (momentum/heat diffusivity ratio)

is $[1 + (84\lambda_f - 1)\gamma]^{-1}$ (Eucken); which reduces to $\gamma/2$ for the case of a monatomic gas without electronic excitation ($\gamma = 5/2$). In this important limiting case, $(\gamma + 1)/2\gamma Pr = 8/15 \approx 0.533$ so that α_f (eqs 2-12) and α_s (eqs 2-14) are nearly equal.

(7) Common examples of important jumps in a continuous (K) regime at a gas/condensed phase interface: (a) Chemical nonequilibrium may be small enough to be well into the continuum regime ($\gamma = 5/2$), the chemical reaction probability, α_{cr} (eqs 2-12) written as, may itself be exceedingly small (Somorjai and Loyalka, 1987; Fuchs, 1964; Williams, 1991). (b) Poor energy accommodation, α_{en} , at the interface in the case of a gas can be as low as 5×10^{-3} . See section 4 for examples. (c) The mean radius of experimental EAC-values, λ_{EAC} , can be as low as 10^{-6} m (see, e.g., section 4).

(8) Of course, A_1 and A_2 must also be α_{en} -dependent. For example when $K_{O_2} \rightarrow C_{O_2} - 2K_{N_2}A_1 + A_2$. Comparison of this result with Epstein's (1929) result for the free-molecule drag on a solid sphere gives $(A_1 + A_2) \approx 9(1 + \alpha_f)/8\lambda_{EAC}^{-1}$. For the mass-transfer analog of C_{O_2} , see, e.g., Li and Davis, 1996.

(9) Note that, even if $K_{O_2} \ll 1$, the diameter dependence of f_1 and D_1 can depart noticeably from d_p^2 and d_p^{-1} , respectively, as a result of the importance of C_{O_2} (K_{N_2} , α_{en}).

(10) This result was subsequently generalized by Brock (1982), Talbot (1981), and Loyalka (1989) to extend the domain of Knudsen number applicability, including the free-molecule (Waldmann) limit for nonspherical particles (Garcia-Ybarra and Roemer, 1989).

(11) Experimentally, this effect is not so pronounced (see, e.g., Li and Davis, 1996). A comprehensive theory based on the linearized Boltzmann equation (moment method solution) covering the entire range of Kn and k_p/k_s values has been given by Beresnev and Chernyak (1995).

(12) An interesting and important corollary of the importance of particle thermophoresis in gaseous systems with appreciable temperature gradients (e.g., combustors) is that, in such systems, particles can be brought to rest ("straggle") at spatial positions systematically different from the position(s) at which the hot gas is brought to rest (Gomes and Roemer, 1993). In particle synthesis flames this "particle stagnation point" phenomenon can be exploited to control particle morphology and chemistry (Gomes and Roemer, 1993; Miquel, 1995), whereas in CVD reactors such locations may be prone to the growth of larger contaminant aggregates by localized coagulation (Davis *et al.*, 1993).

(13) As pointed out by P. J. W. Debye some time ago, C. Ludwig (1866) appears to have discovered the "Soret effect" some 23 years before Soret!

(14) As pointed out by Kogan (1973, 1980) and Roemer (1989), thermal stresses (associated with Burnett terms) can drive nontrivial gas flows far from (comothermal or piecewise isothermal) walls. Continuum calculations of such flows are contained in Mickowski *et al.* (1996) and Viviani *et al.* (1995).

Received for review January 26, 1996
Revised manuscript received July 1, 1996
Accepted July 1, 1996

IE9600351

Abstract published in *Advances ACS Abstracts*, August 15, 1996.

REPORT DOCUMENTATION PAGE

Form Approved
OMB No. 0704-0188

Public reporting burden for this collection of information is estimated to average 1 hour per response, including the time for reviewing instructions, searching existing data sources, gathering and maintaining the data needed, and completing and reviewing the collection of information. Send comments regarding this burden estimate or any other aspect of this collection of information, including suggestions for reducing this burden, to Washington Headquarters Service, Directorate for Information Operations and Reports, 1215 Jefferson Davis Highway, Suite 1204, Arlington, VA 22202-4302, and to the Office of Management and Budget, Paperwork Reduction Project (0704-0188), Washington, DC 20503.

1. AGENCY USE ONLY (Leave blank) 2. REPORT DATE 1996 3. REPORT TYPE AND DATES COVERED Reprint

4. TITLE AND SUBTITLE
Erosion rate prediction and correlation technique for ceramic surfaces exposed to high speed flows of abrasive suspensions

5. FUNDING NUMBERS
PE - 61102F
PR - 2308
SA - BS
G - F49620-94-1-0143

6. AUTHOR(S)
Yehia F. Khalil, Daniel E. Rosner

7. PERFORMING ORGANIZATION NAME(S) AND ADDRESS(ES)
Yale University
High Temperature Chemical Reaction Engineering Laboratory
Department of Chemical Engineering
PO Box 208286 YS, New Haven, CT 06520-8286 USA

8. PERFORMING ORGANIZATION REPORT NUMBER

9. SPONSORING/MONITORING AGENCY NAME(S) AND ADDRESS(ES)
AFOSR/NA
110 Duncan Avenue, Suite B115
Bolling AFB DC 20332-0001

10. SPONSORING/MONITORING AGENCY REPORT NUMBER

11. SUPPLEMENTARY NOTES
Wear 201 (1996) 64-79

12a. DISTRIBUTION/AVAILABILITY STATEMENT
Approved for public release; distribution is unlimited

12b. DISTRIBUTION CODE

13. ABSTRACT (Maximum 200 words)

We describe a simple method to predict (based on available erosion yield data) erosion rates for cylindrical ceramic targets (e.g. circular tube coatings, leading edges of turbine blades, or the ceramic-lined target zone inside CFBC-cyclones) exposed to high-speed abrasive particle-laden streams. Use is made of a convenient parameterization/extrapolation of published laboratory results giving, in effect, average erosion yields per particle impact (ϵ_p) for particular planar ceramic target and projectile materials over a range of impact velocities, V_p , incidence angles, θ_i , and particle sizes, v_p . For a given target/flow geometry we reduce the engineering problem of predicting absolute target erosion rates to that of multiplying a readily calculated characteristic erosion rate by the universal dimensionless erosion rate functions explicitly approximated here in the limit of impacts by particles large enough to be undeflected or slowed down by the local target gas flow. Our characteristic erosion rate is that which would be associated with the mainstream abrasive particle volume flux if all particles struck at normal incidence with the mainstream velocity, U . Dimensionless erosion rate results are cast in terms of the following four dimensionless parameters characterizing the erodent/ceramic target system of interest: sensitivity (exponent n) of erosion yield to projectile incident velocity; sensitivity (exponent m appearing in $(\cos^m \theta_i)$) of erosion yield to angle of incidence θ_i ; sensitivity (exponent l) of erosion yield to projectile particle size (volume, v_p); and the reference erosion yield, $\epsilon_{p,ref}$ (here, ϵ_p is evaluated at $V_p = 100 \text{ m s}^{-1}$, $\theta_i = 0$, and v_p corresponding to $d_p = 100 \mu\text{m}$). Based on our preliminary survey of available erosion yield experimental data, we provide a table giving "best-fit" values of the four parameters: l , m , n , and $\epsilon_{p,ref}$ required to complete a prediction of local and spatially-averaged erosion rates according to our present formalism. For the latter, useful closed-form approximations are provided for convex or concave cylindrical target geometries in the high Stokes number limit. Moreover, convenient correction factors are developed to account for a (Rosin-Rammler) particle size distribution in the erodent mainstream, and mainstreams not perpendicular to the cylinder axis. The more general case of arbitrary (finite) Stokes numbers is outlined. Using two numerical examples (convex leading edge coating on a turbine stator blade, and concave sector target zone in a CFBC-cyclone), we demonstrate that casting required erosion yield data in this suggested format greatly facilitates erosion design calculations for ceramic targets (or coatings) exposed to high-speed abrasive particle suspensions. Organizing empirical data in this manner will also facilitate the longer range goal of correlating each of the above-mentioned parameters with independently measurable physical properties of the participating materials.

14. SUBJECT TERMS
erosion yield, impact erosion, ceramic targets, abrasive suspensions, turbine blades, cyclone wall erosion

15. NUMBER OF PAGES
16

16. PRICE CODE

17. SECURITY CLASSIFICATION OF REPORT
Unclassified

18. SECURITY CLASSIFICATION OF THIS PAGE
Unclassified

19. SECURITY CLASSIFICATION OF ABSTRACT
Unclassified

20. LIMITATION OF ABSTRACT
UL

Erosion rate prediction and correlation technique for ceramic surfaces exposed to high speed flows of abrasive suspensions

Yehia F. Khalil, Daniel E. Rosner *

High Temperature Chemical Reaction Engineering Laboratory, Yale University, Department of Chemical Engineering, New Haven, CT 06520-8286, USA

Received 14 August 1995; accepted 3 April 1996

Abstract

We describe a simple method to predict (based on available erosion yield data) erosion rates for cylindrical ceramic targets (e.g. circular tube coatings, leading edges of turbine blades, or the ceramic-lined target zone inside CFBC-cyclones) exposed to high-speed abrasive particle-laden streams. Use is made of a convenient parameterization/extrapolation of published laboratory results giving, in effect, average erosion yields per particle impact (ϕ_p) for particular planar ceramic target and projectile materials over a range of impact velocities, v_p , incidence angles, θ , and particle sizes, ψ_p . For a given target/flow geometry we reduce the engineering problem of predicting absolute target erosion rates to that of multiplying a readily calculated characteristic erosion rate by the universal, dimensionless erosion rate functions explicitly approximated here in the limit of impacts by particles large enough to be undeflected or slowed down by the local target gas flow. Our characteristic erosion rate is that which would be associated with the mainstream abrasive particle volume flux if all particles struck at normal incidence with the mainstream velocity, U . Dimensionless erosion rate results are cast in terms of the following four dimensionless parameters characterizing the erodent/ceramic target system of interest: sensitivity (exponent n) of erosion yield to projectile incident velocity; sensitivity (exponent m appearing in $\cos^m(\theta)$) of erosion yield to angle of incidence θ ; sensitivity (exponent β) of erosion yield to projectile particle size (volume, ψ_p); and the reference erosion yield, ϕ_{ref} (here, ϕ_p is evaluated at $v_p = 100 \text{ m s}^{-1}$, $\theta = 0$, and ψ_p corresponding to $d_p = 100 \mu\text{m}$). Based on our preliminary survey of available erosion yield experimental data, we provide a table giving "best-fit" values of the four parameters: l , m , n , and ϕ_{ref} required to complete a prediction of local and spatially-averaged erosion rates according to our present formalism. For the latter, useful closed-form approximations are provided for convex or concave cylindrical target geometries in the high Stokes number limit. Moreover, convenient correction factors are developed to account for a (Rosin-Rammler) particle size distribution in the erodent mainstream, and mainstream not perpendicular to the cylinder axis. The more general case of arbitrary (finite) Stokes numbers is outlined. Using two numerical examples (convex leading edge coating on a turbine stator blade, and concave sector target zone in a CFBC-cyclone), we demonstrate that casting required erosion yield data in this suggested format greatly facilitates erosion design calculations for ceramic targets (or coatings) exposed to high-speed abrasive particle suspensions. Organizing empirical data in this manner will also facilitate the longer range goal of correlating each of the above-mentioned parameters with independently measurable physical properties of the participating materials.

Keywords: Erosion rates; Ceramic targets; Abrasive suspensions; Inertial impaction; Tube coatings; CFBC-cyclone erosion; Turbine blade erosion

1. Introduction

1.1. Background

Solid material erosion by the impingement of fine particles entrained in a high velocity stream results in material wastage and forced outages in many chemical and power plants [1,2]. For example, severe erosion problems have been encountered in equipment used in the fluidized bed reactors, gas and steam turbines, cyclone separators, and coal hydrogenation equipment [3-5]. Therefore, a wide variety of ceramic materials

has been proposed as erosion-resistant protective coatings, often applied only locally. To design/optimize refractory-lined parts (such as the ceramic coating on turbine blades, the liner of a circulating fluidized bed combustor (CFBC) hot cyclone [6], or the refractory-lined solids return loop between cyclones and combustors), it is clearly necessary to anticipate the local and total erosion rates in the prevailing environment. The methods introduced and demonstrated here will not only permit this for systems which have been studied in laboratory erosion test-rigs, they will also facilitate the important task of correlating the experimental erosion yield parameters we introduce and tabulate (Table 1) with inde-

pendently measurable physical properties of the participating materials.

Of course, there are many useful applications of erosion by fine particles impinging on ceramic target surfaces [7-17]. For example, sand-blasting techniques are often used to mechanically clean solid surfaces [3]. Additional applications include the erosive cutting and drilling of hard materials [18]. Indeed, we believe that our present approach, with extensions as indicated in Section 4.4, will be able to predict/correlate attainable cutting and drilling rates.

1.2. Objectives

The principal objective of this work is to extend our novel reformulation of the metal erosion problem [19,29] and develop a rather simple method for predicting erosion rates for ceramic target surfaces exposed to high-speed abrasive particle-laden streams. Regarding ceramic targets, two geometrical configurations of special industrial interest (Fig. 1) are explicitly considered in this work: (1) cylindrical ceramic-coated targets in external cross-flow and (2) refractory lined target surfaces, such as those installed on the inner walls of CFBC cyclones.

To achieve our present objective, available ceramic target erosion yield data are re-examined and cast into a useful format which provides (Table 1) for each target/erodent system four best fit erosion parameters that can be used to predict ceramic cylinder erosion rates (see Section 4.1). However, as noted in Section 5, organizing available experimental data in this particular way will also facilitate the longer-range goal

of correlating each of the above-mentioned parameters with independently measurable physical properties of the participating materials.

1.3. Approach

This paper is structured as follows. In Section 2, our principal underlying assumptions are presented. We include a discussion of the proposed erosion yield law and derive/present quadrature expressions for the above-mentioned dimensionless erosion rate functions of greatest practical interest. For simplicity, our emphasis here is on the "worst-case" situation, i.e. the limit of infinite Stokes number (rectilinear particle trajectories).

In Section 3, we present our methods to estimate erosion yield parameters from available erosion yield data and report these parameters for a set of 38 common ceramic target/erodent systems at near 300 K. In Section 4, we provide results for local, maximum, and average erosion rates and provide two numerical examples for calculating erosion of a ceramic target surface; the first example pertains to turbine blade (stator) leading edges, and the second deals with the refractory lining of a CFBC cyclone. Section 5 provides a summary of our principal findings and recommendations for future work.

2. Mathematical model and outline of formulation

2.1. Basic assumptions

The following simplifying Assumptions are exploited here to capture the essential phenomena encountered in ceramic material erosion:

1. Erosion yield data obtained on planar ceramic targets in test rigs can be self-consistently invoked locally at the surface of large curved ceramic targets (e.g. cylinders) since the target radius of curvature ($d_t/2$) far exceeds the scale of the erodent particle radii (and target grain sizes) of interest here.
2. Rebounding particles do not appreciably influence incoming particles, nor cause significant downstream erosion upon re-impaction on the same target.
3. On the scale of the target radius of curvature, ($d_t/2$) for a circular cylinder) the mainstream suspended particles are uniformly distributed in space and are individually negligible in size (cf (1)).
4. While the particle mass loadings, ϕ_p , in the mainstream may not be very small, the volume fraction, ϕ_v , corresponding to the total particle number density N_p and mean particle volume \bar{v}_p (i.e. $\phi_v = N_p \bar{v}_p$) is negligible compared with unity.
5. Target surface recession due to erosion is small on the scale of the initial target radius of curvature.

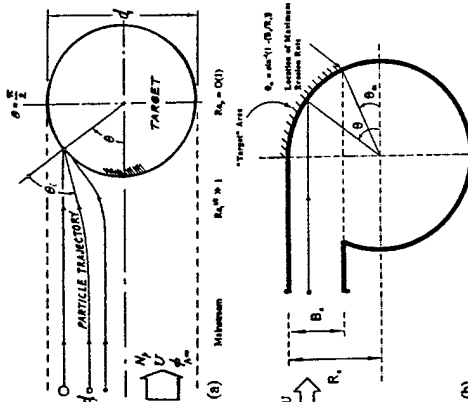


Fig. 1. (a) Circular cylinder target in external cross-flow: configuration and nomenclature. (b) Impingement (target) sector of cyclone inner walls: configuration and nomenclature.

* Corresponding author.

Table 1

Ceramic target and abrasive material combinations: Best-fit values of the erosion yield parameters *l , m , n , and ρ_{erod}

Target material/erodent system no.	Target material	Eroder type, particle size, and velocity				Erosion parameters				Data source
		Type	d_p (μm)	V_p (m s^{-1})	ρ_{erod} (g cm^{-3})	l	m	n	ρ_{erod}	
1	Castable A: 96% High-purity alumina castable	Dead-burned dolomite Density: 3.0 g cm^{-3}	450-680	10.1	1.3	1.3	3.0	9.63-4	Kasims et al. [1]	
			450-950	12.2	1.3	1.3	3.0	9.63-4		
2	Castable C: Chrome castable, $\text{Cr}_2\text{O}_3/\text{Al}_2\text{O}_3$	Dead-burned dolomite Density: 3.0 g cm^{-3}	450-950	14.3	1.3	1.3	3.0	9.63-4	Kasims et al. [1]	
			680	10.1	1.2	1.1	2.5	7.23-5		
3	Castable P: Light weight castable	Dead-burned dolomite Density: 3.0 g cm^{-3}	950	12.2	1.2	1.1	2.5	7.23-5	Kasims et al. [1]	
			500	14.3	1.2	1.2	2.5	7.23-5		
4	Glass: Density: 2.47 g cm^{-3}	Silica flour: SiO_2 Density: 2.65 g cm^{-3}	500-950	10.1	1.0	1.0	2.9	7.83-5	Head and Harr [20]	
			450-950	12.2	1.0	1.0	2.9	7.83-5		
5	Glass: Density: 2.47 g cm^{-3}	Crysochlor: SiC Density: 3.17 g cm^{-3}	500-680	14.3	1.0	1.0	2.9	7.83-5	Head and Harr [20]	
			25	14.9	1.2	2.5	2.3	7.23-1		
6	Glass: Density: 2.47 g cm^{-3}	Aluminum: Al_2O_3 Density: 4.00 g cm^{-3}	39	14.0	1.2	1.8	2.3	2.33-1	Head and Harr [20]	
			39	14.0	1.2	1.8	2.3	2.43-1		
7	Glass: Density: 2.47 g cm^{-3}	Glass beads Density: 2.47 g cm^{-3}	38	13.6	1.2	6.3	2.3	5.63-2	Head and Harr [20]	
			150	5.5	1.2	0.6	2.8	7.33-7		
8	High purity refractory: 95% Al_2O_3 castable refractory bonded with calcium aluminate cement	Silicon carbide Density: 3.17 g cm^{-3}	150	5.5	1.2	0.6	2.8	7.33-7	Widensson and Roberts [21]	
			400	11.6	1.2	0.5	2.3	1.33-3		
9	Insulating refractory concrete: Aluminous cement A and perlite Density: 0.80 g cm^{-3}	Sand Density: 2.4 g cm^{-3}	400	11.6	1.2	0.5	2.3	1.33-3	Crowley [22]	
			1760	11.6	1.2	1.4	2.3	1.43-5		
10	Insulating refractory concrete: Aluminous cement A and perlite Density: 0.80 g cm^{-3}	Blasting grit Density: 2.65 g cm^{-3}	1760	11.6	1.2	1.4	2.3	1.43-5	Crowley [22]	
			400	11.6	1.2	1.6	2.3	1.63-7		
11	Abrasion resistant refractory concrete C: Aluminous cement B and chrome ore aggregate Density: 2.31 g cm^{-3}	Blasting grit Density: 2.65 g cm^{-3}	1760	11.6	1.2	1.6	2.3	1.63-7	Crowley [22]	
			400	11.6	1.2	4.4	2.3	8.93-6		
12	Abrasion resistant refractory concrete C: Aluminous cement B and chrome ore aggregate Density: 2.31 g cm^{-3}	Sand Density: 2.4 g cm^{-3}	400	11.6	1.2	4.4	2.3	8.93-6	Crowley [22]	
			1760	11.6	1.2	3.6	2.3	2.03-6		
13	High strength refractory concrete: Aluminous cement A and calcined fireclay Density: 2.05 g cm^{-3}	Blasting grit Density: 2.65 g cm^{-3}	1760	11.6	1.2	3.6	2.3	2.03-6	Crowley [22]	
			400	11.6	1.2	3.6	2.3	2.03-6		

(continued)

Table 1 (continued)

Target material/erodent system no.	Target material	Eroder type, particle size, and velocity				Erosion parameters				Data source
		Type	d_p (μm)	V_p (m s^{-1})	ρ_{erod} (g cm^{-3})	l	m	n	ρ_{erod}	
14	High strength refractory concrete: Aluminous cement A and calcined fireclay Density: 2.05 g cm^{-3}	Sand Density: 2.4 g cm^{-3}	400	11.6	1.2	3.0	2.3	1.13-3	Crowley [22]	
			580	13.0	1.2	2.5	2.3	1.43-4		
15	Unannealed glass: Density: 2.47 g cm^{-3}	Cast iron Density: 7.8 g cm^{-3}	580	30.5	1.2	2.5	2.3	1.43-4	Plimle [3]	
			580	30.5	1.2	2.7	2.3	1.13-5		
16	Unannealed glass: Density: 2.47 g cm^{-3}	Cast iron Density: 7.8 g cm^{-3}	300	9.9	1.2	3.5	2.3	2.53-4	Blither [23]	
			500	60.0	1.2	N/A	2.3	9.83-5		
17	Annealed glass: Density: 2.47 g cm^{-3}	Silicon carbide Density: 3.22 g cm^{-3}	500	60.0	1.2	N/A	2.3	1.23-4	Liebbard [24]	
			500	60.0	1.2	N/A	2.3	1.83-4		
18	Annealed glass: Density: 2.47 g cm^{-3}	Silicon carbide Density: 3.22 g cm^{-3}	500	60.0	1.2	N/A	2.3	2.03-4	Liebbard [24]	
			500	60.0	1.2	N/A	2.3	2.23-4		
19	Annealed glass: Density: 2.47 g cm^{-3}	Silicon carbide Density: 3.22 g cm^{-3}	500	60.0	1.2	N/A	2.3	2.43-4	Liebbard [24]	
			500	60.0	1.2	N/A	2.3	2.03-4		
20	Annealed glass: Density: 2.47 g cm^{-3}	Silicon carbide Density: 3.22 g cm^{-3}	500	60.0	1.2	N/A	2.3	2.03-4	Liebbard [24]	
			500	60.0	1.2	N/A	2.3	2.23-4		
21	Annealed glass: Density: 2.47 g cm^{-3}	Silicon carbide Density: 3.22 g cm^{-3}	500	60.0	1.2	N/A	2.3	2.03-4	Liebbard [24]	
			500	60.0	1.2	N/A	2.3	2.23-4		
22	Annealed glass: Density: 2.47 g cm^{-3}	Silicon carbide Density: 3.22 g cm^{-3}	500	60.0	1.2	N/A	2.3	2.03-4	Liebbard [24]	
			500	60.0	1.2	N/A	2.3	2.23-4		
23	Annealed glass: Density: 2.47 g cm^{-3}	Silicon carbide Density: 3.22 g cm^{-3}	500	60.0	1.2	N/A	2.3	2.03-4	Liebbard [24]	
			500	60.0	1.2	N/A	2.3	2.23-4		
24	Annealed glass: Density: 2.47 g cm^{-3}	Silicon carbide Density: 3.22 g cm^{-3}	500	60.0	1.2	N/A	2.3	2.43-4	Liebbard [24]	
			500	60.0	1.2	N/A	2.3	2.53-4		
25	Annealed glass: Density: 2.47 g cm^{-3}	Silicon carbide Density: 3.22 g cm^{-3}	500	60.0	1.2	N/A	2.3	2.53-4	Liebbard [24]	
			500	60.0	1.2	N/A	2.3	2.83-4		
26	Annealed glass: Density: 2.47 g cm^{-3}	Silicon carbide Density: 3.22 g cm^{-3}	500	60.0	1.2	N/A	2.3	2.83-4	Liebbard [24]	
			500	60.0	1.2	N/A	2.3	2.03-4		
27	Annealed glass: Density: 2.47 g cm^{-3}	Silicon carbide Density: 3.22 g cm^{-3}	500	60.0	1.2	N/A	2.3	2.83-4	Liebbard [24]	
			500	60.0	1.2	N/A	2.3	4.03-4		
28	Annealed glass: Density: 2.47 g cm^{-3}	Silicon carbide Density: 3.22 g cm^{-3}	500	60.0	1.2	N/A	2.3	4.03-4	Liebbard [24]	
			500	60.0	1.2	N/A	2.3	4.03-4		
29	Annealed glass: Density: 2.47 g cm^{-3}	Silicon carbide Density: 3.22 g cm^{-3}	500	60.0	1.2	N/A	2.3	4.03-4	Liebbard [24]	
			500	60.0	1.2	N/A	2.3	4.13-4		
30	Annealed glass: Density: 2.47 g cm^{-3}	Silicon carbide Density: 3.22 g cm^{-3}	500	60.0	1.2	N/A	2.3	4.13-4	Liebbard [24]	
			500	60.0	1.2	N/A	2.3	4.03-4		
31	Annealed glass: Density: 2.47 g cm^{-3}	Silicon carbide Density: 3.22 g cm^{-3}	500	60.0	1.2	N/A	2.3	4.03-4	Liebbard [24]	
			500	60.0	1.2	N/A	2.3	4.03-4		

(continued)

Table 1 (continued)

Target material/erosion system no.	Target material		Erosion type, particle size, and velocity		Erosion parameters				Data source
	Type	Density	d_p (μm)	V_p (m s^{-1})	l	m	n	ϕ_{opt}	
32	Abrasion resistant castable: Density: 2.08 g cm^{-3}	Silicon carbide Density: 3.22 g cm^{-3}	500	60.0	1.2	N/A	2.3	5.0E-4	Liebard [24]
33	Pressureless SiC ceramic: Density: 2.98 g cm^{-3}	Silicon carbide Density: 3.22 g cm^{-3}	274	35-90	1.3	0.8	2.8	8.3E-5	Wang et al. [25]
34	Hot-pressed SiC ceramic: Density: 3.16 g cm^{-3}	Silicon carbide Density: 3.22 g cm^{-3}	274	35-90	1.3	1.5	2.8	4.0E-5	Wang et al. [25]
35	Hot isostatically pressed ceramic: Density: 3.14 g cm^{-3}	Silicon carbide Density: 3.22 g cm^{-3}	274	35-90	1.3	0.9	2.8	1.4E-5	Wang et al. [25]
36	Hot-pressed Si ₃ N ₄ ceramic: Density: 3.22 g cm^{-3}	Silicon carbide Density: 3.22 g cm^{-3}	305	117	1.3	N/A	4.0	4.6E-6	Gulden [26]
37	Reaction-bonded Si ₃ N ₄ ceramic: Density: 2.65 g cm^{-3}	Quartz Density: 2.65 g cm^{-3}	273	130	1.3	N/A	4.0	3.3E-6	Gulden [26]
38	Hot-pressed Si ₃ N ₄ ceramic: Density: 2.65 g cm^{-3}	Quartz Density: 2.65 g cm^{-3}	304	285	1.0	N/A	1.0	4.3E-7	Gulden [26]

* All erosion yield data reported here correspond to room temperature.

For systems #19 to #32 and #36 to #38, the erosion yield data were provided only at normal incidence ($\theta = 0$). Therefore, values of the erosion parameter m (Eq. (2)) cannot be provided here.

The values of l and n shown here for systems #19 to #32 were provisionally taken from the experimental results for systems #1 to #18.

6. The ceramic target material is either intrinsically isotropic, or if anisotropic (as for pyrolytic BN(s)) conformal to the smooth cylindrical substrate.

Subject to these Assumptions, some of which are critically discussed in Sections 4.3 and 4.4, we show that actual local erosion rates (say, in the units of mm recession per year of continuous exposure) at position θ (Fig. 1) can be expressed as the product of an easily calculated characteristic erosion rate (ER), and a universal dimensionless function $E(\theta, \dots)$ calculated and plotted here for two important geometries: the external upwind-facing surface of a circular cylinder in cross-flow (Fig. 1(a)), and the internal (concave) target area (sector) in a cyclone particle separator (Fig. 1(b)). The characteristic erosion rate is that which would be expected in the prevailing environment if all mainstream particles had the mean size and struck a unit area of target with undiminished speed and at normal incidence, i.e. in the units of linear recession rate:

$$(ER)_e = \phi_p(U, 0, \bar{v}_{p, \text{opt}}) \cdot (\bar{v}_p N_p U) \quad (1)$$

where ϕ_p is the specific erosion yield (average volume of target removed per unit volume of projectile particle impacting) evaluated at the particle mainstream velocity U and at normal incidence angle and at erodent particle volume \bar{v}_p (see Section 2.2), where $(\bar{v}_p N_p)_e$ is the mainstream particle volume fraction. Thus, all local erosion rates will be

For porous (not theoretically dense) ceramic targets, this necessarily includes pore volume originally "in" the undistracted target!

on particle incident velocity V_p , angle of incidence θ , and projectile particle size, d_p or ϕ_p (see, for example, Keairns et al. [1] and Section 4.4). An especially convenient representation of these experimental data for our purposes is the separable, power-law form:

$$\phi_p = \phi_{p, \text{opt}} (V_p/V_{p, \text{opt}})^m \cdot \cos^l(\theta) \cdot (d_p/d_{p, \text{opt}})^n \quad (2)$$

where $\phi_{p, \text{opt}}$ (i.e. the value of ϕ_p at $V_p = V_{p, \text{opt}} = 100 \text{ m s}^{-1}$, $\theta = 0$, and $d_p = d_{p, \text{opt}} = (\pi/6)d_{p, \text{opt}}^3 / (100)^3 \mu\text{m}^3$) is specific to the projectile/ceramic target system, and the exponent n on the particle velocity ($n = d(\ln \phi_p)/d(\ln V_p)$), a value frequently near 2.3) is chosen to fit experimental results, especially in the vicinity of normal incidence, $\theta = 0$. Similarly, the exponent l on particle volume ($l = d(\ln \phi_p)/d(\ln d_p)$), a value frequently near 1.2) is chosen to best describe available experimental results as a function of erodent particle size near $v_{p, \text{opt}}$. Note that the indicated dependence on angle of incidence, $\cos^l(\theta)$, is already normalized since $\cos^0(0) = 1$ for any m (typical values of the exponent m , not necessarily an integer, will be seen to range between 0.5 and 3.5; see, for example, Fig. 2 and Table 1).

Regarding the θ -dependence of erosion yields, the behavior and success of the simple but realistic function $\cos^l(\theta)$ is shown in Fig. 2. This functional form is seen to fit room temperature erosion rate data obtained from laboratory experiments for a wide variety of combinations of ceramic target material and projectile materials [23,22,3,1] and will be shown to facilitate the calculation of total erosion rates (Section 2.3, Figs. 3 and 4), especially in the high Stokes number limit. Note that in all cases considered here we assume that no erosion occurs for projectile particles which strike the target surface at grazing incidence ($\theta = \pi/2$ rad). Conversely, the most vulnerable angle of incidence (written as θ_p in Rosner et al. [29] and Kho et al. [19]) is zero radians (i.e. normal incidence). Some best-fit values of the four parameters l , m , n , and $\phi_{p, \text{opt}}$ which we extracted from available erosion yield measurements for a variety of ceramic targets and erodents (see Section 3), are given in Table 1.

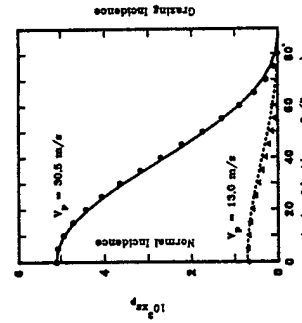


Fig. 2. Dependence of the normalized erosion yield $\phi_p/\phi_{p, \text{opt}}$ on angle of incidence (relative to target normal) for unannealed glass/cast iron erodent ($d_p = 380 \mu\text{m}$ and $V_p = 30.5 \text{ m s}^{-1}$) at 300 K (after Finnke [3]).

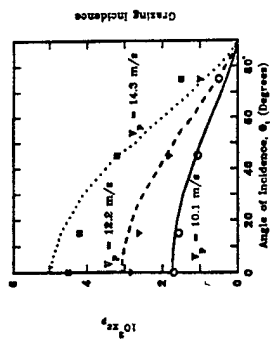


Fig. 3. Erosion yield dependence on particle velocity and angle of incidence (relative to target normal) for unannealed glass/cast iron erodent ($d_p = 380 \mu\text{m}$) at 300 K (after Finnke [3]).

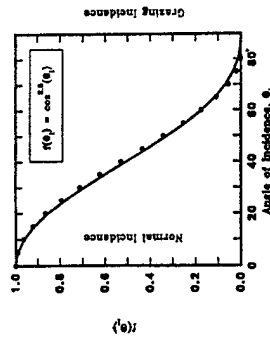


Fig. 4. Erosion yield dependence on particle velocity and angle of incidence (relative to target normal) for 96% high-purity alumina castable/oxidized dolomite erodent ($d_p = 680 \mu\text{m}$) at 300 K (after Keairns et al. [1]).

In what follows, cylindrical ceramic target results will be shown for the following representative range of the above-mentioned erosion yield parameter m : $0.5 \leq m \leq 3.0$. These graphs together with our table giving the four parameters l , m , n and $\phi_{p, \text{opt}}$ summarizing available ceramic planar target erosion rate data (Table 1), will permit rapid engineering estimates of convex or concave cylinder target erosion rates for preliminary design/optimization purposes for many combinations of practical interest (Section 4.1). However, as discussed in Section 4.2, some of these results, when combined with actual erosion rate observations on test cylinders in a reasonably well-characterized cross-flow, could be used to extract rational estimates of certain unavailable erosion yield parameters for use in subsequent design/optimization calculations.

2.3. Local and total erosion rate quadrature expressions

Consider first the task of predicting the local erosion rate at some arbitrary angular position θ on, say, a convex cylindrical ceramic target (measured from the forward stagnation line, see Fig. 1(a)). The mainstream, of velocity U , contains the number density N_p of abrasive particles distributed in size (particle volume) with the normalized size distribution func-

tion $C_m(v)$. We write the local impingement flux of particles of volume $v \pm (dv/2)$ as $\eta_{\text{local}}(v, \theta) \cdot UN_p C_m(v) dv$, which corresponds to a erosion flux $v \eta_{\text{local}}(v, \theta) \cdot UN_p C_m(v) dv$. According to the erosion yield law (Section 2.2), the corresponding contribution to the local erosion rate will be:

$$E_p(V_p(v, \theta), \theta(v, \theta), v) \eta_{\text{local}}(v, \theta) \cdot UN_p C_m(v) dv \quad (3)$$

and the total local erosion rate will therefore be given by the integral of Eq. (3) over the entire particle volume range $0 \rightarrow \infty$. Keeping in mind that, for inertial impaction, the integrand (because of $\eta_{\text{local}}(v, \theta)$) is essentially zero below some threshold volume v_{crit} corresponding to a critical Stokes number, $Stk_{\text{crit}} = 1/8$ [31,32], we can write:

$$ER = \int_0^\infty E_p(V_p(v, \theta), \theta(v, \theta), v) \eta_{\text{local}}(v, \theta) \cdot UN_p C_m(v) dv \quad (4)$$

A suitable system-specific characteristic erosion rate will clearly be:

$$(ER)_c = E_p(U, 0, \bar{v}_{p,m}) \cdot (\bar{v}_p N_p U)_{\infty} \quad (5)$$

where the product $(\bar{v}_p N_p)_{\infty}$ will be recognized as the mainstream particle volume fraction $\phi_{p,m}$. This implies that it will always be possible to calculate actual target erosion rates from the product relation:

$$ER = (ER)_c \cdot E(\theta, \dots) \quad (6)$$

where, in view of Eqs. (3)-(5), the dimensionless local erosion rate function $E(\theta, \dots)$ is explicitly given by:

$$E(\theta, \dots) = \int_0^\infty \left[\frac{E_p(V_p(v, \theta), \theta(v, \theta), v)}{E_p(U, 0, \bar{v}_{p,m})} \right] \cdot \left(\frac{v}{U} \right) \cdot \eta_{\text{local}}(v, \theta) \cdot C_m(v) dv \quad (7)$$

This is an important general result, simplified below for particles large enough to follow straight line trajectories in the vicinity of the ceramic (coated) target.

We now introduce the separable erosion yield law Eq. (2) and note that the first (bracketed) term in the integrand can then be simplified to the product of three dimensionless functions:

$$\left[\frac{E_p(V_p(v, \theta), \theta(v, \theta), v)}{E_p(U, 0, \bar{v}_{p,m})} \right] = \left(\frac{V_p(v, \theta)}{U} \right)^m \cos^m(\theta(v, \theta)) \cdot \left(\frac{v}{v_{\text{crit}}} \right) \quad (8)$$

It will be recalled that the shape function $\cos^m(\theta)$ describing the dependence of erosion yield on angle-of-incidence is already normalized. Generally, to complete the calculation of the dimensionless local erosion rate $E(\theta, \dots)$, it remains to specify (besides the erosion yield parameters of Table 1) the three inertial impaction functions: $V_p(v, \theta)/U$, $\theta(v, \theta)/(\pi/2)$ and $\eta_{\text{local}}(v, \theta)$ for the flow geometry at hand.

In any case, of particular interest to us will be the maximum local value E_{lim} of E , occurring at angular position $\theta = 0$ (or θ_m for the cyclone target sector, Fig. 1(b), Section 2.5), as well as the mean value, \bar{E} , of E over the upwind-facing surface of the circular cylinder, i.e.:

$$\bar{E} = \left(\frac{2}{\pi} \right) \int_0^{\pi/2} E(\theta, \dots) \cdot d\theta \quad (9)$$

These functions are included here (Figs. 6-8) only for the limit $(\bar{v}/v_{\text{crit}})^{1/3} \gg 1$, i.e. infinite Stokes number.

We note that $(ER)_c$ (Eq. (1)) scales as $U^{m+1} \cdot \phi_{p,m}$. Since our dimensionless E -functions are explicitly independent of $\phi_{p,m}$, this indicates that all absolute erosion rates are simply linearly proportional to the volume fraction of abrasive particles in the mainstream. The procedures explicitly illustrated here for a convex circular cylinder target (Fig. 1(a)) could, of course, be implemented for any other convex aerodynamic shape of particular interest. Albeit more approximately (due to multiple erodent particle impacts on the same target; Assumption (1) and Section 4.3), they will also be useful for many concave ceramic target shapes, as illustrated below for a cyclone target area (Fig. 1(b) and Section 2.5).

2.4. Inertial impaction for a cylindrical target in cross-flow: Limiting case of very large Stokes numbers ($Stk_p \gg 1$)

For the general case [28,29], we need to invoke inertial impaction correlations of individual particle trajectory calculations to estimate impinging particle frequencies, impact velocities and angles [33,32,34]. But, in the limit where most particles in the mainstream population are so large that they follow nearly straight line paths (for Stokes number based on a particle of volume v , satisfying the inequality: $Stk_p \gg 1$, the special case to which we restrict ourselves here) all particles will impact the circular cylinder at the velocity $V_p = U$ with local incidence angle $\theta = \theta$. In this limit, the general relations for local impingement efficiency, η_{local} , and maximum angle, θ_{max} , experiencing impaction on a circular cylinder reduce to:

$$\eta_{\text{local}}(v, \theta) \rightarrow \cos(\theta) \quad (10)$$

$$\theta_{\text{max}} \rightarrow \pi/2 \quad (11)$$

Inspection of the general quadrature expression $E(\theta, \dots)$ (Eq. (6)) reveals that when $(\bar{v}/v_{\text{crit}})^{1/3} \gg 1$ then:

$$\lim E(\theta, m, l) = E_{\text{lim}}(\theta, m, l) = \mu_{l+1} \cdot \cos^{m+1}(\theta) \quad (12)$$

Here

$$\mu_{l+1} = \int_0^{\pi/2} \int_0^{\pi/2} C_m(v) dv \cdot \left(v^l \right)^{m+1} \quad (13)$$

is the $(l+1)$ th moment of the normalized mainstream size distribution function $C_m(v)$ (see Section 2.7). Note that, in general, μ_{l+1} differs from unity since $l \neq 0$ (Table 1) and not

obtained by using the known exact results of this integral for $m=0, 1, 3$ as anchor points in a quadratic interpolation formula (cf. Fig. 6).

2.5. Concave target sector of cyclone particle separator

Despite possible complications of re-impingement or "blanketing" (local shielding) (Section 4.3 and Assumption (1)), it is interesting that our present formulation, with only minor modifications, can be used to estimate local and total ceramic erosion rates for the concave target area of a cyclone particle separator (Fig. 1(b)). Apart from the fact that direct impingement now only occurs between the angles θ_m and $\pi/2$ (where $\theta_m = \sin^{-1} [1 - (R_c/R_c)]$) in the (worst case) limit of rectilinear particle paths our previous results for $E(\theta, m)$ still apply, but now the average erosion rate will be $(ER)_c \cdot \mu_{l+1} \cdot \bar{E}_{\text{lim}}(m, \theta_m)$, where:

$$\bar{E}_{\text{lim}}(\theta_m, m) = \left(\frac{\pi/2}{\pi/2 - \theta_m} \right)^{-1} \cdot \int_{\theta_m}^{\pi/2} \cos^{m+1}(\theta) \cdot d\theta \quad (16)$$

and it will be noted that $\bar{E}_{\text{lim}}(0; m) = \bar{E}_{\text{lim}}(m)$ (Eq. (15)). Values of $\bar{E}_{\text{lim}}(\theta_m, m)$ via numerical integration are shown in Fig. 8 for two relevant values of the cyclone geometry parameter θ_m . Again, using exact values for the particular cases $m=0, 1$, and 3 as anchor points in a quadratic interpolation formula, we derive the approximate formula:

$$\bar{E}_{\text{lim}}(\theta_m, m) = C_0 + C_1 m + C_2 \cdot m^2 \quad (17)$$

where:

$$\begin{aligned} C_0 &= (1 - \sin(\theta_m)) / ((\pi/2) - \theta_m) \\ C_1 &= (11/16) - (3/4) \sin(\theta_m) \cos(\theta_m) / ((\pi/2) - \theta_m) \\ &\quad - (3/4) (1 - \sin(\theta_m)) / ((\pi/2) - \theta_m) \\ &\quad + \sin(2\theta_m) / (24((\pi/2) - \theta_m)) \\ &\quad + \sin(4\theta_m) / (192((\pi/2) - \theta_m)) \\ C_2 &= (1/3) (1 - \sin(\theta_m)) / ((\pi/2) - \theta_m) + (1/4) \\ &\quad \cdot \sin(\theta_m) \cos(\theta_m) / ((\pi/2) - \theta_m) \\ &\quad - \sin(2\theta_m) / (24((\pi/2) - \theta_m)) \\ &\quad - \sin(4\theta_m) / (192((\pi/2) - \theta_m)) \end{aligned} \quad (18)$$

Eq. (17) is plotted in Figs. 7 and 8 for θ_m equal to 0.2527 and 0.5236 rad, respectively) and compared with the corresponding numerical integrations of Eq. (16). However, since, often, $\theta_m \ll 1$, we can also use the convenient alternative:

$$\bar{E}_{\text{lim}}(\theta_m, m) = \bar{E}_{\text{lim}}(m) - (2/m) \cdot [1 - \bar{E}_{\text{lim}}(m)] \cdot \theta_m - 2(2/m)^2 \cdot [1 - \bar{E}_{\text{lim}}(m)] \cdot \theta_m^2 \quad (19)$$

where $\bar{E}_{\text{lim}}(m)$ is the corresponding complete upwind cylinder surface erosion rate function.

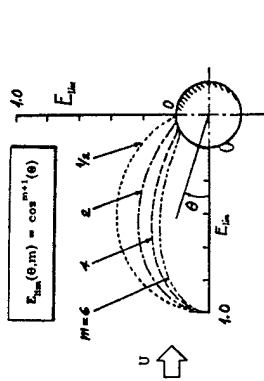


Fig. 5. Polar plot of normalized local erosion rates, $E_{\text{lim}}(\theta_m)$, on upwind surface of ceramic (coated) circular cylinder in crossflow.

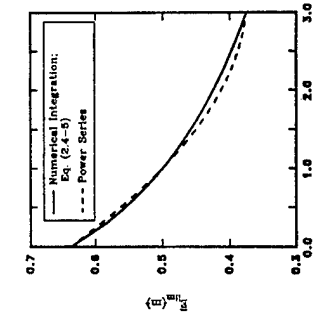


Fig. 6. Dependence of the function $E_{\text{lim}}(m)$ on the erosion parameter m , upwind surface of a circular cylinder in crossflow.

all particles in the mainstream erodent distribution have size v_m . This result, Eq. (12), which is independent of the erosion yield parameters E_p and η , reveals that in the present case the stagnation point value of $E_{\text{lim}}(0, \dots)$ for a monodispersed stream would be unity (for any m), and can be identified with $E_{\text{lim,max}}$. These simple limiting relations were used to generate the (polar-plot) results shown in Fig. 5. If we now use Eq. (12) to calculate the target upwind surface-averaged erosion rate function \bar{E}_{lim} (cf. Eq. (9)) we find:

$$\bar{E}_{\text{lim}}(l, m) = \mu_{l+1} \cdot \left\{ \frac{2}{\pi} \int_0^{\pi/2} \cos^{m+1}(\theta) d\theta \right\} \quad (14)$$

where the factor $\left\{ \frac{2}{\pi} \int_0^{\pi/2} \cos^{m+1}(\theta) d\theta \right\}$ will be recognized as $\bar{E}_{\text{lim}}(m)$ for the special case when all particles in the mainstream have the same size v_m . This function can be obtained by carrying out the indicated numerical integration, with results (for $0 < m < 3.0$) given in Fig. 6. As a useful approximate formula for making future calculations we suggest the power series:

$$\bar{E}_{\text{lim}} \approx (2/\pi) + [(11/16) - (8/(3\pi))] \cdot m + [(2/(3\pi)) - (3/16)] \cdot m^2 \quad (15)$$

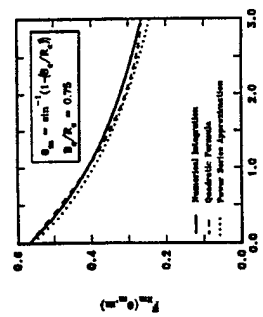


Fig. 7. Dependence of the cyclone target erosion function on the erosion parameter m for a cyclone geometry with $B_c/R_c = 0.75$; impingement sector of cyclone inner walls (Figs. 7 and 1(b)).

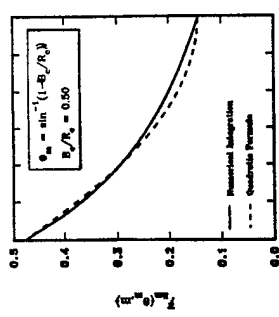


Fig. 8. Dependence of the cyclone target erosion function on the erosion parameter m for a cyclone geometry with $B_c/R_c = 0.50$; impingement sector of cyclone inner walls (Fig. 1(b)).

Fig. 7 also shows a comparison between the series approximation given by Eq. (19) and the numerical integration using Eq. (16) for the case $\theta_m = 0.2527$ rad. Since Eq. (19) becomes less accurate when θ_m does not satisfy the inequality $\theta_m \ll 1$, Eq. (17) would be more appropriate to use.

This concludes our derivation of the formulae needed to predict all ceramic cylinder target erosion rates of interest in this paper. Use of these dimensionless functions to estimate local and total cyclone target section absolute erosion rates (e.g. mm per year recession) is illustrated in Section 4.1.

2.6. Correction factor for departures from pure crossflow

It is possible to include commonly encountered cases in which the configuration departs from "pure crossflow", i.e. the erodent-containing stream direction and target cylinder axis are not perpendicular. Then, in the worst-case limit of rectilinear particle trajectories:

$$\cos(\theta) = \cos(\Lambda)\cos(\theta) \quad (20)$$

where Λ is the complement of the angle between the flow direction and the cylinder axis. Therefore, all previous calculations apply if we merely introduce the additional spanwise-flow correction factor: $\cos^{m+1}(\Lambda)$.

2.7. Correction factor for mainstream erodent particles distributed in size according to the Rosin-Rammler function

For suspended particles in the size range capable of impacting and erosion damage, a common form of size distribution function $C_m(v)$ has the property:

$$\int_0^{\infty} v \cdot C_m(v) dv \cdot \int_0^{\infty} (v/v_{ref})^n = \exp[-(v/v_{ref})^n] \quad (21)$$

where the (Rosin-Rammler) exponent n is an important "monodispersity" (inverse-spread) parameter for the population and v_{ref} is any convenient reference particle volume (including v_m). For this important case we find, for the $(l+1)$ th moment of the normalized size distribution function $C_m(v)$, the useful result [29]:

$$\mu_{l+1} = (v_{ref}/v_m)^l \cdot \Gamma(1 + (l/n)) \quad (22)$$

where $\Gamma(1 + (l/n))$ is the gamma function of the indicated argument $1 + (l/n)$, which can also be written $(l/n)!$, in terms of the factorial function. However, when the spread parameter n is less than unity, as has been reported for the impacting portion of many abrasive powder populations, this result must be increased because of the required introduction of a small-size (volume) "cut-off". As an example, for pulverized coal a typical n -value is 0.4 (i.e. 1.2/3). Thus, if $l=1.2$ (Table 1) $(l/n)! = 3-6$. With the above-mentioned "cut-off correction" this leads to $\mu_{l+1} = 9.6$, corresponding to almost a one-decade erosion rate increase due to mainstream polydispersity (for the particular case: $l=1.2$, $n=0.4$).

3. Procedure to determine best-fit values of the erosion parameters l, m, n , and v_{ref} from available erosion yield data

3.1. Use of erosion test rig data for planar targets with known impingement conditions

To utilize this simplified formulation (see Section 2) and conveniently summarize experimental erosion yield data provided in the literature, a practical procedure is required to determine best-fit values of the erosion yield parameters: l, m, n , and v_{ref} associated with any given set of ceramic erosion yield data (e.g. iso-velocity ϵ_p vs. angle-of-incidence data). In this work, the dimensionless absolute erosion yield, ϵ_p , is defined as the average volume of ceramic target removed per unit volume of impacting erodent particle. The

normalized erosion yield, (θ, θ) , is calculated by dividing the erosion yield, ϵ_p , by the erosion yield at normal incidence (i.e. at $\theta=0^\circ$), all necessary quantities being held constant. When erosion yield data at normal incidence were not available (as in Keairns et al. [11]), data extrapolation was utilized to estimate ϵ_p at $\theta=0^\circ$.

Table 1 summarizes the results of our analysis of available erosion yield data for a variety of ceramic target material/erodent systems near 300 K; best-fit values of the four erosion parameters: l, m, n , and v_{ref} are provided. Note that our reported values of v_{ref} (cf. Eq. (2)) pertain to particle reference velocity, $V_{ref} = 100 \text{ m s}^{-1}$, a reference particle size, $d_{p,ref} = 100 \mu\text{m}$, and normal incidence.

Fig. 2 shows the dependence of erosion yield ϵ_p on particle velocity v_p and angle of incidence θ (relative to target normal) for the system: unannealed glass target/cast iron erodent ($d_p = 580 \mu\text{m}$) at 300 K. It is clear from this figure that our results (using Eq. (2) and Table 1) are in excellent agreement with the corresponding experimental results generated by Finnie [31]. Similarly, Fig. 3 shows the experimental erosion yield data for "dead-burned" dolomite particles impacting on a 96% high-purity alumina castable target at various angles of incidence and mainstream velocities [1]. Also shown are the erosion yields calculated using the chosen erosion yield law (Eq. (2)) and the four parameters reported in Table 1. Note that the erosion yield increases noticeably as the particle velocity increases from 10.1 m s^{-1} to 14.3 m s^{-1} . Furthermore, the experimental data and our simple four-parameter model representation are in acceptable agreement. For example, the absolute deviation between the experimental and predicted erosion yield for incidence angles bounded between $\theta=0^\circ$ and $\theta=45^\circ$ is $\leq 10\%$ (at $\theta=75^\circ$ where much less erosion is expected, the absolute deviation is about 40%). Additional satisfactory results were obtained for the other types of castable target/erodent systems tested by Keairns et al. [11].

Our analysis of these cases and similar erosion data (presented in Table 1) demonstrates the engineering utility of our proposed erosion data representation technique. Combined with local impaction frequency calculations (Section 2.3), these erosion yield parameters will be seen to simplify dramatically the engineering prediction of local and total erosion rates.

3.2. Enlargement of Table 1 based on available relative erosion rate data

The present reformulation of the canonical erosion problem, together with our tabulations of parameters based on available experimental data (Section 3.1), lends itself to augmentation based on the existence of relative erosion rate data also in the literature. As an interesting example, Hansen [35] reported the relative erosion rates of some 80 target materials exposed at normal incidence, and at two temperature levels: 298 K and 973 K, to $27 \mu\text{m}$ diameter alumina particles at a velocity of 170 m s^{-1} . Hansen chose Stellite 6B

(a cobalt-chromium alloy) as his reference target and reported ca. 80 relative erosion factors (REF-values) on this basis. Since Hansen reported no absolute erosion rates, nor enough impingement condition information to calculate corresponding erosion yields, and since Stellite 6B is not present in our Table 1 (or in Table 1 of Kho et al. [19]), it would appear that Hansen's database (which includes some 18 ceramic targets) cannot be used to augment our present Table 1, or to make engineering calculations for these ceramic targets exposed to alumina dusts. However, upon reflection, we can proceed as follows: at 298 K, Hansen reported that #304 stainless steel eroded at the same rate as Stellite 6B, and, from the data reported by Tabakoff et al. [36] for the Al_2O_3 /#304 SS system at 298 K, we have estimated: $v_{ref} = 3.6 \times 10^{-4}$, ϵ_p (normal incidence)/ ϵ_p (most vulnerable incidence angle) = 0.48, and $n=2.0$, $l=0$. These particular absolute values "open the door" to placing Hansen's REF-data on an absolute basis, not only for many ceramic targets (of interest here), but also for some 22 metal alloys, 13 cemented carbides, and 15 coatings.

Correcting for the dependence of v_{ref} on erodent velocity, incidence angle, and (for ceramics) erodent particle size, we are thus led to the following v_{ref} estimate for any 298 K ceramic REF-value tabulated by Hansen [35]:

$$v_{ref} = (3.6 \times 10^{-4} / 0.48) \cdot (170/100)^{-(n-2.0)} \cdot (100/27)^n \cdot (\text{REF}) \quad (23)$$

As two specific examples, consider Hansen's REF-values of 0.40 and 0.12, for targets of hot-pressed (Norton) Si_3N_4 and SiC, respectively. Assuming that for these ceramic targets, $n=2.3$ and $l=1.2$, we then estimate that these 298 K REF-values correspond to v_{ref} (Al_2O_3 erodent/ Si_3N_4 target) = 3×10^{-2} and v_{ref} (Al_2O_3 erodent/SiC target) = 0.9×10^{-2} . This strategy could therefore be used to generate an enlarged database to allow absolute erosion predictions for many erodent/ceramic target systems of engineering interest. Such an enlarged compendium of dimensionless erosion yield parameters (cf. Table 1) will also facilitate the development of rational correlations with combinations of more fundamental mechanical properties of these erodent/target systems, further broadening the domain of applicability and predictive/design value of this approach (see Section 5).

4. Implications, applications, and generalizations

4.1. Direct use to predict erosion rate behavior

The following two numerical examples illustrate the utility of our reformulation of the problem of predicting erosion

¹ In light of the more direct v_{ref} estimates included in our Table 1, these tentative estimates for hot-pressed Si_3N_4 and SiC must be viewed with caution because of a possible (uncorrected) erodent particle size effect (for the $27 \mu\text{m}$ diam. Al_2O_3 erodent/#304 SS planar target in Hansen's (incompletely documented/characterized) test rig.

rates for the canonical geometry of a circular cylinder (sector).

4.1.1. Example 1: Leading edge of a gas-turbine stator blade

We calculate here the erosion rate (units: mm per year) of an initially 0.25 mm thick protective ceramic coating on the leading edge of a gas-turbine stator blade in a pressurized fluidized bed combustor (PFBC) combined cycle unit. Suppose that the gas turbine blades are subjected to a hot gas stream containing suspended ash at operating temperature and pressure of about 1000 K and 11 atm, respectively. Assume, further, that the ash particles have a mean particle diameter d_p of, say, 40 μm , the mainstream gas velocity is about 300 m s^{-1} , and the particle loading is 35 ppm (mass of erodent/mass of gas). Let the four erosion yield parameters describing the blade's protective ceramic coating be: $l = 1.2$, $m = 0.6$, $n = 2.8$, and $s_{p,er} = 7.5 \times 10^{-7}$. If the intrinsic density of each erodent particle is $3.17 \times 10^3 \text{ kg m}^{-3}$, and that of the hot gas stream is 3.44 kg m^{-3} (at 1000 K and 11 atm), then the mainstream volume fraction, $\phi_{p,m}$, of erodent particles will be $(3.44)(35 \times 10^{-6}) / (3.17 \times 10^3) = 3.8 \times 10^{-4}$ (i.e. about 0.04 ppm). Also, the value of the erosion parameter corrected to actual gas turbine operating conditions, $s_p(U,0,d_p)$, will be $(7.5 \times 10^{-7})(300/100)^{2.8} (40/100)^{3.12} = 6.0 \times 10^{-7}$.

The characteristic erosion rate, $(ER)_c$, can then be calculated from the product $s_p(U,0,d_p)$ (mainstream volume fraction) (mainstream velocity) = $(6.0 \times 10^{-7})(3.8 \times 10^{-4})(300)(10^3)$ = 0.22 mm y^{-1} . The local erosion rate can be calculated by multiplying $(ER)_c$ by $E_{lm}(\theta, m)$, i.e. by $\cos^{m-1}(\theta)$, and the maximum local erosion rate (here at $\theta = 0$) would be 0.22 mm y^{-1} . Finally, the mean erosion rate can be calculated by multiplying $(ER)_c$ by the value of $\bar{E}_{lm}(m)$ estimated at $m = 0.6$ using Fig. 6 or Eq. (15). Therefore, the mean erosion rate of the turbine blade's leading edge would be $(0.22)(0.55) = 0.12 \text{ mm y}^{-1}$. Based on these estimated erosion rates, one can, for example, decide on the necessary replacement frequency of the ceramic protective coating system (e.g. in this example about every 2 years of continuous operation).

4.1.2. Example 2: Refractory-lined cyclone

Consider a refractory-lined cyclone separator such as that used with a CFBC unit operating at a pressure near 1 atm. Assume that the cyclone concave target liner is aluminous cement and petite insulating refractory concrete (density 0.80 g cm^{-3}). Consider a CFBC cyclone operated at an inlet gas velocity of approximately 30 m s^{-1} and a gas temperature of 1270 K. Therefore, for this numerical example, we assume that the cyclone liner is exposed to a 30 m s^{-1} solid/gas stream of density 1.18 kg m^{-3} containing sand particles (SiO_2) with an average diameter of $150 \mu\text{m}$ and intrinsic density 2.4 g cm^{-3} . (Sand is chosen to represent the main erodent since it is the hardest material found among the minerals in a CFBC cyclone.) Furthermore, assume that the solids-containing gas stream has a particle (SiO_2) mass loading

of 200 ppm. Our objective (in this example) is to predict the maximum local ceramic liner erosion rate (mm y^{-1}), as well as the mean erosion rate over the target area bounded between $\theta = 30^\circ$ and $\theta = 90^\circ$ (Fig. 1(b) and Fig. 8).

The first step is to calculate the characteristic erosion rate $(ER)_c$. For this purpose, the value of the erosion yield $s_p(U,0,d_p)$ at $V_p = U = 30 \text{ m s}^{-1}$ and $d_p = 150 \mu\text{m}$ can be calculated as follows. The erosion parameters l, m, n , and $s_{p,er}$ for the insulating refractory concrete/sand particle system can be estimated using the 300 K erosion yield data summarized in Table 1. Pertinent values of the erosion parameters are seen to be $l = 1.2$, $m = 0.5$, $n = 2.3$, and $s_{p,er} = 1.45 \times 10^{-3}$ (evaluated at $d_{p,er} = 100 \mu\text{m}$ and $V_{p,er} = 100 \text{ m s}^{-1}$). Then, $s_p(U,0,d_p)$ for this application = $(1.45 \times 10^{-3})(150/100)^{3.12} (30/100)^{2.3} = 3.91 \times 10^{-4}$.

The mainstream volume fraction of the sand particles will be $(1.18)(2 \times 10^{-4}) / (2400) = 0.98 \times 10^{-7}$ (i.e. $\approx 0.1 \text{ ppm}$) and $(ER)_c = s_p(U,0,d_p)$ (mainstream volume fraction) (mainstream velocity) = $(3.91 \times 10^{-4})(0.98 \times 10^{-7})(30)(10^3)$ = $(8760)(36000)$ = 36 mm y^{-1} . The maximum local erosion rate can be calculated using the dimensionless local erosion rate function $E_{lm}(\theta)$ evaluated at $\theta = \theta_m$ and, therefore, $E_{lm}(\theta_m) = \cos^{m-1}(\theta_m) = \cos^{0.5}(30^\circ) = 0.806$. Thus, the maximum local erosion rate is $(36)(0.806) \approx 29 \text{ mm y}^{-1}$. Furthermore, the mean erosion rate can then be calculated from $(ER)_c$ and the function $\bar{E}_{lm}(\theta, m)$ evaluated at $\theta_m = 30^\circ$ and $m = 0.50$ using Fig. 8 or Eq. (17). The value of $\bar{E}_{lm}(\theta, m)$ can be found from Fig. 8 to be equal to 0.368 and, therefore, the mean erosion rate under these conditions would be $(36)(0.368) = 13 \text{ mm y}^{-1}$ (evaluated over the target area bounded between $\theta = 30^\circ$ and $\theta = 90^\circ$).

Note that in these numerical examples we evaluated target erosion rates at room temperature (for which the necessary data were available) rather than at actual operating temperatures. Often, this assumption is conservative since for many refractories, material loss decreases as temperature increases (Liebhaf 24]; see also Section 4.4). This was true for nearly 2/3 of the ceramic target/erodent systems examined at 298 K and 973 K by Hansen [35]. However, a notable exception was hot-pressed (Norton) SiC exposed to alumina dust (which at 973 K eroded 3.7 times as fast as at 298 K).

4.2. Indirect use to infer parameters in the erosion yield law

Inspection of our universal results (Section 2, Figs. 4 and 5) reveals that $(ER)_c$ and/or the calculated quantities E, E_{max} , and/or \bar{E} are sometimes sensitive to the parameters l, m, n and/or $s_{p,er}$ appearing in the erosion yield law. In these regimes an observation of these quantities for a cylinder in a known test environment could clearly be used to extract rational estimates of those parameters least well known—perhaps m for a ceramic never previously studied in a well-characterized erosion test rig. This might be a reasonable

provisional method for making extrapolations to related environmental conditions, including ultimately predicting erosion damage on yet more complex ceramic shapes (e.g. a ceramic coated turbine stator blade) via particle trajectory analysis.

4.3. Examination of approximations

Confidence in the validity of most, if not all, of our underlying assumptions can be generated based on the observations collected in Rosner et al. [28,29]. In some cases we are led to interesting questions which appear to remain open, and warrant further examination. For the present, we briefly highlight the following underlying assumptions:

4.3.1. Locally planar target erosion behavior

The essential validity of Assumption (1) was experimentally demonstrated by carefully measuring the shape change of initially circular cylinder metal targets [37]. Because of the indicated radius of curvature disparity, this assumption can only be invalidated by large effects of stress, or anisotropy (see Assumption (6) and Section 4.4), both of which are not considered here.

4.3.2. Engineering applicability of available erosion yield data

Most erosion rate predictions for, say, combustion turbine or boiler applications have been based on the premise that erosion yield data can be invoked in situations where particles actually arrive simultaneously over a wide band of velocities and angles of incidence. Indeed, this premise underlies the development/use of such erosion test rigs. However, if the erosion mass loss process is not simply a single impact phenomenon this (usually implicit) additivity or uncoupling assumption should probably be examined more critically, perhaps based on the erosion rate experiments involving, e.g. pairs of incidence angles. We are presently unaware of such experimental tests of additivity in erosion situations.

Another important coupling phenomenon, which apparently has not been systematically studied, is the possible protective effect of the simultaneous acquisition of much smaller particles (or even condensed vapor) on the component whose erosion is of concern (see, for example, Rosner et al. [27-30]).

4.3.3. Neglect of particle-particle interactions and rebound phenomena

In most of the applications of concern here, the volume fraction of suspended particles, $\phi_{p,m}$, is small enough (often of order 10^{-6}) to render particle-particle interaction effects in the vicinity of a convex target negligible. Indeed, if one views the particle flow field as if there were no carrier gas (e.g. consider the limit $Stk \rightarrow \infty$, with elastic rebound from the target surface) this particle gas flow would correspond to a Knudsen number (ratio of mean-free-path to target transverse dimension L) of the order of $(2/3)(\phi_p)^{-1/2}(d_p/L)$, which, if $L = 1 \text{ cm}$, is about 1.4×10^5 for our present numer-

ical example (Section 4.1). For convex targets, this value is certainly large enough to justify the assumption of free-particle flow, even if every erodent particle rebounds. We are also neglecting erosion caused by particles that re-impinge on the same target after at least one previous impact event. The situation is less clear for concave targets, including our example of the target zone of a cyclone separator (Fig. 1(b)). In such cases, particle-particle interaction effects near the target would be expected to set in at much lower $\phi_{p,m}$ values.

4.3.4. Roughness and target shape evolution

We have explicitly considered cases in which the asymptotic roughness associated with (quasi) steady state erosion is small on the scale of the overall body dimension (for a circular cylinder, say, $d/2$), as must be the cumulative surface recession (cf. the numerical example in Section 4.1). Indeed, this is fully compatible with the erosion yield data being used, which is itself averaged over long times (many impacts during the constant erosion rate period). However, it is also possible to extract from the polar plots of $E(\theta, m)$ (Fig. 5) what might be called the "shape evolution tendency" of the target. In contrast to the case of metal target erosion, which revealed an interesting tendency to make an initially circular cylindrical leading edge (nose-region) wedge-shaped (sharpen) as time proceeds, Fig. 4 reveals that ceramic (coated) cylinders will tend to become blunter with time. Examples of shape evolution (in which Assumption (5) is relaxed) are contained in Rosner et al. [39].

4.4. Generalizations

It is useful to comment upon some valuable generalizations of our results in order to find ways to deal with more complex situations than those described in Section 2.1.

4.4.1. Arbitrary Stokes numbers

If the mean particle size, $d_{p,m}$, of the mainstream erodent particle population is not much greater than the critical size, $d_{p,crit}$, for the onset of inertial impaction in the prevailing aerodynamic environment then the rectilinear trajectory simplification breaks down. However, these cases are still tractable by making use of the correlated results of particle trajectory calculations for the geometry in question [28,29,32,38,40].

4.4.2. Abrasive particle blends

It is tempting to conjecture that if, as is common, the suspended particle population is actually a blend of several populations of rather different erosion propensity, the total erosion rate can be simply estimated as the sum of contributions from each sub-population. We are unaware if this plausible approach to estimate the erosion of ceramic targets in mixed erodent streams has yet been put to an adequate experimental test.

4.4.3. Quasi-steady application of steady-state results

In applications where the dust loading and gas stream conditions are not constant but, yet, change sufficiently slowly on the time scale (d/2)/U one can justifiably treat the total surface recession as the result of target exposure to a sequence of steady environments and summing their effects. In such cases (ER)z will be slowly varying, but the functions Emax(theta,m), Emin(theta,m), and Flim(theta,m) provided here will be time-independent, and, hence, retain their applicability.

4.4.4. Application to other important shapes/flow conditions

The present approach can clearly be applied to other simple target shapes, including spheres, cones, nozzle entrances, pipe elbows, etc. As shown above (Section 2.6), it is also possible to correct for departures from the pure crossflow configuration, irrespective of Sk.

4.4.5. Quasi-steady shape evolution

The present analysis was deliberately confined to the limiting case of modest target shape change (cf. Assumption (4)). However, by repetitive recalculation of the eroding target shape (and associated local angles of incidence), it is possible to track more extensive interface movements. Examples of such shape evolution for eroding ceramic targets in the high Stokes number limit are contained in Khalil and Rosner [39].

4.4.6. Implicit effects (temperature, reducing environments, stress, etc.)

The framework provided by the present analysis may allow several environmental effects (e.g. effects of temperature level to be implicitly included in the appropriate values of the four erosion yield parameters l, m, n, and epsilon_p,ref = epsilon_p(V_p,ref, theta = 0, d_p,ref = 100 micrometers) where, say, V_p,ref = 100 m/s and epsilon_p,ref = 100 micrometers for particular combinations of projectile/ceramic target materials (irrespective of whether an adequate theory is yet available to anticipate or extrapolate such effects). Another potentially important variable (evidently not adequately considered in previous erosion rate measurements) is the state of stress in the target material surface. For example, one would expect pre-existing tensile stresses to influence measured erosion yields, and hence the above-mentioned four parameters. However, we anticipate erosion/corrosion situations which will require more fundamental generalizations of the present approach, e.g. when the cos^m(theta) law becomes qualitatively incorrect at sufficiently high target temperatures.

4.4.7. Velocity exponent insensitivity to angle-of-incidence and erodent particle size

The separability of V_p, theta, and d_p,ref effects in the erosion yield law epsilon_p(V_p, theta, d_p,ref) (Eq. (2)) significantly reduces the

For the upwind portion of a stationary ceramic (coated) sphere, it is easy to show that (when mu_1 = 1) E_max(theta,m) = cos^{m+1}(theta) and hence E_min = (m+2)^{-1}.

number of dimensionless parameters appearing in our final results, and hence increases the generality and attractiveness of our "short-cut" procedure. However, there appear to be systems (combinations of projectile/ceramic target materials) for which, say, the velocity exponent n changes noticeably with angle-of-incidence. For such systems the shape function cos^m(theta) would not quite be the same at all impact velocities, another complexity that could be straightforwardly introduced into our general quadrature procedure.

4.4.8. Cylindrical targets machined from anisotropic monoliths

In such cases, the four above-mentioned erosion yield parameters l, m, n, and epsilon_p,ref will generally exhibit a non-negligible dependence on the angle between the principal axes intrinsic to the material anisotropy and the local target surface outward normal.

4.4.9. Threshold velocity for erosion damage

It is usually not possible to formally extrapolate the power-law velocity dependence of epsilon_p very far below the range of actual erosion rate measurements because of the likely existence of a threshold velocity below which no perceptible erosion (substrate loss) occurs. In effect, our previous procedures (Section 2.2 are based on the sequence of necessary inequalities: sound speed in target > V_p <= O(U) >> V_p (critical for capture)) and will inevitably over-estimate erosion rates when these rates are very small. Again, this systematic effect could be incorporated via a more general epsilon_p(V_p, theta, d_p,ref) law used in our quadratures Eq. (7) for the case of arbitrary Sk.

5. Conclusions and recommendations

By capturing with simple formulae the essential features of available erosion yield experiments on ceramic targets of usually planar geometry, we have developed and illustrated here an efficient approximate method to predict local and total surface erosion rates for ceramic targets of cylindrical (sector) shape exposed to abrasive particles suspended in a high-speed mainstream. For a circular cylinder target, in the high Stokes number, pure crossflow limit (Lambda = 0), universal graphs are provided here covering the anticipated parameter ranges of greatest interest. Based on a summary of available experimental data, we also provide representative sets (for 38 commonly encountered combinations of ceramic targets and erodents, including SiC, SiO2, Al2O3, cast iron, and dolomite (CaCO3/MgCO3), of numerical values of the four key phenomenological parameters that emerge from our formulation (viz. l, m, n, and epsilon_p,ref; cf. Eq. (2)), albeit at T_s approx 300 K. If the mainstream erodent particles are distributed in size according to the Rosin-Rammler function we derive (Section 2.7 the appropriate correction factor (to be applied to the erosion rate calculated if all erodent particles had the mean particle volume, v_p,ref). Similarly, our present results

also apply to cases with departures from pure cross-flow (i.e. Lambda != 0, where Lambda is the complement of the angle between the flow direction and the cylinder axis) by simply introducing the additional spanwise flow correction factor: cos^{m+1}(Lambda) to the results for E_max, E_min, and F_lim given above. To deal with more general, or singular cases that may be of particular interest to the reader, the required correlation formulae and associated quadrature expressions are provided. This includes the (finite Stokes number) case of polydispersed erodent particles which are not all large enough to follow rectilinear trajectories in the local, target-modified flowfield.

In addition, the present mathematical model and these results (Figs. 2-8 for the large Stokes number limit) reveal that ceramic target erosion rates will be directly proportional to the abrasive particle mass loading (or particle volume fraction) in the mainstream, and quite sensitive to mainstream velocity; viz. proportional to U^{m+1} (where, often n approx 2.3; cf. Table 1).

Several potentially useful extensions of this phenomenological approach have been indicated in Section 4. This includes applications to other, possibly interacting, convex-shaped ceramic targets, such as turbine stator blade cascades exposed to a polydispersed erodent suspension. We are also investigating the erosion of yet other classes of commonly encountered shapes, including axisymmetric nozzles and circular arc elbows and bends. We believe our methods can be developed in such a way as to also predict maximum attainable drilling and cutting rates for various target/erodent combinations.

Finally, our present reformulation of the canonical erosion yield problem has much to recommend it as a convenient new standard for the assembly of experimental erosion-yield parameters for each erodent/target system (see Table 1, giving dimensionless epsilon_p,ref, l, m, n values in an organized format). This itself will greatly facilitate the important next step, viz. showing, with the indispensable guidance of rational micro-mechanical theories, how each of these dimensionless parameters correlates with certain dimensionless groupings of fundamental mechanical properties of the participating materials. Only when this is accomplished will it be possible to design erosion-resistant engineering equipment, i.e. propose optimal materials of construction for each erosive environment.

Acknowledgements

This research was supported, in part, by AFOSR (Grant 94-1-0143) and DOE-PETC (Grant DE-FG-2290PC90099), as well as the Yale HTRC Laboratory Industrial Affiliates (ALCOA, Dupont, Shell and Union Carbide/Praxair Corporations). It is also a pleasure to acknowledge helpful discussions and/or correspondence with J. Fernandez de la Mora, M.J. Labowsky, P. Tandon, R.C. Tucker, Jr., and A.G. Konstandopoulos.

Appendix A. Nomenclature

B_c	width of cyclone inlet (Fig. 1(b))
$C_w(v)$	normalized mainstream particle size distribution function
d_p	particle diameter
d_t	target diameter (Fig. 1(a))
$(ER)_z$	characteristic erosion rate associated with mainstream abrasive particle volume flux if all particles struck the ceramic solid target at normal incidence with (mainstream) velocity U
$E(\theta, \dots)$	dimensionless local erosion rate function (Eq. (7))
E_{max}	maximum (peak) local erosion rate; occurring at angular position $\theta = 0^\circ$ (Fig. 1(a)) or θ_m (Fig. 1(b))
E_{lim}	average dimensionless erosion rate function; Eq. (9) where $Sk \rightarrow \infty$
$f(\theta)$	normalized erosion yield; $= \epsilon_p / (\epsilon_p)$ evaluated at $\theta = (\theta)$ (Fig. 4)
$F_{lim}(\theta_{opt}, m)$	cyclone target dimensionless erosion function; Eq. (16)
L	transverse reference length for target (d for circular cylinder, Fig. 1(a))
l	dimensionless exponent which describes the sensitivity of erosion yield to projectile particle size (volume, v_p)
m	dimensionless exponent appearing in $\cos^m(\theta)$ to angle of incidence θ (measured with respect to the local target normal)
n	dimensionless exponent representing sensitivity of erosion yield to projectile incident velocity V_p
N_p	number density of abrasive particles
R_c	cyclone separator inner wall radius (Fig. 1(b))
Sk	particle Stokes number; $\rho_p / (d/2)U^2 [31,32]$
t_p	particle stopping time
U	mainstream velocity
$v_{p,ref}$	particle volume $= (\pi/6) \cdot d_p^3$
\bar{v}_m	reference particle volume $= (\pi/6) \cdot d_p^3$, with $d_p = 100 \mu m$
V_p	mean particle size (volume) in mainstream
$V_{p,ref}$	particle impact velocity
$V_{p,ref}$	reference particle impact velocity ($= 100 \text{ m s}^{-1}$ here)
ϵ_p	dimensionless erosion yield per particle impact (defined as average volume of ceramic target removed per unit volume of impacting erodent particle)
$\epsilon_{p,ref}$	ϵ_p evaluated at $V_p = 100 \text{ m s}^{-1}$, $\theta = 0^\circ$, and t_p corresponding to $d_p = 100 \mu m$
ω_p	particle mass loading in mainstream ($= \text{kg erodent/kg gas}$ when $\omega_p \ll 1$)

- mainstream particle volume fraction; $(\partial N/\partial t)_0$ particle incidence angle; $\theta = 0^\circ$ refers to normal incidence, and $\theta = 90^\circ$ refers to grazing incidence (see Fig. 1(a))
- θ angular position on target measured from the stagnation line (Fig. 1)
- θ_m minimum angle (Fig. 1(b)) experiencing cyclone inlet particle erosion (in the large Stokes number limit)
- θ_{loc} local impingement efficiency (Section 2.3)
- Λ complement of the angle between the flow direction and the cylinder axis
- Γ gamma function of the indicated argument $(1 + (l/v))$ (see Eq. (22))
- ν Rosin-Rammler exponent shown in Eq. (21)
- μ_{+1} moment function defined by Eq. (13)
- CFBC circulating fluidized bed combustor limit
- PFBC pressurized fluidized bed combustor
- REF relative erosion factor (Section 3.2 and Hansen (35))
- $O(\)$ order of magnitude operator
- $(\)!$ factorial function
- $9.6E-4$ 9.6×10^{-4} , etc. (see Table 1)

References

- [1] D.L. Keatins, W.C. Yang and W.G. Vaux, Design of refractories for coal gasification and combustion systems, *EPRI AP-1151*, Electric Power Research Institute, Palo Alto, CA, July 1979.
- [2] D.R. Reid and E. Ruh, Abrasion resistance of refractories, *Ceramic Bulletin*, 40 (7) (1961) 452-455.
- [3] L. Frannie, Erosion of surfaces by solid particles, *Wear*, 3 (1960) 87-103.
- [4] C.E. Yeaslee, Erosion resistance of ceramic materials for steamboiler refinery applications, *Ceramic Bulletin*, 38 (7) (1959) 363-368.
- [5] S.T. Woodard, Erosion resistant coatings for steam turbines, *EPRI CS-3415* Electric Power Research Institute, Palo Alto, CA, 1987.
- [6] T. Elliott, Shoor for more durable, less costly refractory in CFB units, *Power (February 1994)* 69-71.
- [7] G.L. Barna and R.R. Riley, Abrasion test for refractories, *Ceramic Bulletin*, 46 (9) (1967) 824-828.
- [8] R.E. Dial, Refractories for coal gasification and liquefaction, *Ceramic Bulletin*, 54 (7) (1975) 640-643.
- [9] P.A. Eigel, *Inspect Wear of Materials*, Tribology Series 2, Elsevier, Amsterdam, 1978.
- [10] R.G. Hood, Consider advanced ceramics for valve thims, *Chemical Engineering Progress*, (May 1994) 64-67.
- [11] S.S. MacAdam and J. Strieger, Particle impact and impact distribution within a fluidized bed combustor environment, *Wear*, 141 (1991) 373-394.
- [12] J.H. Nelson and A. Gilchrist, Erosion by a stream of solid particles, *Wear*, 11 (1968) 111-122.
- [13] J.H. Nelson and A. Gilchrist, An experimental investigation into aspects of erosion in rocket motor tail nozzles, *Wear*, 11 (1968) 123-143.
- [14] D.E. Roemer, *Transport Processes in Chemically Reacting Flow Systems*, Butterworth-Heinemann, Stoneham, MA, 1986.

- [37] R.H. Bartalow, J.A. Goebel and F.S. Pettit, Erosion-combustion coatings and superalloys in high-velocity hot gases, in W.F. Adler (ed.), *Erosion: Prevention and Useful Applications*, ASTM Special Technical Publication 664, 1979.
- [38] D.E. Roemer, S.A. Oskogis and R. Israel, Rational engineering correlations of diffusional and inertial particle deposition behavior in non-isothermal forced convection environments, in R. Bryers (ed.), *Foiling and Heat Exchanger Surfaces*, Eng. Foundation, New York, 1983, pp. 235-256.
- [39] D.E. Roemer, Y.F. Khalil and P. Tandon, Prediction/correlation of erosion peaks and shape evolution for ceramic surfaces exposed to flows of abrasive suspensions, *Proc. 5th World Congress of Chemical Engineering*, AIChE, Vol IV, 1996, pp. 1013-1018.
- [40] A.G. Konstandopoulos, M.J. Labowaty and D.E. Roemer, Inertial deposition of particles from potential flows past cylinder arrays, *J. Aerosol Sci.*, 24 (2) (1993) 471-483.

Biographies

Dr. Yehia F. Khalil is a Lecturer in the Chemical Engineering Department, Yale University, New Haven, CT. Dr. Khalil is also a Research Affiliate of the High Temperature Chemical Reaction Engineering (HTCRE) Laboratory, Yale University. Dr. Khalil holds a PhD in chemical engineering from the University of Connecticut at Storrs. In addition, he has earned a NuClE and Master of Science degrees in nuclear engineering from the Massachusetts Institute of Technology (MIT) and

attended the MIT School of Chemical Engineering Practice where he earned an MSCEP degree in chemical engineering, and has been a fellow of the MIT Center of Advanced Engineering Studies. His published work has appeared in the Transactions of the American Chemical Society, Transactions of the American Nuclear Society, MIT Journal of Information Systems, and the Fuel Journal. Dr. Khalil taught graduate and undergraduate courses in environmental control technologies, nuclear engineering, queueing theory, decision analysis, system dynamics, and probabilistic risk assessment.

Dr. Daniel E. Roemer is Professor and formerly Chairman (1984-1987, 1993-1996) of the Department of Chemical Engineering at Yale University, where he also holds a joint appointment in Mechanical Engineering. He is founder and Director of the Yale High Temperature Chemical Reaction Laboratory and is an engineering consultant to many corporations and consortia. His research activities include convective energy and mass transport, interfacial chemical reactions, phase transformations, gas dynamics, fine particle technology, and combustion — subjects on which he has published over 200 papers and one book. He joined the Yale University engineering faculty after 11 years of research experience, having completed his undergraduate and PhD engineering degrees at City College of New York and Princeton University, respectively.

IN FORCE OF LAW
 NOTICE
 This document is approved and is
 distributed under the terms of
 STINFD PROCEEDINGS

Approved for public release,
 distribution unlimited